UNIVERSITY OF CALIFORNIA
SANTA CRUZ

INVESTIGATIONS ON THE STRUCTURES OF THE PENTAVALENT ANTIMONIAL DRUGS FOR THE TREATMENT OF LEISHMANIASIS

A dissertation submitted in partial satisfaction
of the requirements for the degree of

DOCTOR OF PHILOSOPHY
in
CHEMISTRY

By

Brent Lindquist-Kleissler

December 2023

The Dissertation of Brent Lindquist-Kleissler is approved:

_____
Professor Timothy Johnstone, chair

_____
Professor Pradip Mascharak

_____
Professor Theodore Holman

_____
Peter Biehl
Vice Provost and Dean of Graduate Studies

Table of Contents

List of Figures

Chapter 4

Chapter 5

Appendix B

Appendix C

Appendix D

List of Schemes

List of Tables

Appendix B

Appendix C

Investigations on the Structures of the Pentavalent Antimonial Drugs for the Treatment of Leishmaniasis

By

Brent Lindquist-Kleissler

A dissertation submitted in partial satisfaction of the requirements for the degree of

Doctor of Philosophy in Chemistry

Abstract

Antimony(Sb)-containing molecules have a rich therapeutic history. Their most significant clinical use in modern medicine is in the treatment of the neglected tropical disease leishmaniasis. Up to a million new cases of leishmaniasis are reported annually, and the disease disproportionately affects populations of low- and middle-income countries. The current frontline treatments for leishmaniasis are the pentavalent antimonials: meglumine antimoniate (Glucantime) and sodium stibogluconate (Pentostam). Although effective, the pentavalent antimonials have severe side-effects and resistance to the drugs is mounting. Despite the pentavalent antimonials having been used for nearly a century, their structures and mechanism of action are still unknown. Elucidation of these drugs' structures would allow for derivatization that could reduce toxicity while increasing the efficacy of treatment. Furthermore, structural knowledge of the pentavalent antimonials could prove pivotal in the elucidation of their mechanism of action. Presented here are our initial attempts to develop and apply techniques that will allow for better understanding of antimony

and its interactions with the ligands employed in the synthesis of the pentavalent antimonials. Quantum theory of atoms in molecules (QTAIM) was used to elucidate the character of bonding interactions between pnictogens and oxygen. Pentaphenylantimony served as a proof-of-concept compound for an exploration into the use of physical inorganic techniques such as X-ray absorption spectroscopy to provide insight to the geometry of Sb-containing compounds. The solution- and solid-state structures of a series of Sb-diolate compounds were investigated via ^{1}H and $^{13}C\{^{1}H\}$ nuclear magnetic resonance (NMR) spectroscopy and X-ray crystallography to gain a better understanding of how an Sb center is coordinated by secondary and primary alkoxides with varying stereochemistry. Trends in the chemical shifts from NMR spectra of these compounds were observed as a product of the stereochemistry of the diol chelating the Sb center. Elucidation of these spectroscopic signatures allows for future insight into Sb-containing molecules and their structures. The work described in this dissertation provides a foundational framework for understanding the interactions between polyalcohols and Sb, an important step toward improved Sb-containing therapeutics.

To Kathy and Arthur Lindquist-Kleissler

Acknowledgements

Firstly, I acknowledge my research supervisor, Professor Timothy Johnstone. When first we met at UCSC's recruitment weekend, I thought he was a prospective student like myself, due to his youth and exuberance. Little did I know that he would be one of the largest influences in my life and the best mentor I could ask for. Both in and out of the laboratory, Tim taught me more about life, science, and perspective than one could ever hope for from an academic advisor. Tim is truly unique in his ability to approach and solve problems. Along with all the scientific expertise, which Tim has so much of, he has taught me patience and appreciation. I will forever cherish his ability to teach, listen, and appreciate each person for their own strengths. Thank you for being one of the most genuine, honest, and curious people I have ever met.

I must also thank my fellow Johnstone Lab members (Johnstonians), without whom I would not have been able to enjoy my work to the extent that I did. All of whom accepted me for the wild card I can be. I am deeply grateful for their presence and insights, both in and out of the lab. Of great distinction is Dr. Daniel D. Droege, who was with me from the start and taught me how to handle difficult situations with grace.

I would like to acknowledge Leah M. Bouthillette, my dearest partner and friend. I cannot overstate the role that Leah has played in my personal growth. Leah has been understanding and accepting beyond what I ever expected from another person. Leah not only put up with my often-cantankerous nature, she acknowledged

and accepted me. To feel seen by another individual is something beautiful and profound, and Leah has done that for me. I thank her for everything she has given to me.

Finally, I acknowledge the invaluable support of my family, without whom I would have never achieved my goals. There has never been a better support group than my family. Of utmost importance, my family has taught me love. True love that crosses all lines, is a gift felt by few and appreciated by even fewer. As I have grown, I have realized the gift of friendship and family given by my sisters. Yet, above all else is the love I have experienced from my parents. Both my mother and my father have given all that they can to make me a worldly and compassionate man. Without my parents I would not have the opportunities I do, the passions I have, or the appreciation of life that I feel. I acknowledge and thank them above all else, without them I would not be who I am. To them I dedicate this Thesis.

Chapter 1

Overview of the Extant Structural Studies on the Pentavalent Antimony Drugs for the Treatment of Leishmaniasis

1.1 Introduction

This thesis will focus on antimony-containing molecules and their use as therapeutics against leishmaniasis. Leishmaniasis is a neglected tropical disease which is often treated with two antimony-containing drugs known as the pentavalent antimonials, meglumine antimoniate and sodium stibogluconate. Despite being used for nearly a century, the structures of the pentavalent antimonials are still unknown. Below is a discussion of the current state of knowledge on the pentavalent antimonials and leishmaniasis, followed by information on the electronics and bonding present in many antimony-containing molecules. Then the introduction of physical inorganic techniques that could prove useful in probing the structures of antimony-containing molecules, and finally information on the use of model compounds meant to model the interactions present in the pentavalent antimonials.

1.2 Antimony Therapeutics and Leishmaniasis

Antimony (Sb) has a rich therapeutic history spanning centuries. In fact, antimony's use in early medicine is well documented, despite – or perhaps because of – the high toxicity of many Sb-containing molecules.[1] One of the oldest known Sb-containing therapeutics is tartar emetic, also called potassium antimony tartrate, which is the potassium salt of the tartrate complex of Sb(III).[1] Tartar emetic, as implied by its name, was widely used to induce vomiting. Interestingly, it is still commonly used for this purpose in ornithological studies.[2]

Leishmaniasis is a neglected tropical disease, caused by infection with parasitic protozoans from the genus *Leishmania*. These parasites are spread by the bite of phlebotomine sand flies, commonly found in parts of the tropics, subtropics, and southern Europe. In people, the disease presents in three common forms. Cutaneous leishmaniasis is the most common form and presents with skin sores. Visceral leishmaniasis typically affects the liver, spleen, or bone marrow and is often fatal. Mucosal or mucocutaneous leishmaniasis causes sores primarily located in the mucous membranes of the nose, throat, or mouth. Leishmaniasis is most common in low- and middle-income countries with up to a million new cases reported annually.[3]

In 1913, potassium antimony tartrate was reported to be effective at treating mucocutaneous leishmaniasis.[4] This activity was later confirmed in visceral leishmaniasis in Italy, Africa, and India.[5-7] Potassium antimony tartrate (tartar emetic) was used medicinally for over 300 years, but it wasn't until the 1960s that its structure was confirmed. A series of studies revealed that the molecule features two four-coordinate Sb centers, each with a square-based pyramidal geometry.[8] However, due to severe side-effects treatment with potassium antimony tartrate was ceased before its structure was determined, leaving little need for improvement of the drug via purification or derivatization.

1.3 The Pentavalent Antimonials

The Sb-containing antileishmanial drugs meglumine antimoniate (Glucantime) and sodium stibogluconate (Pentostam) are collectively known as the pentavalent antimonials. These drugs are synthesized by combining a carrier ligand, either *N*-methyl-D-glucamine (meglumine antimoniate) or D-gluconic acid (sodium stibogluconate), with an Sb(V) source; typically $SbCl_5$ or $K[Sb(OH)_6]$ (Scheme 1.1).[9] These Sb(V) complexes were first introduced as therapeutics for leishmaniasis in the 1940s and are still the frontline treatment for all forms of leishmaniasis.[10] Despite their efficacy and widespread use, the pentavalent antimonials have many serious side effects that reduce patient quality of life and treatment with them can even be fatal. Attempts to rationally capitalize on their antileishmanial activity while reducing off-target toxicity are hampered by the fact that, as was the case with potassium antimony tartrate, there is little-to-no information on the structures of these molecules.[9] Knowledge of the pentavalent antimonials' structures could provide a framework for rationally developing more active and selective derivatives and understanding their mechanism of action. This knowledge would be invaluable in addressing one of the larger questions concerning the pentavalent antimonials: is each drug (i) an intractable mixture of multiple compounds or (ii) a set of one or more well defined compounds with other species present as minor components? If a mixture of molecules is present in these drugs, it may be the case that the components have differential toxicity and activity, making gaining knowledge of their structures vital to their improvement.

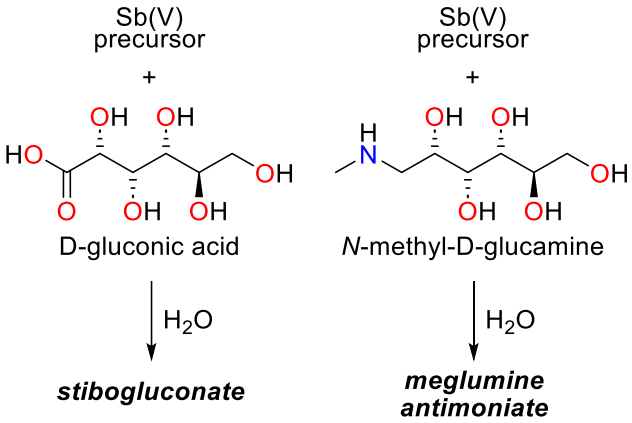

Scheme 1.1. Overall synthesis of the antileishmanial pentavalent antimonial drugs stibogluconate and meglumine antimoniate from an Sb(V) precursor such as hydrolyzed $SbCl_5$ or $K[Sb(OH)_6]$.

A large variety of different structures has been proposed for the pentavalent antimonials, many of which are informed by mass spectrometry studies.[9] Fast-atom bombardment mass spectrometric (FAB-MS) data on commercially available meglumine antimoniate suggested the drug consists of two molecules of *N*-methyl-D-glucamine (NMG) coordinated to a single Sb center in a symmetrical geometry.[11] However, another study implementing positive-ion mode electrospray ionization mass spectrometry (ESI(+)-MS) suggested the existence of a mixture of polymeric structures with the general formula $(NMG\text{-}Sb)_n\text{-}NMG$.[12] When further ESI-MS experiments were performed in both positive and negative modes, it was concluded that meglumine antimoniate primarily consisted of zwitterionic species, supported by negatively-charged 1:1 (*m*/*z* 364) and a 2:2 (*m*/*z* 765) peaks.[9] This same study also suggested that sodium stibogluconate consists of a mixture of oligomeric structures. This could be due to the inconsistencies in the synthesis of the pentavalent

antimonials, leading to a mixture of different compounds that would all fragment and ionize differently.

Despite the value of the information provided by these studies, they do not discriminate readily among the myriad of ways that these sugar derivatives can interact with the Sb center.[13] Mass spectrometric analysis is also complicated by the possibility that the dative Sb—O bonds are labile to rearrangement during ionization. Gaining insight into the structures of these drugs with direct spectroscopic studies is hampered by the lack of distinct spectroscopic signatures corresponding to the different possible binding modes of the ligands. As shown in Scheme 1.2, each ligand has five possible alkoxides for bonding, and in the case of D-gluconic acid, a carboxylic acid. This leads to a myriad of possible structures for the two drugs. If the pentavalent antimonials are a mixture of different compounds, each compound would likely have unique toxicity. By identifying the structures of the compounds in the putative mixture, one would be able to identify which components are the most active and/or toxic, providing a path to a more effective and safer drug. If the drugs are a mixture of compounds, there are likely equilibria involved which could be adding to the difficulties of investigating their structure in solution. These equilibria would also affect the activity/toxicity of the mixture as each component of equilibria would have different biological properties. This topic will be discussed further in depth in Chapter 4.

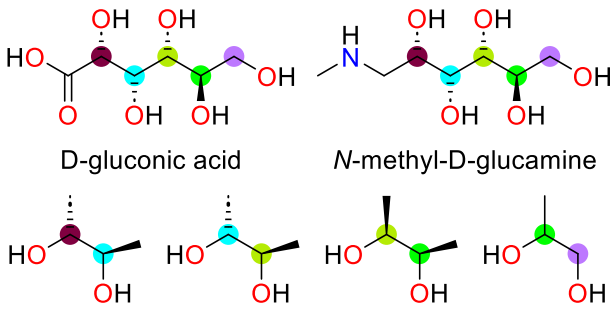

Scheme 1.2. Depiction of the relationship between the stereochemistry of the vicinal diols used in this study (*bottom*) and the stereochemistry of the *N*-methyl-D-glucamine and D-gluconic acid ligand precursors used in the pentavalent antimonial antileishmanial drugs (*top*).

1.4 Electronics and Bonding of Antimony

Antimony and other pnictogens have richly diverse chemistry. Due to this varied chemistry, pnictogen-containing compounds have served as systems to investigate trends in bonding and structure.[14-17] Antimony tends to form dative bonds with many elements, but Sb(V) is relatively oxophilic and forms many stable compounds with oxygen. Antimony-containing compounds with monodentate ligands also tend to be fluxional.[18] Computational methods, whether based on wavefunction theory or density function theory (DFT), provide a means of analyzing the canonical molecular orbitals (MOs),[19] natural bond orbitals (NBOs),[20] and the topology of the electron density via the Quantum Theory of Atoms in Molecules (QTAIM) to gain insight into the electronics and bonding of molecules.[21, 22] These methods have been used widely to investigate pnictogen-containing compounds, and this topic will be discussed further in Chapter 2.

Valence-shell electron pair repulsion (VSEPR) theory is a model used to predict the geometry of molecules based on their Lewis structure. The theory is based on the idea that electron pairs, either in bonds or lone pairs, will repel each other and that this repulsion is the primary driving force in the organization of ligands/substituents around a metal/metalloid center.[23] Since pairs of electrons repel each other electrostatically, the most stable geometry of a molecule is one which maximizes the distance between electron pairs. The primary metric for separation of electron pairs is bond angles, the larger the angle between electron pairs, the more stable that geometry. In VSEPR theory, it is generally accepted that electron pairs with a bond angle ≥ 120° do not repel each other. For a pentasubstituted, pentavalent (σ^5,λ^5) compound, the two most prevalent geometries are square pyramidal and trigonal bipyramidal. The bond angles in an ideal trigonal bipyramidal structure are 180°, 120°, and 90°. In a square pyramidal structure, the bond angles are all 90°. VSEPR theory predicts the trigonal bipyramidal geometry to be the most stable because it spaces out the electron pairs more than in a square pyramidal geometry.

The robustness of VSEPR theory is evidenced by the fact that the majority of main-group pentasubstituted, pentavalent molecules are shown to be trigonal bipyramidal either by spectroscopic studies or crystallography.[24] In fact, a supposed pentasubstituted, pentavalent molecule with a square pyramidal geometry was a point of great scientific intrigue.[25, 26] This will be discussed further in Chapter 3.

Three-center four-electron bonding (3c-4e) is a model of bonding invoked to explain certain types of hypervalent molecules. Bonding in electron-rich compounds

containing main-group elements often violates the Lewis octet rule. Originally, molecules like PF_5, ClF_3, and XeF_2 (10-valence electron systems) were described as dsp^3 hybridized. However, ab initio calculations of these molecules indicated that the d orbitals do not play a large role in the bonding of these molecules due to their high energy and diffuseness. To address the dissatisfactory description provided by hybridization in these cases, 3c-4e bonding was invoked.[27, 28] A 3c-4e bond is described as a bond with only two bonding electrons delocalized over three atoms; the remaining two electrons occupy a non-bonding orbital. This results in a bond order of 0.5 between each terminal atom and the central atom.

In the case of PF_5, which possesses a trigonal bipyramidal geometry, the 3c-4e bond is the linear bond between the two axial F atoms and the central P atom. The 3c-4e bond is formed from a p orbital of the central P atom and the σ orbitals of the two axial F atoms. Only the bonding and nonbonding orbitals are occupied, which leads each axial P—F bond to have a bond order of 0.5. This resulting lower bond order is evidenced by the fact that the axial P—F bonds are longer than the equatorial P—F bonds (1.577(5) Å and 1.534(4) Å respectively).[29]

A feature of 3c-4e bonding that is present in heteroleptic compounds is apicophilicity. Apicophilicity occurs in trigonal bipyramidal compounds and is the phenomenon in which the most electronegative substituents will occupy the axial positions. This occurs due to the non-bonding orbital of the 3c-4e bond concentrating electron density at the axial positions, which is stabilized by the electronegative substituents.

1.5 Physical Inorganic Techniques

As discussed above, insight into the structures of the pentavalent antimonials via classical spectroscopic studies are difficult, due to the complexity of the potential mixture. In addition, these spectroscopic techniques are often done on samples in solution which can be further plagued by equilibria. We sought to find a direct way to probe the Sb center using physical inorganic techniques. Of great interest to us was Mössbauer spectroscopy and X-ray absorption spectroscopy as they can provide information on the geometry, oxidation state, and structure of the Sb center.

Mössbauer spectroscopy is an absorption technique employing gamma rays. Radioactive decay generates a nucleus of interest in an excited nuclear state. Relaxation of this source nucleus to the ground state is accompanied by emission of a gamma ray photon that can then be absorbed by the sample, inducing a transition from the ground nuclear to excited nuclear state. The energies of the gamma rays are modulated using the Doppler effect by accelerating the source with respect to the sample. This technique can provide information on the number of metal sites present in a sample as well as the symmetry around those metal centers and has proved pivotal in understanding the structures of Fe-containing proteins and enzymes (e.g. iron-sulfur clusters, ferritin, and hemes).[30] This information can be obtained from three primary types of spectral information: isomer shift, quadrupole splitting, and magnetic hyperfine splitting. Isomer shift (δ, in mm s^{-1}) is a linear function of the electron density at the nucleus of interest, which is influenced by many factors including oxidation state, spin state, and the types of bonds/ligands present. The

isomer shift allows for determining overall oxidation state, or whether there are several oxidation states present in a sample. Quadrupole splitting (ΔE_Q) reveals the asymmetry of the electric field surrounding a metal center. If the metal center present is non-quadrupolar ($I \leq ½$) or possesses high symmetry (octahedral/tetrahedral), no quadrupole splitting is observed. If quadrupole splitting is observed, the spectrum from a sample can be compared to standards, providing insight into the overall geometry of the metal center. Magnetic hyperfine splitting is a result of the Zeeman Effect, which is the splitting of spectral lines into several components in the presence of a magnetic field. The extent of splitting is proportional to the magnetic field strength at the nucleus, which is dependent on the electron distribution around the nucleus. When taken together, these three parameters (isomer shift, quadrupole splitting, and hyperfine splitting) can directly provide structural information but are perhaps most powerful when the spectra of unknown compounds are compared to spectra of standards with known structures. ^{121}Sb is one of the primary elements probed by Mössbauer spectroscopy, along with ^{57}Fe.[30] We had hopes to use this technique to provide insight into the structures of the pentavalent antimonials, but study of spectra obtained on pentaphenylantimony proved to be less informative than we had hoped due to the wide line widths which made it difficult to reliably extract any quadrupole splitting information.

X-ray absorption spectroscopy (XAS) is a technique commonly used to determine the local geometry or electronic structure of chemical compounds.[31] XAS is sometimes referred to as an “inner-shell” spectroscopic technique as it probes the

core electrons of an atom unlike the more traditional electronic absorption techniques (e.g. UV-vis absorption) which probe the outer-shell or valence electrons of an atom. The energy required to excite a core electron is typically much higher than that needed to excite a valence electron, thus it requires high-energy photons. Photons with energy in the X-ray region of the spectrum tend to meet these requirements, which is why they are selected for the technique. Due to the wide range of X-ray energies required for an XAS instrument to probe multiple elements, a synchrotron source is typically used.

The choice of the energy of the X-rays used is determined by the specific element being probed. The ability to probe specific elements is one of the reasons this technique is so powerful. Common optical methods such as UV-vis absorption or fluorescence are not selective in this manner, making XAS ideal for gaining structural and electronic insight where other techniques are dissatisfactory. XAS measures the transitions from core orbitals of the element being probed to low-lying valence states. For the above reasons, XAS is often used to probe central metal atoms of coordination compounds. An XAS spectrum can be broken down into two primary regions: the X-ray absorption near-edge structure (XANES) region and the extended X-ray absorption fine structure (EXAFS) region. The XANES region can be further broken down into the pre-edge and rising edge regions which result from the initial excitation of the core electron (Figure 1.1). The EXAFS region results from the excitation of the core electron to energies greater than the threshold for electron release. The two methods provide complementary structural information, the XANES

spectra providing information on electronic structure, symmetry of the element probed, and its geometry; while the EXAFS spectra provide information on the types of ligands, number of ligands, and bond distances present in the compound.

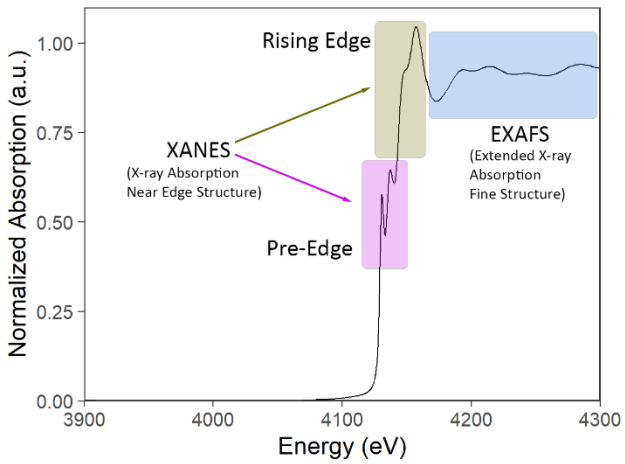

Figure 1.1. Schematic of a typical XAS spectrum.

X-ray absorption spectra are typically characterized by a sharp increase in absorption at specific X-ray photon energies (typically displayed in eV), which are characteristic of the element being probed. These sharp increases in absorption are referred to as absorption edges and correspond to the energy required to eject a photoelectron (Figure 1.1). There are several absorption edges for the element being probed, depending on which core electron is excited. When a photoelectron originates from a 1s core orbital, it is referred to as the K-edge. If a photoelectron originates from a 2s or 2p orbital, it is known as the L-edge, which further comprises three primary transitions. The L_1-edge of a spectrum is a result of a 2s electron being

excited, the L_2- and L_3-edges from the excitation of a 2p electron. There are other edges one can investigate, but this thesis will only discuss K-edge and L-edge XAS.

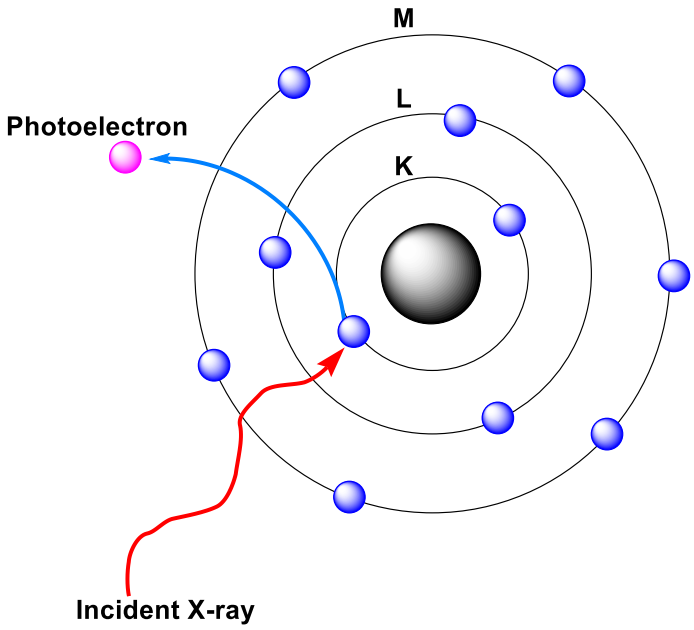

Figure 1.2. Schematic of the process of excitation and creation of a photoelectron.

1.6 Model Compounds

A common mechanism of gaining insight into molecular structures is the use of model compounds. This method has proved extremely fruitful in the determination of proteins, catalysts, and their active sites.[32, 33] To the best of our knowledge, there have been no attempts prior to those discussed in Chapter 4 to investigate the structures of the pentavalent antimonials through model compounds. As discussed above, the polyalcohol ligands employed in the synthesis of the pentavalent antimonials have a myriad of ways of interacting with the Sb atom. By synthesizing and characterizing compounds that contain chemical motifs similar to those that could

be present in the pentavalent antimonials, one can gain insight into the interactions present in the pentavalent antimonials by comparing the spectroscopic results of the model compounds to those of the pentavalent antimonials. For example, the ^{1}H NMR spectra of the pentavalent antimonials are difficult to interpret due to the large number of signals, many of which overlap. By analyzing the NMR spectra of model compounds, some chemical signals may prove diagnostic based on their chemical shifts or splitting patterns. These spectroscopic signatures could prove valuable in interpreting the complex NMR spectra of the pentavalent antimonials. This same overall method could be useful for other techniques like mass spectrometry and would not be limited to just NMR.

1.7 Conclusions

Leishmaniasis is a neglected tropical disease that affects millions of people. The current frontline treatments are the pentavalent antimonials meglumine antimoniate and sodium stibogluconate, two antimony-containing drugs with severe side-effects and mounting drug resistance. Despite their clinical use for nearly a century, their structures and mechanism of action are still not fully elucidated. Structural studies are hampered by the complexity of the chemical mixtures present in the drugs, making more common spectroscopic techniques less helpful. In the following chapters, our approach to combating these issues will be discussed. Chapter 2 will investigate the use of the quantum theory of atoms in molecules (QTAIM) in understanding and characterizing the types of bonding present between pnictogens (Group 15 elements) and oxygen. This will allow for a better understanding of what

bonding to expect in the pentavalent antimonials. Chapter 3 will explore the use of physical inorganic techniques in elucidating the geometry assumed by Sb centers. Pentaphenylantimony is used as a proof of concept to show that both solution- and solid-state XAS can shed light on the geometry around an Sb center. Chapter 4 will describe the use of model compounds to determine spectroscopic signatures present in Sb-diolate complexes. Structural and spectroscopic information on these model compounds will provide insight into the possible structures of the pentavalent antimonials. Finally, Chapter 5 will exploit the results of Chapter 4 to further understand the solid-state structures of Sb-diolate compounds. Information pertaining to the structures of our Sb-diolate model compounds will allow for further derivatization and understanding of the structures of the pentavalent antimonials. These are our first steps into determining the structures of the pentavalent antimonials in hopes to improve the treatment of patients suffering from leishmaniasis.

1.8 References

1. Duffin, J.; René, P., "Anti–moine; Anti–biotique": The Public Fortunes of the Secret Properties of Antimony Potassium Tartrate (Tartar Emetic). *Journal of the History of Medicine and Allied Sciences* **1991,** *46* (4), 440-456.
2. Diamond, A. W.; Fayad, V. C.; McKinley, P. S., COMMENTARY-Ipecac: an improved emetic for wild birds. *Journal of Field Ornithology* **2007,** *78* (4), 436-439.
3. Organization, W. H. *Leishmaniasis* [Fact sheet]. https://www.who.int/news-room/fact-sheets/detail/leishmaniasis (accessed 2023/05/26).
4. Aragão, H. D. B.; Vianna, G., Pesquizas sobre o Granuloma venereo. *Memórias do Instituto Oswaldo Cruz* **1913,** *5* (2), 211-238.

5. di Cristina, G.; Caronia, G., Über die Behandlung der inneren Leishmaniosis. *Deutsche Medizinische Wochenschrift* **1915,** *41* (14), 396-397.

6. Rogers, L., Tartar Emetic in Kala-azar. *British Medical Journal* **1915,** *2*, 197.

7. Cole, A. C. E., Kala-azar in East Africa. *Transactions of the Royal Society of Tropical Medicine and Hygiene* **1944,** *37* (6), 409-435.

8. Tapscott, R. E.; Belford, R. L.; Paul, I. C., Stereochemistry of tartrato(4-)-bridged binuclear complexes. *Coordination Chemistry Reviews* **1969,** *4* (3), 323-359.

9. Frézard, F.; Martins, P. S.; Barbosa, M. C. M.; Pimenta, A. M. C.; Ferreira, W. A.; de Melo, J. E.; Mangrum, J. B.; Demicheli, C., New insights into the chemical structure and composition of the pentavalent antimonial drugs, meglumine antimonate and sodium stibogluconate. *Journal of Inorganic Biochemistry* **2008,** *102* (4), 656-665.

10. Roatt, B. M.; de Oliveira Cardoso, J. M.; De Brito, R. C. F.; Coura-Vital, W.; de Oliveira Aguiar-Soares, R. D.; Reis, A. B., Recent advances and new strategies on leishmaniasis treatment. *Applied Microbiology and Biotechnology* **2020,** *104* (21), 8965-8977.

11. Headley, J. V.; Yong, M. S.; Brooks, P. W.; Phillips, A., Fast-Atom Bombardment Mass Spectrometry of the Organometallic Parasiticide, Meglumine Antimonate. *Rapid Communications in Mass Spectrometry* **1995,** *9* (5), 372-376.

12. Roberts, W. L.; McMurray, W. J.; Rainey, P. M., Characterization of the antimonial antileishmanial agent meglumine antimonate (Glucantime). *Antimicrobial Agents and Chemotherapy* **1998,** *42* (5), 1076-1082.

13. Gyurcsik, B.; Nagy, L., Carbohydrates as ligands: coordination equilibria and structure of the metal complexes. *Coordination Chemistry Reviews* **2000,** *203* (1), 81-149.

14. Jerzembeck, W.; Bürger, H.; Constantin, L.; Margulès, L.; Demaison, J.; Breidung, J.; Thiel, W., Bismuthine BiH_3: Fact or Fiction? High-Resolution Infrared, Millimeter-Wave, and Ab Initio Studies. *Angewandte Chemie International Edition* **2002,** *41* (14), 2550-2552.

15. Trubenstein, H. J.; Moaven, S.; Vega, M.; Unruh, D. K.; Cozzolino, A. F., Pnictogen bonding with alkoxide cages: which pnictogen is best? *New Journal of Chemistry* **2019,** *43* (36), 14305-14312.

16. Goicoechea, J. M.; Grützmacher, H., The Chemistry of the 2-Phosphaethynolate Anion. *Angewandte Chemie International Edition* **2018,** *57* (52), 16968-16994.

17. Twamley, B.; Sofield, C. D.; Olmstead, M. M.; Power, P. P., Homologous Series of Heavier Element Dipnictenes 2,6-$Ar_2H_3C_6E$=EC_6H_3-2,6-Ar_2 (E = P, As, Sb, Bi; Ar = Mes = C_6H_2-2,4,6-Me_3; or Trip = C_6H2-2,4,6-$^iPr_3$) Stabilized by *m*-Terphenyl Ligands. *Journal of the American Chemical Society* **1999,** *121* (14), 3357-3367.

18. Moc, J.; Morokuma, K., *Ab Initio* Molecular Orbital Study on the Periodic Trends in Structures and Energies of Hypervalent Compounds: Five-Coordinated XH_5 Species Containing a Group 15 Central Atom (X = P, As, Sb, and Bi). *Journal of the American Chemical Society* **1995,** *117* (47), 11790-11797.

19. Stowasser, R.; Hoffmann, R., What Do the Kohn−Sham Orbitals and Eigenvalues Mean? *Journal of the American Chemical Society* **1999,** *121* (14), 3414-3420.

20. Glendening, E. D.; Landis, C. R.; Weinhold, F., NBO 7.0: New vistas in localized and delocalized chemical bonding theory. *Journal of Computational Chemistry* **2019,** *40*, 2234–2241.

21. Bader, R. F. W., Atoms in Molecules. *Accounts of Chemical Research* **1985,** *18* (1), 9-15.

22. Bader, R. F. W., A Quantum Theory of Molecular Structure and Its Applications. *Chemical Reviews* **1991,** *91* (5), 893-928.

23. Gillespie, R. J.; Nyholm, R. S., Inorganic stereochemistry. *Quarterly Reviews, Chemical Society* **1957,** *11* (4), 339-380.

24. Gillespie, R. J., Fifty years of the VSEPR model. *Coordination Chemistry Reviews* **2008,** *252* (12-14), 1315-1327.

25. Lindquist-Kleissler, B.; Weng, M.; Le Magueres, P.; George, G. N.; Johnstone, T. C., Geometry of Pentaphenylantimony in Solution: Support for a Trigonal Bipyramidal Assignment from X-ray Absorption Spectroscopy and Vibrational Spectroscopic Data. *Inorganic Chemistry* **2021,** *60* (12), 8566-8574.

26. Schmuck, A.; Buschmann, J.; Fuchs, J.; Seppelt, K., Structure and Color of Pentaphenylbismuth. *Angewandte Chemie International Edition in English* **1987,** *26* (11), 1180-1182.

27. Pimentel, G. C., The Bonding of Trihalide and Bifluoride Ions by the Molecular Orbital Method. *The Journal of Chemical Physics* **1951,** *19* (4), 446-448.

28. Rundle, R. E., Electron Deficient Compounds. II. Relative Energies of ``Half-Bonds". *The Journal of Chemical Physics* **1949,** *17* (8), 671-675.

29. Hansen, K. W.; Bartell, L. S., Electron Diffraction Study of the Structure of PF_5. *Inorganic Chemistry* **1965,** *4* (12), 1775-1776.

30. Grandjean, F.; Long, G. J., Best Practices and Protocols in Mössbauer Spectroscopy. *Chemistry of Materials* **2021,** *33* (11), 3878-3904.

31. Yano, J.; Yachandra, V. K., X-ray absorption spectroscopy. *Photosynthesis Research* **2009,** *102* (2-3), 241-254.

32. Tolman, W. B., Using synthetic chemistry to understand copper protein active sites: a personal perspective. *JBIC Journal of Biological Inorganic Chemistry* **2006,** *11* (3), 261-271.

33. Harris, D. L., High-valent intermediates of heme proteins and model compounds. *Current Opinion in Chemical Biology* **2001,** *5* (6), 724-735.

Chapter 2

Exploring Oxygen—Pnictogen Bonding Using Electron Density Topology

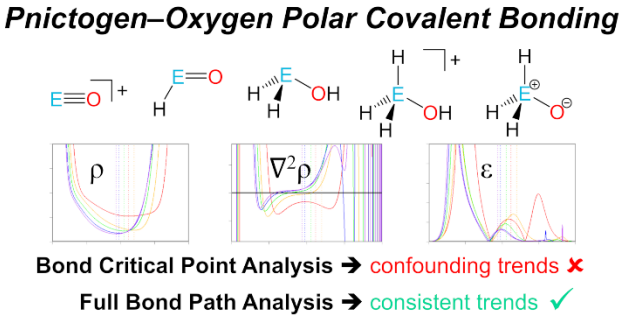

Published in part in: Lindquist-Kleissler, B.; Johnstone, T. C. *Inorg. Chem.*, **2021,** *60*, 1846.

2.1 Introduction

The chemistry of the pnictogens, or group 15 elements, varies greatly as you descend the group or family. From non-metallic N and P, through metalloids As and Sb, to metallic Bi.[1] Pnictogen-containing compounds display a wide variety of chemistry, as manifested in their catalytic abilities and their oftentimes unique chemical structures.[2-5] Previously, pnictogen-containing compounds have served as systems to investigate fundamental concepts of structure and bonding. These compounds have helped to reveal systematic variation across the periods, including the fluxionality of EH_5 species,[6] the interatomic angles of EH_3 compounds,[7] secondary (pnictogen) bonding capacity,[8] the structure and electronic properties of OCE^{-} anions,[9] and the multiple bonding in dipnictenes.[10] These variations have helped to inform our understanding of the roles of hybridization, relativity, and orbital overlap in main-group chemistry.[1] It is hard to overstate the importance of pnictogen-containing compounds in main-group chemistry.

It is well known that the pnictogens all readily interact with oxygen in richly varied ways. On a terrestrial scale, the oxides of nitrogen are vital in atmospheric chemistry and the oxides of the heavier pnictogens play an important role in geochemistry.[11] On a biological level, oxygen-phosphorus bonds are central to manifold processes, including bioenergetics (ATP/ADP), genetic information storage (DNA/RNA phosphodiesters), and cell function (protein phosphorylation).[12] The arsenic oxides are pivotal in the mechanisms of anticancer and antiparasitic drugs.[13] Some of the most widely used flame retardants feature compounds containing

oxygen-antimony bonds. As discussed in the Chapter 1, compounds featuring oxygen-antimony bonds are also used as antiparasitic drugs.[14] Bismuth oxides have been used in fireworks and dental fixtures, but perhaps the most widely known application of compounds containing oxygen-bismuth bonds is Pepto-Bismol (bismuth subsalicylate), which features important biological activity.[15]

The interactions of O—E bonds exhibit rich diversity, ranging from the formal triple bonds in EO^+ diatomic cations that are isoelectronic with N_2, to the O—E single bonds in species like hydroxylamine (H_2NOH) or phosphinous acid (H_2POH). R_3EO compounds, such as trimethylamine *N*-oxide and triphenylphosphine oxide, feature O—E bonding that has been the focus of long-standing discussion.[16-24] The amine-oxides are conventionally depicted with a polar single bond (O^-—N^+), but the heavier congeners are conventionally shown with a double bond (O=E). However, it is now well established that the d orbitals of these heavier pnictogens are too low in energy to participate in bonding.[1] Nonetheless, the distinct reactivity of the R_3EO species showcases the unique O—E interactions present in these compounds.[25]

There are a host of electronic structure analytical frameworks that have been used to analyze and rationalize the structures and reactivities of these different classes of oxygen-pnictogen compounds. The most common methods involve analysis of the canonical molecular orbitals (MOs) obtained from diagonalization of the Fock matrix. Alternative MO schemes, obtained by applying unitary transformations to the canonical MOs, have also be used to analyze oxygen-pnictogen bonding. A prominent example of this is natural bond orbital (NBO) analysis.[26] Typically, the

MOs used to investigate chemical bonding, both canonical and transformed, are obtained using the Hartree-Fock (HF) self-consistent field theory and can be modified to account for the influence of electron-electron correlation according to a variety of post-HF schemes (e.g. Møller-Plesset perturbation theory, configuration interaction, coupled-cluster theory, etc.). Alternatively, the Kohn-Sham orbitals obtained from density functional theory (DFT) calculations can be analyzed directly or following unitary transformation.[27]

A relatively less used strategy, that greatly complements these orbital-based analyses, is the topological analysis of the electron density. This method is commonly referred to as atoms in molecules (AIM) or the quantum theory of atoms in molecules (QTAIM).[28, 29] A notable difference between analysis of electron density and analysis of wavefunctions is that the former relies exclusively on a physical observable, which can be a great benefit. Typically, the electron density is obtained from wavefunction or DFT calculations, but refined charge densities from high-resolution X-ray diffraction allows experimental electron densities to be analyzed. As this thesis will make clear, we have a vested interest in the medicinal inorganic chemistry of pnictogen-containing species, thus we sought a framework to classify and categorize oxygen-pnictogen bonds through a topological analysis of the electron density. As mentioned above, many methods can be used to compare and contrast the bonding in these molecules, but topological analysis of the electron density is unique in that it remains agnostic to the origin of that electron density. I acknowledge that there have been isolated studies on subsets of oxygen-pnictogen compounds, but to the best of

my knowledge, no systemic investigation of the topology of the electron density of these compounds has been performed.

The details of the topological analysis of electron density (ρ) within the AIM framework have been extensively covered previously, and I refer the reader to those comprehensive resources for details.[28, 29] For ease of comprehension, I will briefly introduce those concepts necessary for the ensuing discussion. Two functions whose topologies are extensively probed are ρ and the Laplacian of the electron density ($\nabla^2\rho$), the latter of which is equal to the sum of the eigenvalues λ_1, λ_2, and λ_3 of the Hessian of ρ. The Hessian matrix comprises the partial second derivatives of ρ with respect to orthogonal spatial directions. A key feature of this analysis is the identification of topologically critical points in ρ or $\nabla^2\rho$. Critical points in ρ are points in three-dimensional space where the gradient of the electron density ($\nabla\rho$) vanishes. These critical points are classified according to the properties of the Hessian of ρ at this point in space, which are summarized by the rank and signature. The rank (ω) is the number of non-zero curvatures (Hessian eigenvalues) in ρ at the critical point, and the signature (σ) is the algebraic sum of the signs of the curvatures (Hessian eigenvalues) at the critical point. The vector field $\nabla\rho$ also features prominently in QTAIM. It comprises field lines that either (i) originate at infinity and terminate at a critical point in ρ or (ii) link two critical points in ρ. One of the most fascinating features of the topology of ρ is that the critical points and the gradient paths that link them recover our conventional notions of molecular structure, which is excellently depicted in some of Bader's earlier work.[30] Nuclear positions are reflected by critical

points in ρ with ω = 3 and σ = -3, known as a $(3,-3)_\rho$ critical points. A $(3,-1)_\rho$ critical point will lie between any two atoms engaged in a bonding interaction, and two unique gradient paths will link this $(3,-1)_\rho$ critical point to the two $(3,-3)_\rho$ critical points associated with the bonded atoms. These two gradient trajectories form a *bond path*, which is not to be mistaken for a bond, but often coincides with where a chemical bond would typically be drawn. The union of all the $(3,-3)_\rho$ critical points and bond paths comprise the molecular graph.

Due to the reliable manner in which known bonding interactions have mapped onto $(3,-1)_\rho$ critical points, many investigators use the presence of such a critical point as evidence of a bonding interaction between the atoms,[30] although dogmatic reliance on this relationship has been questioned.[31] Not only do topological analyses provide evidence of bonding, they can also shed light on the very nature of the bond in question.[32] A large variety of analyses can be performed to provide nuanced information on bonding, but most investigations follow a typical formula. They begin with a search of ρ to locate a $(3,-1)_\rho$ critical point linked to two $(3,-3)_\rho$ critical points via unique ∇ρ trajectories. Then, a variety of real-space functions are evaluated at the $(3,-1)_\rho$ critical point. Although a huge array of real-space functions can be employed, the most widely used and robust are: ρ, $\nabla^2\rho$, and the ellipticity ($\varepsilon = \lambda_1/\lambda_2 - 1$). The value of ρ at the $(3,-1)_\rho$ critical point tends to reflect the strength of the bond and the bond order. The Laplacian reflects local concentrations and depletions in ρ. Typically, a stronger or higher-order covalent bond gives values of $\nabla^2\rho$ that are negative, while closed-shell interactions (e.g. ionic or dative bonding) feature positive values of $\nabla^2\rho$

at the $(3,-1)_\rho$ critical point. Finally, ε describes the extent to which ρ is preferentially accumulated in the plane defined by the eigenvectors of the Hessian associated with λ_1 and λ_3.[33, 34] Note that, at the $(3,-1)_\rho$ critical point, λ_1 is the negative curvature of the greatest magnitude and λ_3 is the positive curvature in the direction of the bond path. For bonds with cylindrical σ symmetry, $\varepsilon = 0$, whereas for bonds with elliptical π symmetry, $\varepsilon > 0$.

One important aspect of QTAIM, which supports the views of the anti-dogmatists, is that many of the relationships identified between the nature of a bond and values of ρ, $\nabla^2\rho$, and ε at $(3,-1)_\rho$ critical points of covalent bonds were established using relatively non-polar bonds between first- and second-period elements. Later studies of polar covalent bonds and bonds involving heavier elements have shown that reliance on the values of these functions at the $(3,-1)_\rho$ critical point alone can be misleading.[35-42] We observed this inconsistency during our own investigation of oxygen-pnictogen bonding, and as discussed later in this chapter, the values of ρ, $\nabla^2\rho$, and ε at the $(3,-1)_\rho$ critical points of a variety of O—E bonds did not trend as expected. We found that we can recover the expected trends if one analyzes these functions *along the length of the bond path*, rather than solely at the $(3,-1)_\rho$ critical point. Not only does this provide insights into the bonding of these molecules, this bond path topological analysis also reveals patterns that are characteristic of each of the bond types explored herein (O—E, O=E, O≡E, O^{-}—E^{+}). Our studies show that the same patterns are produced regardless of whether ρ is obtained from coupled-

cluster singles doubles (CCSD) or DFT calculations. The patterns also persist upon substitution with organic groups.

2.2 Results and Discussion

Classical Examples/References

As mentioned above, the trends established between bond types and the values of the real-space functions investigated at $(3,-1)_\rho$ critical points were initially observed in relatively non-polar bonds between light atoms. A classical series investigated by Bader was ethane, ethene, and ethyne, which all feature a $(3,-1)_\rho$ critical point between the two carbon atoms. Visualizing ρ along the bond path reveals the local minimum, the critical point, which lies exactly halfway between the two carbon atoms for each molecule (Fig. 2.1A). It is important to note that the bond distances were normalized to unit length in Figure 2.1, to facilitate the comparison of species with different bond lengths. The value of ρ at the $(3,-1)_\rho$ critical point (ρ_b) tracks with bond order and steadily increases from single to double to triple bond (from ethane through ethene to ethyne). For all three molecules, the value of $\nabla^2\rho$ at the $(3,-1)_\rho$ critical point ($\nabla^2\rho_b$) is negative, as expected for a covalent bond in which electron density is locally concentrated between the nuclei (Fig. 2.1B). $\nabla^2\rho_b$ also becomes increasingly negative from single to double to triple bond. Finally, the ellipticity at the $(3,-1)_\rho$ critical point (ε_b) is zero for the cylindrically symmetric single and triple bonds of ethane and ethyne, but non-zero for ethene because of the preferential

concentration of electron density above and below the plane of the molecule (Fig. 2.1C).

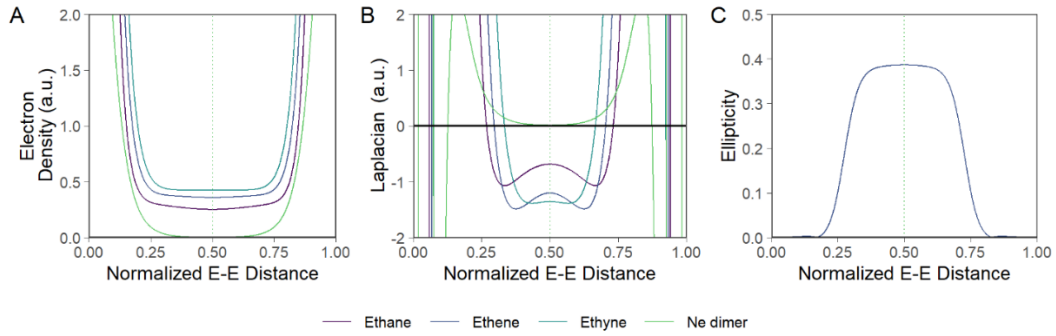

Figure 2.1. Plots of (A) ρ, (B) $\nabla^2\rho$, and (C) ε as a function of the normalized C—C (for ethane, ethene, and ethyne) or Ne—Ne (for Ne dimer) bond length for a series of reference compounds. For (C), note that ethane, ethene, ethyne, and Ne_2 have $\varepsilon = 0$ along the length of the bond. Orbital-optimized electron densities were obtained from single-point CCSD/ANO-RCC-QZP calculations at experimental geometries extracted from the NIST CCCDB.[43]

The covalent bonding in the ethane/ethene/ethyne series is fundamentally different in nature from the bonding that is present in the van der Waals molecule Ne_2.[44] Ne_2 still features a $(3,-1)_\rho$ critical point between the two nuclei, but the value of ρ_b is exceedingly small, reflecting the weak strength of the bond. The value of $\nabla^2\rho_b$ is negligibly small and positive, consistent with the non-covalent nature of the interaction in Ne_2. As expected, $\varepsilon_b = 0$ for the cylindrically symmetric Ne_2. The values of these functions at the $(3,-1)_\rho$ critical points are summarized in Table 2.1.

Table 2.1. Values of real-space functions at $(3,-1)_\rho$ critical points of reference compounds[a].

	ρ_b (a.u.)	$\nabla^2\rho_b$ (a.u.)	ε_b
Ethane	0.252	-0.686	0.000
Ethene	0.359	-1.202	0.387
Ethyne	0.425	-1.354	0.000
Ne dimer	0.002	0.013	0.000

[a]Electron densities obtained from orbital-optimized single-point CCSD/ANO-RCC-QZP calculations.

Panel Selection

The initial goal of this work was to establish the periodic trends that exist in oxygen-pnictogen bonds across group 15 and across the accessible bond orders. It is well known that oxygen can readily form nominal triple, double, and single bonds with the pnictogens as discussed previously. We elected to choose five classes of compounds: EO^+, HEO, H_2EOH, H_3EOH^+, and H_3EO (Scheme 2.1). The EO^+ cations are isoelectronic with N_2 and feature a triple bond. The HEO species exhibit a canonical oxygen-pnictogen double bond. The H_2EOH species feature an oxygen-pnictogen single bond. To establish whether the valence of the pnictogen influences our results, the pentavalent H_3EOH^+ species, which also contain formal O—E single bonds, were investigated. The final class of compounds could naively be considered as the pentavalent analogues of the HEO compounds given that they are often written as having double bonds (e.g. $Ph_3P{=}O$), but it is now well accepted that the EO bonds in these compounds are distinct from either conventional single or double bonds.[18]

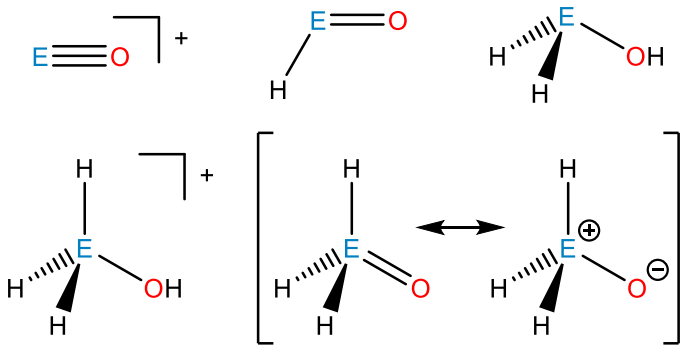

Scheme 2.1. Structures of the classes of compounds investigated. E = N, P, As, Sb, Bi.

The geometries of these compounds were optimized at the MP2/def2-QZVPP level of theory, which provides structures that agree with those that have been experimentally determined by spectroscopic or diffractometric methods (Table A.1). Note that the def2-QZVPP basis set[45] used in the geometry optimizations employs effective core potentials (ECPs) to address relativistic effects, which become particularly important for the antimony and bismuth compounds due to their size. The final electron densities were obtained at the MP2-optimized geometries from orbital-optimized CCSD/ANO-RCC-QZP single-point energy calculations. For these calculations, the second-order Douglas-Kroll-Hess (DKH) method was used in conjunction with a relativistically contracted, correlation-consistent, all-electron, quadruple-ζ atomic natural orbital basis set to account for relativistic effects.[46, 47]

Critical Point Analyses of Oxygen-Pnictogen Compounds

The first step in this analysis was to analyze ρ for all 25 compounds in Scheme 2.1. These analyses identified clear $(3,-1)_\rho$ critical points between the oxygen

and pnictogen atoms for all compounds. To continue the conventional analysis, ρ_b, $\nabla^2\rho_b$, and ε_b were evaluated at each $(3,-1)_\rho$ critical point (Figure 2.2, Table A.2). Among the E = N species, ρ_b decreases steadily from triply bonded NO^+ to doubly bonded HNO to singly bonded H_2NOH and H_3NOH^+ (Figure 2.2A). The two singly bonded species exhibit relatively similar values of ρ_b, with that of H_3NOH^+ being slightly higher. The value of ρ_b for H_3NO lies between that of the doubly and singly bonded species, albeit more closely to the single-bond values. The same trend is broadly observed when E = P, As, Sb, or Bi, although the range of values is much narrower. The EO^+ species consistently exhibit a ρ_b value higher than that of HEO, which is in turn higher than those of H_2EOH and H_3EOH^+. Among the singly bonded species, ρ_b is consistently greater for H_3EOH^+. One significant difference from the N compounds is that the heavier H_3EO species all feature ρ_b values greater than those of the doubly bonded HEO species. The ρ_b value for H_3EO progressively approaches the value for EO^+ as the family is descended. Comparing across the family within each class of compounds, we observe a systematic decrease in ρ_b with increasing atomic number, consistent with the expected decrease in orbital overlap in the bonds involving the large, heavy atoms. The dramatic change from N to P followed by more subtle variation further down the family is consistent with the generally observed principle that bonding between second-period elements differs greatly from that of the heavier elements, which are generally more similar. Nonetheless, there is a consistent trend across the whole family. Similar trends exist among the atomic charges obtained by integrating electron density within the topologically defined

atomic basins (Table A.3). Note that, unlike the heavier pnictogens, nitrogen is more electronegative than H, so for all classes of compounds with E—H bonds, the nitrogen members have negative charges. Among the heavier elements, the O—P charge separation is consistently greatest and those of the remaining species differ little. There is also little variation across bond types, with the exception that all charge separations are greater for the E(V) species, as expected.

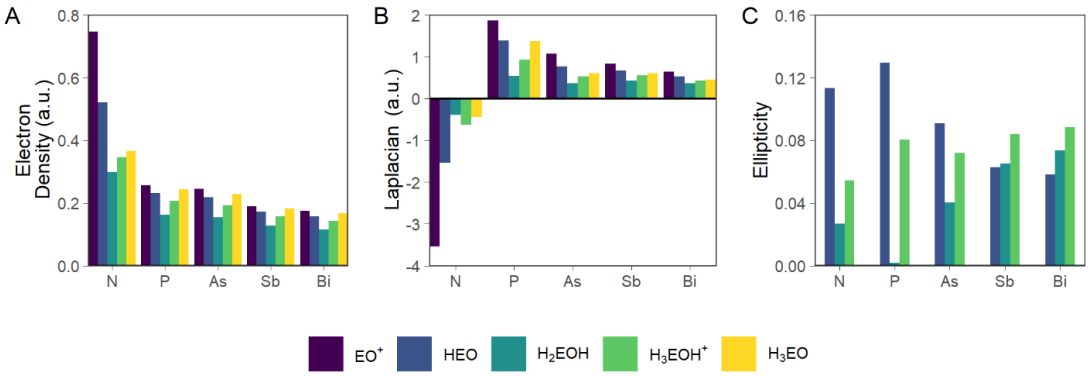

Figure 2.2. Values of (A) ρ_b, (B) $\nabla^2\rho_b$, and (C) ε_b for all 25 species grouped by pnictogen and colored by compound type. For (C), note that all EO^+ and H_3EO compounds have $\varepsilon = 0$. Note that ρ_b, $\nabla^2\rho_b$, and ε_b are the values of ρ, $\nabla^2\rho$, and ε at the (3,-1) critical point in ρ.

A similar consistent trend is not found among the values of $\nabla^2\rho_b$ (Figure 2.2B). Among the E = N species, the $\nabla^2\rho_b$ values trend as expected. All compounds have $\nabla^2\rho_b < 0$, consistent with a covalent interaction between the N and O atoms. For the triply bonded NO^+, $\nabla^2\rho_b$ is the most negative, followed by HNO, and then H_3NOH^+ and H_2NOH. The $\nabla^2\rho_b$ value for H_3NO lies between the values for the two singly bonded species. These values vary with bond order in the same way as those of ethane, ethene, and ethyne (Table 2.1). For all compounds of the heavier elements,

however, $\nabla^2\rho_b > 0$. The pattern among the phosphorus compounds is nearly the mirror image of that for the nitrogen compounds. PO^+ has the most positive value of $\nabla^2\rho_b$, followed by HPO and then H_3POH^+ and H_2POH. H_3PO has a value of $\nabla^2\rho_b$ between that of the singly and doubly bonded compounds. This trend of positive $\nabla^2\rho_b$ values is displayed by all of the heavier pnictogen series, with the absolute values of the Laplacian gradually decreasing down the family. The value of $\nabla^2\rho_b$ is often taken as a strong indicator of the nature of the bond, with negative values suggesting an open-shell, or covalent, interaction and positive values suggesting a closed-shell interaction. As with ρ_b, the $\nabla^2\rho_b$ values highlight the distinction between the bonding in oxygen–nitrogen compounds and that in all of the other oxygen–pnictogen compounds. However, in contrast to ρ_b, which only signified a difference in the magnitude of the interaction, $\nabla^2\rho_b$ appears to suggest a fundamentally different kind of interaction. The data could be interpreted as suggesting that the formally triply bonded PO^+ does not have a covalent bond. As with ρ_b, the spread of $\nabla^2\rho_b$ values across the different bond types decreases dramatically down the family.

In an effort to gain further insights into the variation in bonding across these series, and to find metrics that provide greater discriminatory power for the O—E bonds of the heavier pnictogens, we determined the values of ε_b (Figure 2.2C). Among the nitrogen-containing molecules, ε_b takes on the expected value of 0 for the cylindrically symmetric NO^+. For the doubly bonded, π-symmetric HNO, ε_b takes on a positive value, albeit one lower than that of the C=C bond in ethene (Table 2.1). For the singly bonded H_2NOH and H_3NOH^+, ε_b does not assume the expected value of 0

(cf. ethane, Table 2.1) but the magnitude is nonetheless less than that of HNO. As was the case for ρ_b and $\nabla^2\rho_b$, the magnitude of ε_b of H_3NOH^+ is slightly greater than that of H_2NOH. Finally, for the cylindrically symmetric H_3NO, $\varepsilon_b = 0$ as expected. For the heavier pnictogens (E = P, As, Sb, or Bi), $\varepsilon_b = 0$ for the cylindrically symmetric EO^+ and H_3EO species, as expected. Moreover, the HEO compounds feature positive ε_b values that decrease in magnitude down the family, as would be expected based on the decreased efficiency of multiple bonding as the family is descended. Among the singly bonded species, however, the ε_b values do not trend as expected. H_2POH features an ε_b of approximately zero, closer to expectation than H_2NOH, but for H_3POH^+, ε_b is over half that of the doubly bonded HPO. As the pnictogen increases in atomic number, the ε_b values for the singly bonded species consistently *increase*, and for Sb and Bi, they overtake the value of the corresponding HEO compound. An argument can be made for an expected increase in ε_b as the atomic number of E in H_2EOH increases because the E—H σ* orbital lowers in energy, facilitating a lone pair (O) to σ* (E—H) transition. It is nevertheless surprising that an increase in ε_b via this mechanism would cause the ε_b values of H_2EOH to overtake those of HEO, with formal O=E double bonds.

Bond Path Analyses of Oxygen—Pnictogen Compounds

To gain further insight into the anomalous trends observed in the values of the real-space functions evaluated at the $(3,-1)_\rho$ critical points, ρ, $\nabla^2\rho$, and ε were evaluated along the entire length of the O—E bond (Figure 2.3). To facilitate the comparison of species with differing bond lengths, the O—E distances of all

compounds were normalized to unit length. Along each bond path, a clear minimum is observed in ρ, coincident with a $(3,-1)_\rho$ critical point (Figure 2.3A–E). The difference in electronegativity of the bonded elements imparts polarity on the bond as reflected in the skewed distribution of ρ along the bond path. Among the nitrogen-containing species, as the bond order decreases, the bond lengthens, the electron density distribution trends toward being more symmetric, and the $(3,-1)_\rho$ critical point moves toward the midway point of the bond. For the heavier pnictogens, the longer bonds vary less in length across bond orders, and the trend is less pronounced. In all compound classes, as the pnictogen increases in size, the bond length increases and the proportion of the bond attributable to oxygen decreases, which is manifested as a gradual migration of the critical point toward the oxygen along the normalized bond. The location of the $(3,-1)_\rho$ critical point is marked with a dashed vertical line in all panels of Figure 2.3, and the intersection of the dashed line with the solid curve provides the values depicted in Figure 2.2 and collected in Table A.2. As noted above, the values of ρ_b do indeed follow the expected trends, but the full curves depicted in Figure 2.3 better capture the gradual variation in ρ that occurs across the pnictogen family.

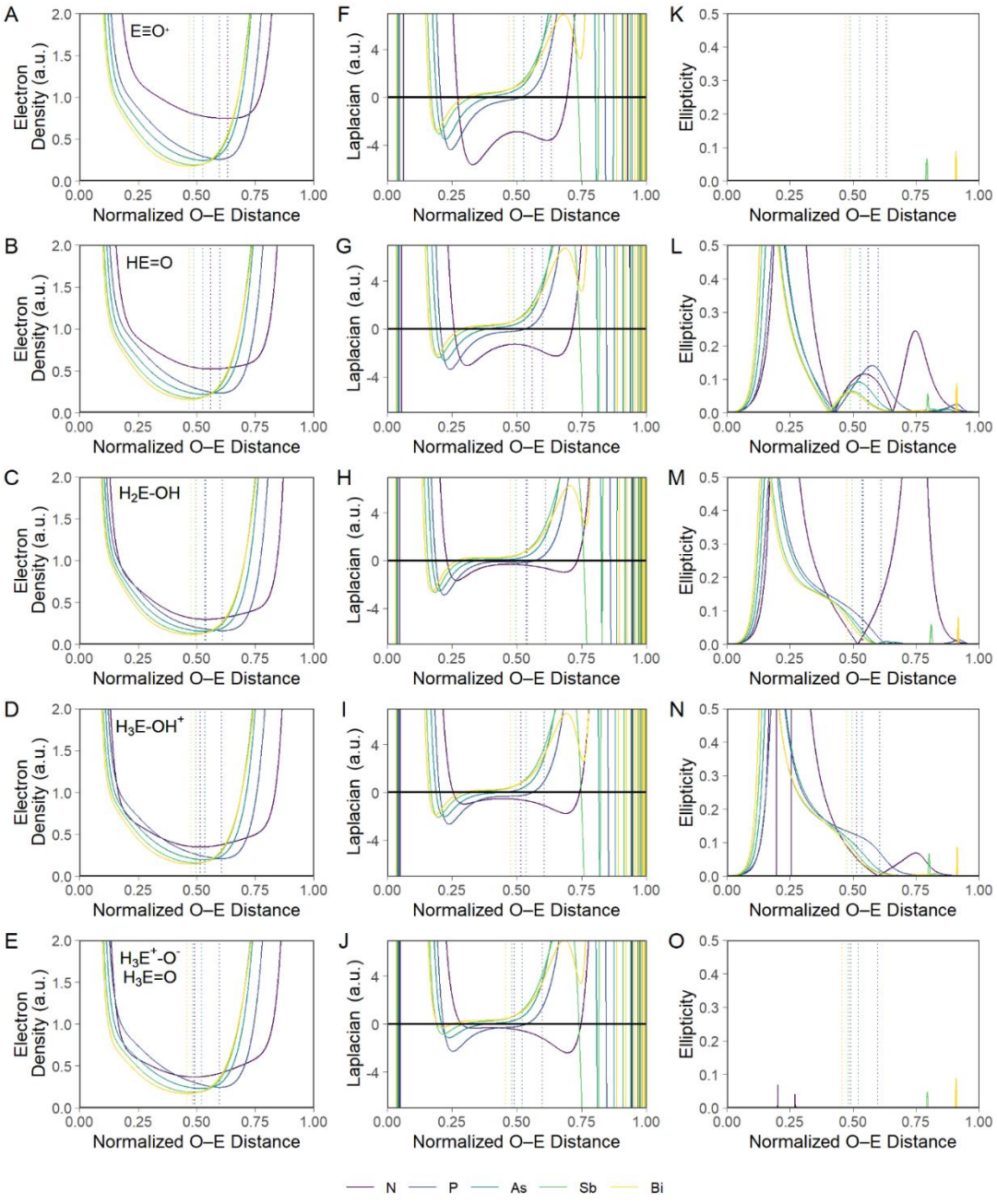

Figure 2.3. Evaluation (CCSD/ANO-RCC-QZP//MP2/def2-QZVPP) of electron density, Laplacian, and ellipticity along the normalized oxygen–pnictogen bond paths of different compounds (O at 0.0 and E at 1.0). Rows of panels feature data for a class of compounds: EO^+ (A,F,K); HEO (B,G,L); H_2EOH (C,H,M); H_3EOH^+ (D,I,N); and H_3EO (E,J,O), where E is a pnictogen. For (K) and (O), note that all compounds have $\varepsilon = 0$ along the length of the bond. Dashed vertical lines represent the location of the bond critical point.

Analysis of the plots of $\nabla^2\rho$ for the nitrogen compounds (Figure 2.3F–J) reveals that they have overall shapes similar to those of the curves for ethane, ethene, and ethyne (Figure 2.1B). It should be noted that the concentrations of nearly vertical lines near 0 and 1 result from the oscillation of $\nabla^2\rho$ across the core electronic shells. As in the C—C bonded compounds, the valence region of the Laplacian features a prominent region of negative values in the internuclear space, reflecting a local concentration of electron density between the bonded atoms, as expected for a covalent bond. Also as expected, as bond order decreases, the magnitude of the negative Laplacian values in the internuclear region broadly decreases. In contrast to the symmetric $\nabla^2\rho$ curves for the C—C species (Figure 2.1B), those of the nitrogen-containing species are asymmetric. For NO^+, HNO, and H_2NOH, the local minimum proximal to the oxygen atom assumes more negative values than the local minimum proximal to the nitrogen. Moreover, whereas the $(3,-1)_\rho$ critical points of the C—C species are all coincident with the central local maximum of the $\nabla^2\rho$ curve (Figure 2.1B), the critical point occurs at differing locations along the $\nabla^2\rho$ curve for the different nitrogen compounds (Figure 2.3F–H). For NO^+, the critical point is nearly coincident with the local minimum proximal to the nitrogen, whereas for H_2NOH it is nearly at the local maximum. It is also noteworthy that the curves for H_3NOH^+ and H_3NO are even further skewed (Figure 2.3I,J); for the latter, the local minimum proximal to oxygen has almost vanished.

The $\nabla^2\rho$ curves for all the heavier pnictogen compounds feature a common pattern that is, as expected, distinct from that of the nitrogen compounds. A single

local minimum exists and is proximal to the oxygen. The presence of a single local minimum in $\nabla^2\rho$ along the bond path connecting second-period elements with third- or greater-period elements has been previously reported.[36-42] In the valence region, the value of $\nabla^2\rho$ increases from the oxygen-proximal minimum, passes through an inflection point near the midway point of the bond with $\nabla^2\rho \approx 0$, and then continues to increasingly positive values near the pnictogen. Among the phosphorus compounds, as the bond order decreases from PO^+ to HPO to H_2POH and H_3POH^+, the Laplacian curve progressively flattens in the vicinity of the inflection point. This flattening of the curve delays the onset of the rise to increasingly positive $\nabla^2\rho$ values proximal to the pnictogen and consequently, the value of $\nabla^2\rho_b$ gradually diminishes in magnitude, as captured in Figure 2.2B. A feature not captured by the $\nabla^2\rho_b$ values, as shown in Figure 2.2B, is the decrease in the magnitude of the local minimum proximal to oxygen with decreasing bond order. Finally, the various H_2EOH and H_3EOH^+ series provide an opportunity to assess the influence of oxidation state on the Laplacian within a single bond type (nominal O—E single bond). The E(V) atoms have greater electronegativities than the corresponding E(III) atoms, resulting in a diminished electronegativity difference between the pnictogen and oxygen for H_3EOH^+ as compared to H_2EOH. As a result, the O—E bond in H_3EOH^+ would be expected to be more covalent. Although the differences between the compounds of the heavier elements are very small, we do indeed see this expected trend in the Laplacian, whereby that of H_3NOH^+ is more negative than that of H_2NOH at the $(3,-1)_\rho$ critical point (Figure 2.2B) or along the length of the bond path (Figure 2.3H,I).

Within a given class of compounds, as the pnictogen becomes heavier, the $\nabla^2\rho$ curve generally shifts up and to the left, with both the oxygen-proximal minimum and inflection point occurring progressively closer to the oxygen atom (smaller normalized O–E distances) and progressively more positive $\nabla^2\rho$. We believe that the overall shape of the $\nabla^2\rho$ curve better captures the variation that occurs across compound classes and element periods than the values of $\nabla^2\rho_b$ alone. It is interesting to note that although $\nabla^2\rho_b$ for the singly bonded Sb—O and Bi—O species is similar to $\nabla^2\rho_b$ for the corresponding H_3EO compounds, the magnitude of the oxygen-proximal $\nabla^2\rho$ minimum is greatly reduced for the latter. Given that monomeric stibine oxides and bismuthine oxides are greatly underexplored as compared to compounds with Sb—O and Bi—O single bonds, analysis of $\nabla^2\rho$ along the length of the bond path may discriminate comparative stability and bond strength better than $\nabla^2\rho_b$.

In the case of ε, analysis along the full bond path (Figure 2.3K–O) affords an opportunity to understand the apparently counterintuitive results provided by analysis of ε_b (*vide supra*). As with ethyne (Table 2.1), the triple-bonded EO^+ molecules have $\varepsilon = 0$ along the entire length of the bond path (Figure 2.3K). The spikes in the baseline appear to arise during the numerical processing of the electron density data; note that they are absent from the DFT data, as shown in Figure A.1 (*vide infra*). For the HEO species, ε achieves a local maximum near the $(3,-1)_\rho$ critical point (Figure 2.3L). This maximum is bracketed by roots on either side. The curves also feature a prominent oxygen-proximal maximum and a much smaller pnictogen-proximal maximum. The presence of a local maximum near the $(3,-1)_\rho$ critical point is a feature

shared by the ε curve for ethene (Figure 2.1C). We note that the prominent oxygen- and pnictogen-proximal maxima in Figure 2.3L occur in regions of the bond where $\nabla^2\rho$ has local minima (Figure 2.3G). This behavior has been noted previously in polar bonds and has been ascribed to deviation of the eigenvector associated with λ_2 from the plane of the molecule.[35, 40] HNO, which has a well-defined nitrogen-proximal minimum in $\nabla^2\rho$, features a correspondingly well-defined maximum in ε. In contrast, the HEO compounds with heavier pnictogens, which do not feature a pnictogen-proximal valence minimum in $\nabla^2\rho$, have ε values close to 0 in the pnictogen-proximal valence region. We also highlight that, in general, the value of ε is expected to deviate from 0 in regions far from the $(3,-1)_\rho$ critical point of any bond if there is an asymmetric distribution of electron density around the atoms involved in that bond. For example, lone pairs on bonded atoms can skew electron density along a bond path from cylindrical symmetry proximal to that atom.

The singly bonded H_2NOH and H_3NOH^+ both also feature maxima in ε near the regions where their $\nabla^2\rho$ curves have local minima. In contrast to HNO, however, ε for these two compounds reaches a value of zero between these maxima. This situation contrasts with that of ethane, for which ε = 0 along the length of the bond (Figure 2.1C). Nevertheless, for these O—N singly bonded species, ε trends toward 0 in the vicinity of the $(3,-1)_\rho$ critical point. The fact that the $(3,-1)_\rho$ critical points for these molecules do not coincide exactly with their respective minima in ε explains the non-zero ε_b values, as shown in Figure 2.2C and Table A.2. The singly bonded species of the heavier pnictogens feature a slightly different pattern. As with the

nitrogen species, they feature a large maximum near the oxygen atom, where $\nabla^2\rho$ has a local minimum. As with the heavier HEO species, however, there is no prominent maximum in ε near the pnictogen (nor is there a corresponding pnictogen-proximal minimum in $\nabla^2\rho$). Moreover, unlike the nitrogen-containing species, the oxygen-proximal feature in ε for the heavier H_2EOH and H_3EOH^+ compounds bears a significant shoulder distal to the oxygen. For all compounds with E = P, As, Sb, or Bi, this shoulder extends into the vicinity of the $(3,-1)_\rho$ critical point before decaying to zero in the valence region of the pnictogen. The presence of this shoulder results in the non-zero values of ε_b reported for these species in Figure 2.2C and accounts for their deviation from the expected value of $\varepsilon_b \approx 0$. The steady migration of the critical point toward the oxygen, as group 15 is descended, results in ε_b assuming progressively larger numbers, even surpassing those of the corresponding HEO species for E = Sb and Bi. The one apparent exception to the pattern is H_2POH, which is in fact the only one of these compounds to show the expected $\varepsilon_b \approx 0$ in Figure 2.2C. Analysis of Figure 2.3M reveals that the overall form of the curve is the same as for the other compounds, but that the critical point happens to lie just outside of the shoulder.

The behavior of ε for the H_3EO compounds (Figure 2.3O), which are known to have bonds of order greater than 1,[25] highlights that this parameter does not report on bond order per se but rather on the preferential concentration of charge within a plane containing the bond. The ε value of 0 for the H_3EO compounds does not rule out a bond order greater than 1, but it does imply that any interactions additional to a

single O—E bond are cylindrically symmetric. Previous orbital-based analyses of pnictine oxides of the general form X_3EO have suggested that donation from two orthogonal p-type lone pairs on the terminal oxygen atom into three E–X antibonding orbitals produces the characteristic strengthening of the O—E interaction but maintains cylindrical symmetry about the O—E bond.[18] It is interesting to note that protonation of H_3EO to form H_3EOH^+ "ties up" one of these lone pairs, disrupting the cylindrical symmetry of the oxygen–pnictogen interaction as revealed by the behavior of ε along the bond path.

In summary, analysis of the patterns of ρ, $\nabla^2\rho$, and ε across the length of the bond path provides a means of differentiating different types of oxygen–pnictogen bonds and a richer source of information about chemical bonding than analysis of these functions at the $(3,-1)_\rho$ critical point alone. Analysis of ρ along the bond path reveals the asymmetry of the electron density distribution that is not captured by ρ_b. As expected on the basis of increasing orbital diffuseness as the family is descended, the asymmetry in ρ along the bond path decreases with increasing atomic number of E. Analysis of $\nabla^2\rho$ not only provides a better means of discriminating bond types than $\nabla^2\rho_b$, but it better captures the systematic variation in bonding across the compounds and periods. For example, charge concentration between the pnictogen and oxygen across the entire valence region increases with bond order and decreases down the family, as expected from the increase in orbital overlap with bond order and the decrease in O—E orbital overlap as E becomes larger. Finally, the behavior of ε across the bond length provides an explanation for the seemingly counter-intuitive

trends afforded by ε_b. Axially symmetric molecules (EO^+ and H_3EO) that feature cylindrically symmetric overlap of s and p orbitals along the O–E bond exhibit $\varepsilon = 0$ along the entire bond. The locally cylindrically symmetric overlap of atomic orbitals in molecules with O—E single bonds (H_2EOH and H_3EOH^+) results in ε reaching 0 in the valence region, although not necessarily at a location coincident with the $(3,-1)_\rho$ critical point. The lack of overall axial symmetry in these molecules relaxes the requirement that $\varepsilon = 0$ along the entire bond. The overlap of p-orbitals in the doubly bonded HEO species results in accumulation of electron density above and below the plane of the molecule and produces a maximum in ε in the vicinity of the $(3,-1)_\rho$ critical point. Because of the decreased propensity of heavier elements to engage in multiple bonding, the value of ε assumed at this local maximum decreases with increasing atomic number of E.

Extension to DFT Methods

The analyses discussed above revealed that the overall shapes of ρ, $\nabla^2\rho$, and ε along the bond paths contain important information, but the electron densities used for these analyses were obtained at the computationally expensive orbital-optimized CCSD level of theory in an effort to best approximate the true electron densities. We were interested in seeing whether or not these patterns and trends would persist when the electron densities were calculated at the much more computationally efficient DFT level. Although DFT has recently been criticized as deviating from the pursuit of the true electron density, common hybrid functionals typically perform well in reproducing the densities of high-level correlated calculations.[48-53] The geometries of

the 25 compounds from Scheme 2.1 were optimized at the PBE0/def2-TZVPP level of theory, which employs ECPs.[45] The electron densities for these newly optimized geometries were obtained with single-point energy second-order DKH calculations using the PBE0 functional and an all-electron, relativistically contracted Ahlrichs-style triple-ζ basis set with extensive polarization functions. Electron densities were obtained for EO^+, HEO, H_2EOH, H_3EOH^+, and H_3EO with E = N, P, As, and Sb (Bi was not defined in the all-electron basis set used). Plots of ρ, $\nabla^2\rho$, and ε as a function of normalized O—E distance are presented in Figure A.1 and recover all of the trends observed in Figure 2.3.

Extension to Organic Derivatives

Having observed that the trends are robust enough for DFT calculations in the previous section, we analyzed the topology of E—Me and E—Ph derivatives of two of the classes of compounds: H_3EO and H_3EOH^+. For the Me_3EO species (Figure 2.4A,B), the patterns in ρ and $\nabla^2\rho$ are essentially identical to those of the H_3EO species. For E = P, As, and Sb, there is a single minimum in $\nabla^2\rho$ in the valence region proximal to the oxygen and the value of $\nabla^2\rho$ at this minimum is slightly more negative than for the corresponding H_3EO (Figure 2.4B) as expected for a stronger covalent bond. For H_3NO, the oxygen-proximal minimum in $\nabla^2\rho$ is essentially absent (Figure 2.3J), whereas for Me_3NO, it is slightly more pronounced (Figure 2.4B). The values of ε are effectively zero along the lengths of the bond paths of all of these cylindrically symmetric compounds (Figure 2.4C), although there are spikes that arise

during numerical processing of the data. For the Me_3EOH^+ species, featuring single bonds, the situation again mirrors that of the H_3EOH^+ species (Figure 2.4D-F). For Me_3NOH^+, there is a more pronounced oxygen-proximal minimum in $\nabla^2\rho$ than in Me_3NO and the absolute value of $\nabla^2\rho$ at the local maximum near the $(3,-1)_\rho$ critical point is smaller for the formally singly bonded compound (Figure 2.4E). Again for Me_3NOH^+, the pnictogen-proximal minimum in $\nabla^2\rho$ is less negative than that of Me_3NO. Among the heavier pnictogens (P, As, and Sb), the oxygen-proximal minimum in $\nabla^2\rho$ is more negative for the Me_3EOH^+ compounds and in neither class of compounds is there a pnictogen-proximal minimum. The curve of ε for Me_3NOH^+ exhibits two maxima near where $\nabla^2\rho$ features local valence minima. Between these maxima, ε descends to zero near, but not coincident with, the $(3,-1)_\rho$ critical point (Figure 2.4F). The Me_3EOH^+ compounds feature heavier pnictogens lack a pnictogen-proximal maximum in ε, and the oxygen-proximal feature has a significant shoulder that extends into the vicinity of the $(3,-1)_\rho$ critical point before diminishing to zero near the pnictogen. The same results were obtained for the Ph_3EO and Ph_3EOH^+ compounds (Figure 2.4G-L). With this information in hand, we feel confident that the patterns and trends of these real-space functions (ρ, $\nabla^2\rho$, and ε) follow those established by the parent hydrides earlier in this chapter. These results indicate the reliability of DFT calculations to mirror the more computationally expensive CCSD calculations, allowing for the investigation of organic derivatives not accessible to the average user of CCSD level calculations.

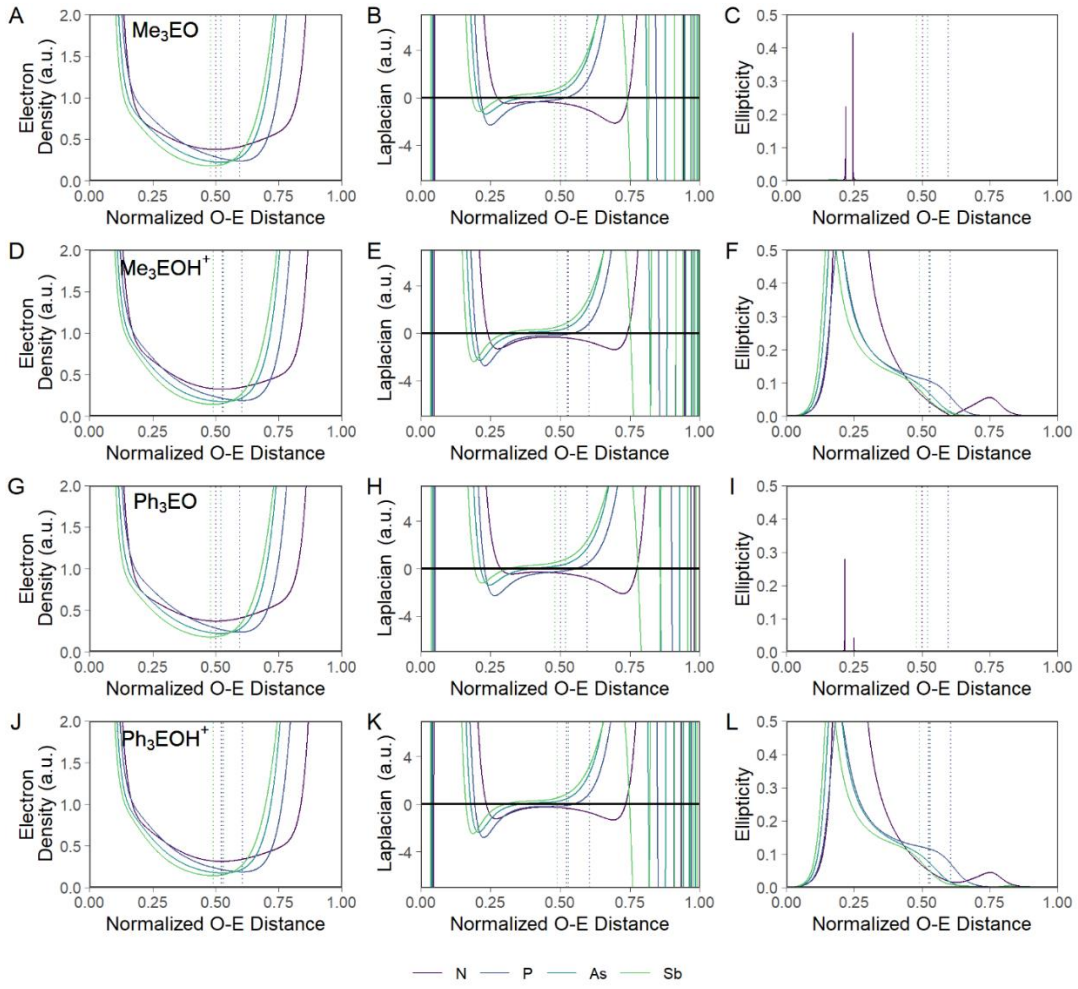

Figure 2.4. Evaluation (PBE0/old-DKH-TZVPP//PBE0/def2-TZVPP) of ρ, $\nabla^2\rho$, and ε along the normalized oxygen-pnictogen bond paths of different compounds (O at 0.0 and E at 1.0). Rows of panels feature data for a class of compounds: Me_3EO (A-C); Me_3EOH^+ (D-F); Ph_3EO (G-I); and Ph_3EOH^+ (J-L), where E is a pnictogen (N, P, As, or Sb). For (C,I), note that all compounds have ε = 0 along the length of the bond path. Dashed vertical lines represent the location of the bond critical point.

2.3 Conclusions

The bonds formed between the pnictogens and oxygen are richly varied, exhibiting a range of geometric, electronic, and reactive properties. A number of different theoretical methods can be used to provide greater insight into the nature of

the bonding interaction that exists between the pnictogen and oxygen in any given molecule and to discriminate between bond types. In this chapter, we have focused on the topological analysis of the electron density and its derivatives, which provides an orbital-agnostic means of analyzing the electronic structure using only a physical observable: the electron density. Typical analyses of this sort rely on the evaluation of real-space functions such as ρ, $\nabla^2\rho$, and ε at the $(3,-1)_\rho$ critical point between the bonded atoms to provide information on the strength and nature of the bond. When performed on the oxygen–pnictogen bonded compounds described in this chapter, such classical analysis yielded unexpected trends, particularly in $\nabla^2\rho_b$ and ε_b of the compounds containing heavier pnictogens. We have demonstrated that analysis of these functions along the entirety of the bond path resolves the apparent discrepancies. Although necessarily more information-rich, the full bond path analyses provide a set of simple patterns that are readily distinguishable to discriminate between bond types. The real-space function that perhaps performs best in this discriminatory capacity is ε. The formally O=E double-bonded species exhibit a local maximum near, but not necessarily coincident with, the $(3,-1)_\rho$ critical point. For the heavier pnictogens, O—E single bonds exhibit a characteristic shoulder on the oxygen-proximal feature of the ε curve that proves particularly capable of obfuscating ε_b trends. Finally, the compounds with triple oxygen–pnictogen bonds or the partially multiply bonded O=E/ O^{-}—E^{+} functional groups of pnictine oxides investigated here were cylindrically symmetric and consequently ε was 0 along the length of the bond path. These two classes of compounds can, however, be readily distinguished by the

behavior of $\nabla^2\rho_b$, which attains greater negative values at the oxygen-proximal local valence minimum for the triple bonds.

We originally believed these methods would be useful in better understanding the oxygen—pnictogen interactions in drugs, but they have shown a broader use in helping our group better understand the electronics and bonding involved in more fundamental pnictogen-containing compounds. Our group has used these methods to help describe and understand Sb=O double bonds[54] and current work is using these methods to develop novel bismuth-containing compounds.

2.4 Computational Methods

MP2 Geometry Optimization

All computational chemistry was performed using ORCA (version 4.2.1).[55, 56] The geometries of the 25 panel compounds depicted in Scheme 2.1 (EO^+, HEO, H_2EOH, H_3EOH^+ and H_3EO where E = N, P, As, Sb, or Bi) were optimized at the MP2/def2-QZVPP level of theory.[45] The resolution of the identity chain of spheres (RIJCOSX)[57] approximation was employed and the necessary auxiliary basis sets were generated using the AutoAux functionality.[58] Increased convergence criteria were employed during the SCF process (tightSCF) and the geometry optimization (tightOPT). The sizes of the integration grid and the COSX grid were increased (Grid7 GridX6 NOFINALGRID).

CCSD Electron Density

Using the MP2/def2-QZVPP geometries (or literature geometries extracted from the NIST Computational Chemistry Comparison and Benchmark Database for ethane, ethene, ethyne, and Ne_2),[43] wavefunctions were obtained using atomic orbital coupled-cluster singles doubles (AO-CCSD) calculations with an all-electron relativistically contracted quadruple-ζ atomic natural orbital (ANO-RCC-QZP)[46, 47] basis set. The resolution of the identity approximation was employed (RI-AO) and relativistic effects were taken into consideration using the second-order Douglas-Kroll-Hess procedure (DKH). Orbital optimization, involving evaluation of the Z vector, was employed to obtain fully relaxed CCSD electron densities.

DFT calculations

The geometries of the nitrogen, phosphorus, arsenic, and antimony compounds in Scheme 2.1 were optimized at the PBE0/def2-TZVPP level of theory,[45, 59, 60] employing the RIJCOSX approximation with the def2/J auxiliary basis set,[61] tight geometry optimization criteria (tightOPT), and expanded grids (Grid5 GridX7 NOFINALGRID). The electron density was then calculated at these optimized geometries using the hybrid PBE0 functional and an earlier version of the relativisitically contracted TZVPP basis set (old-DKH-TZVPP). The RIJCOSX approximation was employed with an appropriate segmented all-electron relativistically contracted (SARC/J)[62-65] auxiliary basis set. The second-order DKH method was used and expanded grids were employed (Grid7 GridX7

NOFINALGRID). Analogous DFT calculations were also performed on organic derivatives Me_3EO, Me_3EOH^+, Ph_3EO, and Ph_3EOH^+ where E = N, P, As, or Sb.

Topological Analysis of Electron Density

The electron densities, either DFT or orbital-optimized CCSD, were analyzed using MultiWFN (version 3.7).[66] In all instances, a (3,-1) critical point in ρ was found between the oxygen and pnictogen (or pair of carbon or pair of neon) atoms. The values of ρ, $\nabla^2\rho$, and ε were either evaluated at the $(3,-1)_\rho$ critical point or along the length of the line connecting the oxygen and pnictogen (or pair of carbon or pair of neon) atoms. The values of these real-space functions along the interatomic line were further analyzed using R (version 4.0.2) through RStudio (version 1.3.1073). The following R packages were used for analysis and visualization: tidyverse, gridExtra, ggtext, and grid.

2.5 References

1. Zhao, L.; Pan, S.; Holzmann, N.; Schwerdtfeger, P.; Frenking, G., Chemical Bonding and Bonding Models of Main-Group Compounds. *Chemical Reviews* **2019,** *119* (14), 8781-8845.
2. Bayne, J. M.; Stephan, D. W., Phosphorus Lewis acids: emerging reactivity and applications in catalysis. *Chemical Society Reviews* **2016,** *45* (4), 765-774.
3. Jones, J. S.; Gabbaï, F. P., Coordination- and Redox-Noninnocent Behavior of Ambiphilic Ligands Containing Antimony. *Accounts of Chemical Research* **2016,** *49* (5), 857-867.
4. Cummins, C. C., Phosphorus: From the Stars to Land & Sea. *Daedalus* **2014,** *143* (4), 9-20.

5. Robertson, A. P. M.; Gray, P. A.; Burford, N., Interpnictogen Cations: Exploring New Vistas in Coordination Chemistry. *Angewandte Chemie International Edition* **2014,** *53* (24), 6050-6069.

6. Moc, J.; Morokuma, K., *Ab Initio* Molecular Orbital Study on the Periodic Trends in Structures and Energies of Hypervalent Compounds: Five-Coordinated XH_5 Species Containing a Group 15 Central Atom (X = P, As, Sb, and Bi). *Journal of the American Chemical Society* **1995,** *117* (47), 11790-11797.

7. Jerzembeck, W.; Bürger, H.; Constantin, L.; Margulès, L.; Demaison, J.; Breidung, J.; Thiel, W., Bismuthine BiH_3: Fact or Fiction? High-Resolution Infrared, Millimeter-Wave, and Ab Initio Studies. *Angewandte Chemie International Edition* **2002,** *41* (14), 2550-2552.

8. Trubenstein, H. J.; Moaven, S.; Vega, M.; Unruh, D. K.; Cozzolino, A. F., Pnictogen bonding with alkoxide cages: which pnictogen is best? *New Journal of Chemistry* **2019,** *43* (36), 14305-14312.

9. Goicoechea, J. M.; Grützmacher, H., The Chemistry of the 2-Phosphaethynolate Anion. *Angewandte Chemie International Edition* **2018,** *57* (52), 16968-16994.

10. Twamley, B.; Sofield, C. D.; Olmstead, M. M.; Power, P. P., Homologous Series of Heavier Element Dipnictenes 2,6-$Ar_2H_3C_6E$=EC_6H_3-2,6-Ar_2 (E = P, As, Sb, Bi; Ar = Mes = C_6H_2-2,4,6-Me_3; or Trip = C_6H2-2,4,6-$^iPr_3$) Stabilized by *m*-Terphenyl Ligands. *Journal of the American Chemical Society* **1999,** *121* (14), 3357-3367.

11. Greenwood, N. N.; Earnshaw, A., *Chemistry of the Elements*. 2nd ed.; Butterworth-Heinemann: Oxford ; Boston, 1997; p xxii, 1341 p.

12. Voet, D.; Voet, J. G., *Biochemistry*. 4th ed.; John Wiley & Sons: Hoboken, NJ, 2011; p xxv, 1428, 53 p.

13. Gibaud, S.; Jaouen, G., Arsenic-Based Drugs: From Fowler's Solution to Modern Anticancer Chemotherapy. In *Medicinal Organometallic Chemistry*, Jaouen, G.; Metzler-Nolte, N., Eds. Springer-Verlag: Berlin, 2010; Vol. 32, pp 1-20.

14. Nagle, A. S.; Khare, S.; Kumar, A. B.; Supek, F.; Buchynskyy, A.; Mathison, C. J. N.; Chennamaneni, N. K.; Pendem, N.; Buckner, F. S.; Gelb, M. H.; Molteni, V., Recent Developments in Drug Discovery for Leishmaniasis and Human African Trypanosomiasis. *Chemical Reviews* **2014,** *114* (22), 11305-11347.

15. Andrews, P. C.; Deacon, G. B.; Forsyth, C. M.; Junk, P. C.; Kumar, I.; Maguire, M., Towards a Structural Understanding of the Anti-Ulcer and Anti-Gastritis Drug Bismuth Subsalicylate. *Angewandte Chemie International Edition* **2006,** *45* (34), 5638-5642.

16. Rogachev, A. Y.; Burger, P., Bonding situation and N–O-bond strengths in amine-*N*-oxides—a combined experimental and theoretical study. *Physical Chemistry Chemical Physics* **2012,** *14* (6), 1985–2000.

17. Łukomska, M.; Rybarczyk-Pirek, A. J.; Jabłoński, M.; Palusiak, M., The nature of NO-bonding in *N*-oxide group. *Physical Chemistry Chemical Physics* **2015,** *17* (25), 16375-16387.

18. Dobado, J. A.; Martínez-García, H.; Molina; Sundberg, M. R., Chemical Bonding in Hypervalent Molecules Revised. Application of the Atoms in Molecules Theory to Y_3X and Y_3XZ (Y = H or CH_3; X = N, P or As; Z = O or S) Compounds. *Journal of the American Chemical Society* **1998,** *120* (33), 8461-8471.

19. Chesnut, D. B.; Savin, A., The Electron Localization Function (ELF) Description of the PO Bond in Phosphine Oxide. *Journal of the American Chemical Society* **1999,** *121* (10), 2335-2336.

20. Lyssenko, K. A.; Grintselev-Knyazev, G. V.; Antipin, M. Y., Nature of the PO bond in diphenylphosphonic acid: experimental charge density and electron localization function analysis. *Mendeleev Communications* **2002,** *12* (4), 128-130.

21. Chesnut, D. B., Atoms-in-Molecules and Electron Localization Function Study of the Phosphoryl Bond. *The Journal of Physical Chemistry A* **2003,** *107* (21), 4307-4313.

22. Gamoke, B.; Neff, D.; Simons, J., Nature of PO Bonds in Phosphates. *The Journal of Physical Chemistry A* **2009,** *113* (19), 5677-5684.

23. Yamada, K.; Koga, N., Variationally determined electronic states for the theoretical analysis of intramolecular interaction. II. Qualitative nature of the P—O bond in phosphine oxides. *Journal of Computational Chemistry* **2013,** *34* (2), 149-161.

24. Viana, R. B., Tailoring the electronic properties among oxoarsine, arsinoyl and arsine oxide isomers: the simplest molecular systems with an arsenic–oxygen bond. *RSC Advances* **2016,** *6* (93), 90760-90770.

25. Yang, T.; Andrada, D. M.; Frenking, G., Dative versus electron-sharing bonding in N-oxides and phosphane oxides R_3EO and relative energies of the R_2EOR isomers (E = N, P; R = H, F, Cl, Me, Ph). A theoretical study. *Physical Chemistry Chemical Physics* **2018,** *20* (17), 11856-11866.

26. Glendening, E. D.; Landis, C. R.; Weinhold, F., NBO 7.0: New vistas in localized and delocalized chemical bonding theory. *Journal of Computational Chemistry* **2019,** *40*, 2234–2241.

27. Stowasser, R.; Hoffmann, R., What Do the Kohn−Sham Orbitals and Eigenvalues Mean? *Journal of the American Chemical Society* **1999,** *121* (14), 3414-3420.

28. Bader, R. F. W., Atoms in Molecules. *Accounts of Chemical Research* **1985,** *18* (1), 9-15.

29. Bader, R. F. W., A Quantum Theory of Molecular Structure and Its Applications. *Chemical Reviews* **1991,** *91* (5), 893-928.

30. Bader, R. F. W., A Bond Path: A Universal Indicator of Bonded Interactions. *The Journal of Physical Chemistry A* **1998,** *102* (37), 7314-7323.

31. Danovich, D.; Shaik, S.; Rzepa, H. S.; Hoffmann, R., A Response to the Critical Comments on "One Molecule, Two Atoms, Three Views, Four Bonds?". *Angewandte Chemie International Edition* **2013,** *52* (23), 5926-5928.

32. Bader, R. F. W.; Essén, H., The characterization of atomic interactions. *The Journal of Chemical Physics* **1984,** *80* (5), 1943-1960.

33. Bader, R. F. W.; Slee, T. S.; Cremer, D.; Kraka, E., Description of Conjugation and Hyperconjugation in Terms of Electron Distributions. *Journal of the American Chemical Society* **1983,** *105* (15), 5061-5068.

34. Cremer, D.; Kraka, E.; Slee, T. S.; Bader, R. F. W.; Lau, C. D. H.; Nguyen Dang, T. T.; MacDougall, P. J., Description of homoaromaticity in terms of electron distributions. *Journal of the American Chemical Society* **1983,** *105* (15), 5069-5075.

35. Cheeseman, J. R.; Carroll, M. T.; Bader, R. F. W., The mechanics of hydrogen bond formation in conjugated systems. *Chemical Physics Letters* **1988,** *143* (5), 450-458.

36. Scherer, W.; Sirsch, P.; Grosche, M.; Spiegler, M.; Mason, S. A.; Gardiner, M. G., Agostic deformations based on electron delocalization in the alkyllithium-

complex [{2-($Me_3Si)_2CLiC_5H_4N$ }$_2$. *Chemical Communications* **2001,** (20), 2072-2073.

37. Scherer, W.; Sirsch, P.; Shorokhov, D.; McGrady, G. S.; Mason, S. A.; Gardiner, M. G., Valence-Shell Charge Concentrations and Electron Delocalization in Alkyllithium Complexes: Negative Hyperconjugation and Agostic Bonding. *Chemistry - A European Journal* **2002,** *8* (10), 2324-2334.

38. Tafipolsky, M.; Scherer, W.; Öfele, K.; Artus, G.; Pedersen, B.; Herrmann, W. A.; McGrady, G. S., Electron Delocalization in Acyclic andN-Heterocyclic Carbenes and Their Complexes: A Combined Experimental and Theoretical Charge-Density Study. *Journal of the American Chemical Society* **2002,** *124* (20), 5865-5880.

39. Ott, H.; Däschlein, C.; Leusser, D.; Schildbach, D.; Seibel, T.; Stalke, D.; Strohmann, C., Structure/Reactivity Studies on an α-Lithiated Benzylsilane: Chemical Interpretation of Experimental Charge Density. *Journal of the American Chemical Society* **2008,** *130* (36), 11901-11911.

40. Farrugia, L. J.; Khalaji, A. D., Evidence for Side-Chain π-Delocalization in a Planar Substituted Benzene: An Experimental and Theoretical Charge Density Study on 2,5-Dimethoxybenzaldehyde Thiosemicarbazone. *The Journal of Physical Chemistry A* **2011,** *115* (45), 12512-12522.

41. Huang, W. J.; Momen, R.; Azizi, A.; Xu, T.; Kirk, S. R.; Filatov, M.; Jenkins, S., Next-generation quantum theory of atoms in molecules for the ground and excited states of fulvene. *International Journal of Quantum Chemistry* **2018,** *118* (22), e25768.

42. Espinosa Ferao, A.; García Alcaraz, A.; Zaragoza Noguera, S.; Streubel, R., Terminal Phosphinidene Complex Adducts with Neutral and Anionic O-Donors and Halides and the Search for a Differentiating Bonding Descriptor. *Inorganic Chemistry* **2020,** *59* (17), 12829-12841.

43. NIST, NIST Computational Chemistry Comparison and Benchmark Database; NIST Standard Reference Database Number 101, Realease 21 (August 2020).

44. Ulrich, B.; Vredenborg, A.; Malakzadeh, A.; Schmidt, L. P. H.; Havermeier, T.; Meckel, M.; Cole, K.; Smolarski, M.; Chang, Z.; Jahnke, T.; Dörner, R., Imaging of the Structure of the Argon and Neon Dimer, Trimer, and Tetramer. *The Journal of Physical Chemistry A* **2011,** *115* (25), 6936-6941.

45. Weigend, F.; Ahlrichs, R., Balanced basis sets of split valence, triple zeta valence and quadruple zeta valence quality for H to Rn: Design and assessment of accuracy. *Physical Chemistry Chemical Physics* **2005,** *7* (18), 3297-3305.

46. Widmark, P.-O.; Malmqvist, P.-Å.; Roos, B. O., Density matrix averaged atomic natural orbital (ANO) basis sets for correlated molecular wave functions. *Theoretica Chimica Acta* **1990,** *77* (5), 291-306.

47. Roos, B. O.; Lindh, R.; Malmqvist, P.-Å.; Veryazov, V.; Widmark, P.-O., Main Group Atoms and Dimers Studied with a New Relativistic ANO Basis Set. *The Journal of Physical Chemistry A* **2004,** *108* (15), 2851-2858.

48. Medvedev, M. G.; Bushmarinov, I. S.; Sun, J.; Perdew, J. P.; Lyssenko, K. A., Density functional theory is straying from the path toward the exact functional. *Science* **2017,** *355* (6320), 49-52.

49. Kepp, K. P., Comment on "Density functional theory is straying from the path toward the exact functional". *Science* **2017,** *356* (6337), 496b.

50. Brorsen, K. R.; Yang, Y.; Pak, M. V.; Hammes-Schiffer, S., Is the Accuracy of Density Functional Theory for Atomization Energies and Densities in Bonding Regions Correlated? *The Journal of Physical Chemistry Letters* **2017,** *8* (9), 2076-2081.

51. Medvedev, M. G.; Bushmarinov, I. S.; Sun, J.; Perdew, J. P.; Lyssenko, K. A., Response to Comment on "Density functional theory is straying from the path toward the exact functional". *Science* **2017,** *356* (6337), 496c.

52. Ranasinghe, D. S.; Perera, A.; Bartlett, R. J., A note on the accuracy of KS-DFT densities. *The Journal of Chemical Physics* **2017,** *147* (20), 204103.

53. Mayer, I.; Pápai, I.; Bakó, I.; Nagy, Á., Conceptual Problem with Calculating Electron Densities in Finite Basis Density Functional Theory. *Journal of Chemical Theory and Computation* **2017,** *13* (9), 3961-3963.

54. Wenger, J. S.; Weng, M.; George, G. N.; Johnstone, T. C., Isolation, bonding and reactivity of a monomeric stibine oxide. *Nature Chemistry* **2023,** *15* (5), 633-640.

55. Neese, F., The ORCA program system. *WIREs Computational Molecular Science* **2011,** *2* (1), 73-78.

56. Neese, F., Software update: the ORCA program system, version 4.0. *WIREs Computational Molecular Science* **2018,** *8* (1), e1327.

57. Kossmann, S.; Neese, F., Efficient Structure Optimization with Second-Order Many-Body Perturbation Theory: The RIJCOSX-MP2 Method. *Journal of Chemical Theory and Computation* **2010,** *6* (8), 2325-2338.

58. Stoychev, G. L.; Auer, A. A.; Neese, F., Automatic Generation of Auxiliary Basis Sets. *Journal of Chemical Theory and Computation* **2017,** *13* (2), 554-562.

59. Perdew, J. P.; Ernzerhof, M.; Burke, K., Rationale for mixing exact exchange with density functional approximations. *The Journal of Chemical Physics* **1996,** *105* (22), 9982-9985.

60. Perdew, J. P.; Burke, K.; Ernzerhof, M., Generalized Gradient Approximation Made Simple. *Physical Review Letters* **1996,** *77* (18), 3865-3868.

61. Weigend, F., Accurate Coulomb-fitting basis sets for H to Rn. *Physical Chemistry Chemical Physics* **2006,** *8* (9), 1057-1065.

62. Pantazis, D. A.; Chen, X.-Y.; Landis, C. R.; Neese, F., All-Electron Scalar Relativistic Basis Sets for Third-Row Transition Metal Atoms. *J. Chem. Theory Comput.* **2008,** *4* (6), 908-919.

63. Pantazis, D. A.; Neese, F., All-Electron Scalar Relativistic Basis Sets for the Lanthanides. *Journal of Chemical Theory and Computation* **2009,** *5* (9), 2229-2238.

64. Pantazis, D. A.; Neese, F., All-Electron Scalar Relativistic Basis Sets for the Actinides. *Journal of Chemical Theory and Computation* **2011,** *7* (3), 677-684.

65. Pantazis, D. A.; Neese, F., All-electron scalar relativistic basis sets for the 6p elements. *Theoretical Chemistry Accounts* **2012,** *131* (11), 1292.

66. Lu, T.; Chen, F., Multiwfn: A multifunctional wavefunction analyzer. *Journal of Computational Chemistry* **2012,** *33* (5), 580-592.

Chapter 3

Synthesis and Structural Characterization of Pentaphenylantimony

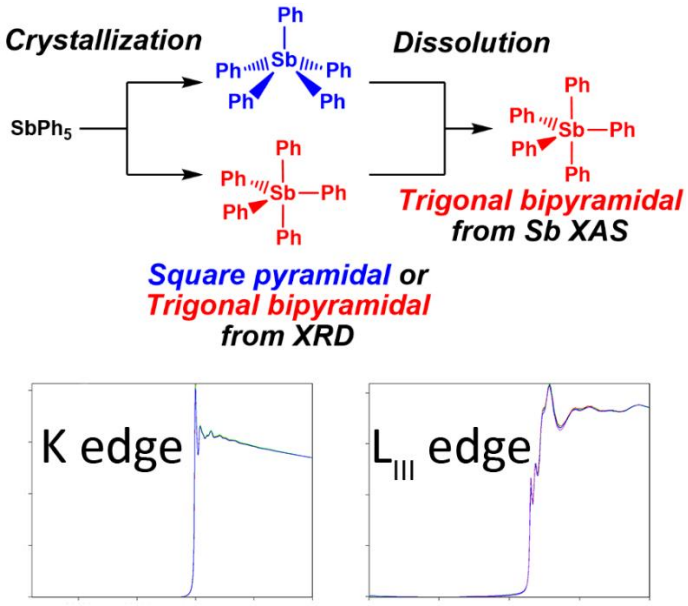

Published in part in: Lindquist-Kleissler, B.; Johnstone, T. C. *Inorg. Chem.* **2021,** *60,* 8566.

3.1 Introduction

In an effort to begin our understanding of the structures of the pentavalent antimonials, we wanted to test our use of physical inorganic techniques using a model compound. For this purpose, we chose pentaphenylantimony because it crystallizes in two different geometries. If we can differentiate between the two geometries using these physical inorganic techniques, then these techniques might be useful in elucidating the structures of the pentavalent antimonials. Pentaphenylantimony (pentaphenylstiborane, pentaphenyl-λ^5-stibane, $SbPh_5$) was the first pentasubstituted pentavalent (σ^5,λ^5) main-group compound to be crystallographically characterized.[1-3] Due to valence-shell electron pair repulsion (VSEPR) theory, it was expected that the crystal structure of $SbPh_5$ would provide unambiguous confirmation of its trigonal bipyramidal structure. Prior to crystallographically characterizing $SbPh_5$, it was further confirmed that this molecule was trigonal bipyramidal based on spectroscopic measurements on a variety of other σ^5,λ^5 pnictogen compounds.[4-8] However, $SbPh_5$ was found to adopt a distorted square pyramidal structure in the solid state.[9-11] The τ parameter reflects the extent of distortion from a trigonal bipyramidal geometry, by capturing the position along the C_{2v}-symmetric normal coordinate that connects the C_{4v} square pyramidal ($\tau = 0$) and D_{3h} trigonal bipyramidal ($\tau = 1$) geometries.[12] The first published structure of $SbPh_5$ featured a τ of 0.267 (Figure 3.1a).[10] Although this τ value reflects a distorted square pyramidal geometry, we will refer to this geometry as *square pyramidal* for the sake of consistency with past literature.[9, 10] Rationalization of this unexpected structure was hampered by the fact that the subsequently

determined crystal structure of the cyclohexane hemisolvate of $SbPh_5$ ($SbPh_5 \cdot 0.5C_6H_{12}$) featured the $SbPh_5$ molecule in a trigonal bipyramidal geometry with a τ of 0.952 (Figure 3.1b).[13] A series of studies suggested that both the crystals of $SbPh_5$ and $SbPh_5 \cdot 0.5C_6H_{12}$ had significant packing forces influencing their structures,[14-19] but it remained unclear which of the two geometries was more stable in the absence of crystal packing forces (i.e., in solution or gas phase).

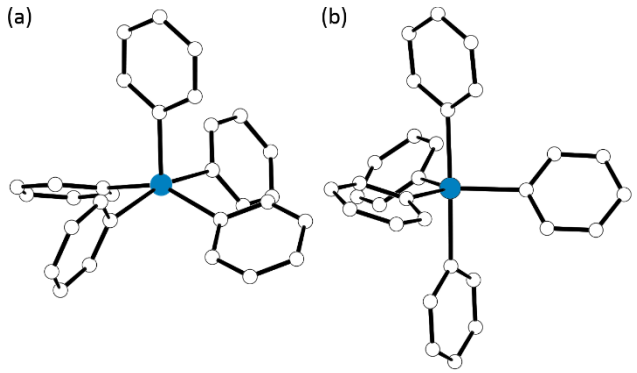

Figure 3.1. Ball-and-stick representations of the (a) square pyramidal and (b) trigonal bipyramidal structures of $SbPh_5$ previously reported for the nonsolvate and cyclohexane hemisolvate, respectively (refs 10 and 13). H atoms omitted for clarity; Sb colored blue.

The robustness, utility, and simplicity of VSEPR theory have all contributed to its long persistent use and reference in the chemical literature.[4, 8, 20, 21] Due to the relatively simple nature of VSEPR theory, there are instances in which the VSEPR-predicted geometry is not the one observed. We are not alone in our ideology in believing that these "failures" do not indicate that the theory should be discarded[22] but rather highlight interesting molecules with electronic structures more complex than can be accounted for by the simplicity of VSEPR theory. An interesting example

of this is WMe_6, which assumes a trigonal prismatic geometry instead of the VSEPR-predicted octahedral geometry.[23-27] Studies focusing on WMe_6 and other non-octahedral six-coordinate compounds ultimately led to a deeper understanding of bonding and electronic structure.[28, 29] As stated previously, for pentasubstituted species with no stereochemically active lone pairs, such as σ^5,λ^5 pnictogen compounds, VSEPR theory predicts the trigonal bipyramidal geometry to be the most stable. Many spectroscopic studies confirm this geometrical preference, however, these experiments also reveal these species to be highly fluxional.[6, 7] NMR spectra, primarily ^{1}H NMR, of $SbPh_5$ exhibit only one set of aryl resonances, even at —142 °C.[30] In order to get a clearer understanding of the solution-phase dynamics of these species, Sb(*p*-tol)$_5$, which crystallizes in a trigonal bipyramidal geometry,[31] was investigated with hopes that the methyl resonances would facilitate this understanding by supplying us with an easily-identifiable NMR shift. Unfortunately, as with $SbPh_5$, decoalescence of the signals could not be achieved, even at temperatures as low as —130 °C.[32] Broadening of the methyl ^{1}H NMR resonances at low temperature was analyzed to obtain an estimate of the barrier to fluxional motion of 1.60 kcal mol^{-1}; analysis of the broadening of the ^{13}C{^{1}H} aryl resonances afforded an estimated activation energy of 1.46 kcal mol^{-1}.

There are many types of intramolecular rearrangements, also known as polytopal rearrangements. One of the more common mechanisms for fluxionality in σ^5,λ^5 pnictogen compounds is the Berry pseudorotation, whereby the axial and equatorial substituents of a trigonal bipyramid (D_{3h}) exchange via a square pyramidal

(C_{4v}) intermediate or transition state.[33] The Berry pseudorotation mechanism can also exchange the basal and apical substituents of a square pyramid via a trigonal bipyramidal intermediate or transition state. Despite the preference for a trigonal bipyramidal geometry, the fluxionality of these molecules suggests that the potential energy surfaces of such species are quite shallow. Regardless of these features, the potential energy surfaces of these compounds should still feature distinct minima. In the EPh_5 series (E = P, As, Sb, Bi), PPh_5 and $AsPh_5$ have only been crystallized in trigonal bipyramidal geometries, whether as solvates or nonsolvates.[34, 35] As stated above, this geometry is the expected geometry from VSEPR theory, but NMR spectra reveal that compounds like $SbPh_5$ are highly fluxional and show only one set of phenyl resonances under all investigated temperatures. Vibrational spectroscopy, which operates on a faster time scale than NMR spectroscopy, can resolve rapidly interconverting species and indicates that $AsPh_5$ maintains its equilibrium trigonal bipyramidal geometry in solution.[36] Interestingly, $BiPh_5$ has been shown to assume a square pyramidal geometry in the solid state, and electronic absorption spectroscopic measurements have been interpreted as confirming the persistence of this geometry in solution.[37] Subsequent studies of $BiPh_5$ have drawn on relativistic effects to explain the stabilization of this non-VSEPR geometry.[37-40] It appears that $SbPh_5$ is somewhat unique, and lies at a cusp of a transition where the factors that favor trigonal bipyramidal for PPh_5 and $AsPh_5$, are overtaken by those that favor a square pyramidal geometry for $BiPh_5$. These factors seem to be of similar, if not the same, importance in $SbPh_5$, given that both geometries are readily accessible in the solid state.

To further emphasize the uniqueness of $SbPh_5$, all other pentaarylantimony(V) compounds for which crystallographic data have been obtained, or for which a structure has been determined in solution, have exhibited a trigonal bipyramidal geometry. Of these examples, $Sb(C_6F_5)_5$ is trigonal bipyramidal in the crystalline state, and decoalescence in the ^{19}F NMR spectrum is observed at —55 °C.[41] As expected for a trigonal bipyramidal geometry, the low temperature spectra featured signals in a 2:3 ratio. The parameters from the low-temperature data were used to model high-temperature spectra which indicate that the trigonal bipyramidal geometry persists at higher temperatures.[41] Another set of examples that illustrate the behavior of these species was the systematic investigation of all combinations of $Sb(p\text{-tol})_x(p\text{-}CF_3C_6H_4)_{5-x}$ for x = 0—5.[42] All compounds in that study were trigonal bipyramidal in the crystalline state and showed no decoalescence down to temperatures of —80 °C. With this information, it would be tempting to conclude that $SbPh_5$ is trigonal bipyramidal in solution and is only perturbed from this equilibrium trigonal bipyramidal geometry to a distorted square pyramidal geometry in the crystalline state. However, the only previous report to reach a conclusion on the solution-state structure of $SbPh_5$ concluded that it was square pyramidal from vibrational spectroscopy.[36] The question of why this particular stiborane would favor a square pyramidal geometry remains unanswered.

In this study, we present new X-ray absorption spectroscopic (XAS) and revised Raman spectroscopic data collected on crystals that feature $SbPh_5$ in either a square pyramidal or trigonal bipyramidal geometry. When compared to the spectra of

$SbPh_5$ in solution, these data support the proposal that the molecule assumes the VSEPR-predicted trigonal bipyramidal geometry in solution. Not only do these data help conclude a historically important investigation into the structure of $SbPh_5$, but arguably more important, they highlight the ability of XAS to provide detailed information about the structures of fluxional Sb compounds. We acknowledge that our conclusion contradicts that reached by previous investigators, and we provide a suggestion for the origin of this contradiction.

3.2 Results and Discussion

As noted above, $SbPh_5$ has been crystallized in both a square pyramidal (nonsolvate) and a trigonal bipyramidal (solvates) geometry, but which of the two is the most stable in solution or in the gas phase, in the absence of crystal packing forces? Ideally this question can be answered spectroscopically, however, common spectroscopic techniques like NMR spectroscopy are hampered by the fluxionality of the molecule on the time scale of this technique (millisecond to microsecond). Vibrational spectroscopy provides access to a faster time scale (picosecond) which could allow one to look past the fluxionality of the molecule and "freeze" out individual geometries. Previous studies comparing IR and Raman spectra of solutions of $SbPh_5$ with solid-state spectra of the square pyramidal $SbPh_5$ nonsolvate suggested that the square pyramidal geometry is preserved in solution.[36]

The overarching theme of this thesis is the chemistry of the group 15 elements, primarily focusing on antimony (Sb).[43, 44] It is this interest that prompted

our investigation of the utility of spectroscopic techniques that can provide insight into the geometry about Sb centers. Of particular interest is XAS because it provides an opportunity to directly probe the Sb center. In the case of $SbPh_5$, both geometries (square pyramidal and trigonal bipyramidal) feature Sb in the +5 oxidation state, meaning the edge energies will provide little discriminatory power. The extended X-ray absorption fine structure (EXAFS) region would likely be similarly devoid of information since there is no change in coordination number or ligating atoms, as well as little change in the Sb—C bond lengths. This leaves us with the X-ray absorption near-edge spectroscopy (XANES) region to differentiate between the two geometries. The symmetry of the two geometries is quite distinct, approximately D_{3h} for the trigonal bipyramidal geometry and approximately C_{4v} for the square pyramidal geometry. We suspected that the pre-edge features in the XANES region, which are governed by the typical electronic absorption spectroscopy selection rules and can resolve species that are dynamically interconverting with very short (femtosecond) lifetimes, would provide the discriminatory power we desired. We aimed to obtain Sb X-ray absorption spectra of both crystalline solids (solvate and nonsolvate) for which the geometry of $SbPh_5$ is known and compare them to the spectra of $SbPh_5$ in solution. With these solids in hand, we also decided to revisit the earlier Raman spectra collected from $SbPh_5$.

Synthesis and Crystallography

Modifying a previously established procedure,[45] crude $SbPh_5$ was isolated from the reaction of *trans*-$SbBr_2Ph_3$ with 2 equiv of PhMgBr (Scheme 3.1). In the

original report of the crystal structure of $SbPh_5$, crystals were grown from isooctane.[10] We found that either *n*-pentane or a 1:1 Et_2O/*n*-pentane mixture serves equally well and that cooling concentrated solutions of $SbPh_5$ to —20 °C reliably affords crystalline material with analytical data that match those previously reported for $SbPh_5$.

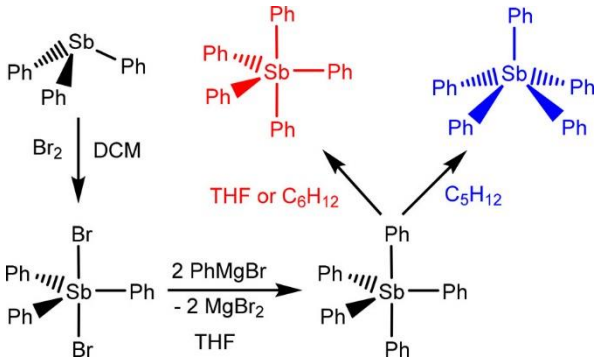

Scheme 3.1. Synthesis of $SbPh_5$ and solvents used to isolate crystals featuring different molecular geometries.

We confirmed that our material crystallized from *n*-pentane is structurally identical to that previously crystallized from isooctane (Figure 3.2a)[10] via single-crystal X-ray diffraction (Table B.1). Our low-temperature, high-resolution structure affords a $\tau = 0.216$ for the distorted square pyramidal compound (nonsolvate). The apical Sb—C bond length is 2.129(2) Å, which is slightly, but statistically significantly, shorter than the basal Sb—C bond lengths, which range from 2.208(2) to 2.213(2) Å.

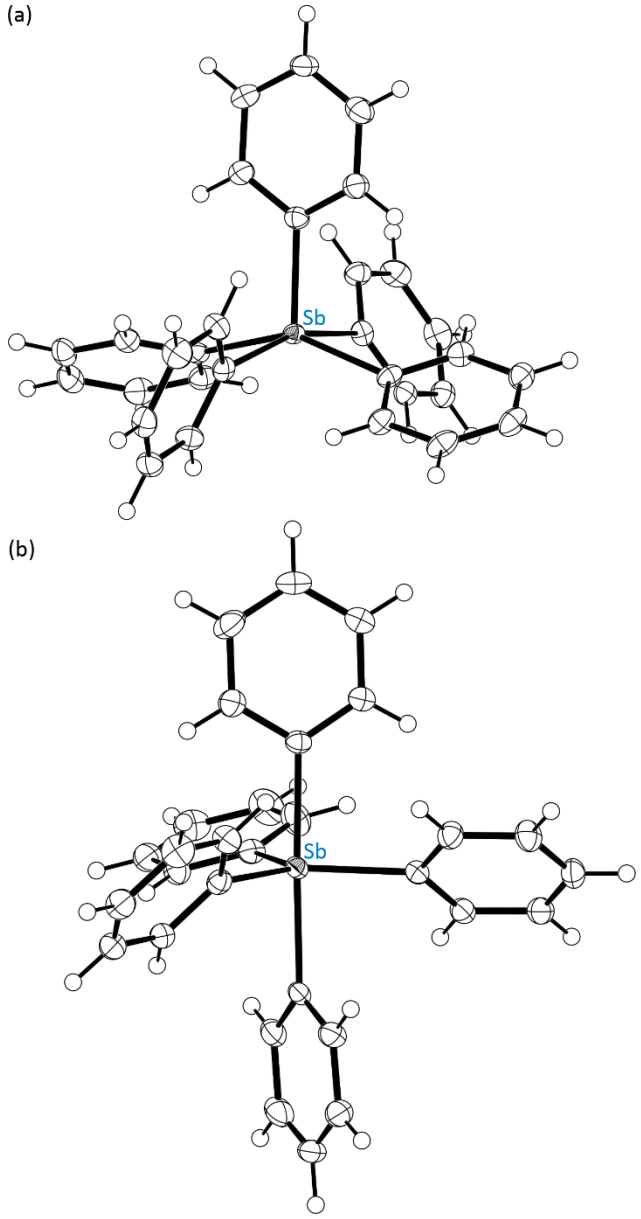

Figure 3.2. Crystallographically determined molecular structures of $SbPh_5$ from (a) $SbPh_5$ nonsolvate and (b) $SbPh_5 \cdot 0.5C_6H_{12}$. Thermal ellipsoids are drawn at 50% probability level, and H atoms are shown as spheres of arbitrary radius.

As previously reported, $SbPh_5$ can also be recrystallized from cyclohexane to yield the hemisolvate $SbPh_5 \cdot 0.5C_6H_{12}$.[13] We routinely achieve high recovery of the hemisolvate by cooling a concentrated solution of $SbPh_5$ in ~3:1 Et_2O/cyclohexane to

—20 °C (Scheme 3.1). Upon dissolution of the cyclohexane hemisolvate, NMR spectra show signals identical to those from $SbPh_5$ (nonsolvate) but with additional resonances that integrate to half an equivalent of C_6H_{12}. Single-crystal X-ray diffraction affords a structure identical to that previously reported (Figure 3.2b)[13] but with the advantage of smaller uncertainties and with the previously unmodeled solvent molecule included in the refinement. The centrosymmetric cyclohexane molecule resides on a crystallographic inversion center and is well-ordered. The $SbPh_5$ molecules assume a trigonal bipyramidal geometry in the cyclohexane hemisolvate crystals and exhibit a $\tau = 0.949$. The axial Sb—C bond lengths are 2.234(2) and 2.241(2) Å, whereas the equatorial Sb—C bond lengths range from 2.147(2) to 2.157(2) Å. The statistically significant elongation of the axial Sb—C bond lengths is consistent with the three-center-four-electron bonding expected in this compound.

We were also able to isolate crystals of the THF hemisolvate of $SbPh_5$ ($SbPh_5 \cdot 0.5C_4H_8O$) by cooling a ~4:1 *n*-pentane/THF solution of $SbPh_5$ to —20 °C. The identity and purity of this new hemisolvate were confirmed by ^1H and $^{13}C\{^1H\}$ NMR spectroscopy, single-crystal X-ray diffraction, and combustion microanalysis. The crystal structures of both the cyclohexane hemisolvate and the THF hemisolvate are isostructural, with no noteworthy differences in the $SbPh_5$ bond metrics (Table B.1). In the crystals of the THF hemisolvate, the THF molecules also reside on crystallographic inversion centers, but because THF is not centrosymmetric (unlike cyclohexane), they are disordered about these special positions.

X-ray Absorption Spectroscopy

To begin elucidating the structure of $SbPh_5$ in solution, we collected Sb XAS data on the three solids described above. The two hemisolvates served as authentic examples of trigonal bipyramidal $SbPh_5$, while the nonsolvate provided an example of square pyramidal $SbPh_5$. We first investigated the Sb K-edge spectra of crystalline $SbPh_5$, $SbPh_5 \cdot 0.5C_6H_{12}$, and $SbPh_5 \cdot 0.5C_4H_8O$ (Figure 3.3). All three samples showed a strong absorption of the hard X-rays and there are no significant pre-edge features. However, close analysis of the spectra revealed that the intensity of the white line (principal maximum) of the square pyramidal nonsolvate $SbPh_5$ was slightly lower than those of the two hemisolvates. Upon running time-dependent density functional theory (TDDFT) calculations probing excitation of the Sb 1s electrons (the electrons excited during K-edge experiments) into available valence orbitals, the results indicated that the white line bears a contribution from a metal-to-ligand charge transfer transition that is slightly more allowed in the trigonal bipyramidal geometry ($f_{osc} = 2.84 \times 10^{-4}$) than in the square pyramidal geometry ($f_{osc} = 2.56 \times 10^{-4}$) (Table B.2).

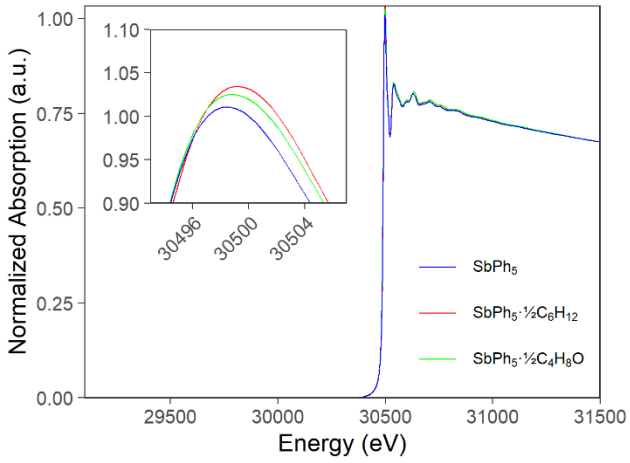

Figure 3.3. Sb K-edge absorption spectra of crystalline antimony compounds: $SbPh_5$ nonsolvate, $SbPh_5 \cdot 0.5C_6H_{12}$, and $SbPh_5 \cdot 0.5C_4H_8O$. Inset is an expansion of the white line maximum.

Although the K-edge spectra were informative, we decided to investigate the L-edge spectra, as they are frequently more information-rich and sensitive to changes in structure and bonding. Before collecting L-edge data, we decided to run more TDDFT calculations to provide some insight for the types of differences we might encounter in the spectra. We performed TDDFT calculations of the Sb L_{III}-edge for both the square pyramidal and trigonal bipyramidal geometries which revealed many closely spaced transitions from the Sb 2p orbitals to low-lying vacant molecular orbitals. These transitions cluster into two XANES pre-edge features (Figure 3.4b). Our calculations predicted that, by normalizing the data to the second pre-edge feature, the trigonal bipyramidal geometry will produce a first pre-edge feature more intense than that produced by the square pyramidal geometry. With this information in hand, we proceeded to collect spectra of the Sb L_{III}-edge for the three crystalline solids, which confirmed what we saw in our TDDFT calculations. There are two pre-

edge features, and the lower-energy feature is more intense for the two trigonal bipyramidal molecules, $SbPh_5 \cdot 0.5C_6H_{12}$, and $SbPh_5 \cdot 0.5C_4H_8O$., than the square pyramidal nonsolvate (Figure 3.4a).

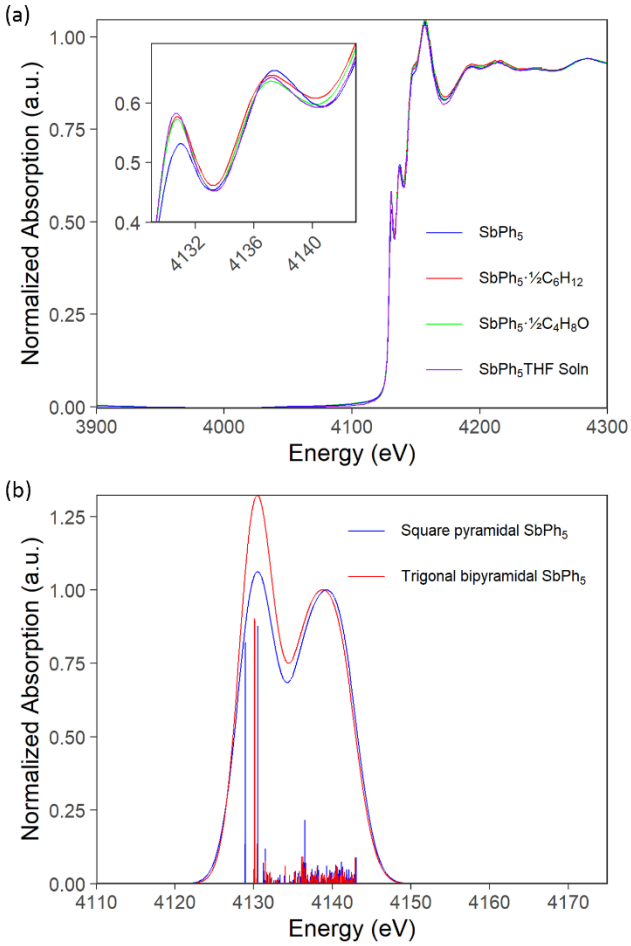

Figure 3.4. (a) Room temperature Sb L_{III}-edge absorption spectra of crystalline antimony compounds: $SbPh_5$ nonsolvate, $SbPh_5 \cdot 0.5C_6H_{12}$, and $SbPh_5 \cdot 0.5C_4H_8O$, as well as $SbPh_5$ in THF solution. Inset is an expansion of the pre-edge features. (b) Simulation of XANES Sb L_{III} pre-edge features using TDDFT (DKH2- ωB97X-D3BJ/old-DKH-TZVP(-f)). Individual transitions are shown as sticks. Calculated energies are shifted to align the first pre-edge feature to the experimentally measured energy.

The final step in our XAS experiments was to collect an Sb L_{III}-edge spectrum of a THF solution of the nonsolvate $SbPh_5$, to see which of the solid-state spectra it would agree with. The fluorescence-mode Sb L_{III}-edge spectrum of a THF solution of $SbPh_5$ overlaps nearly perfectly with the spectra of the two hemisolvate solids, in which the $SbPh_5$ molecule assumes a trigonal bipyramidal geometry (Figure 3.4a). The intensity ratio of the two pre-edge features is clearly distinct from that of the square pyramidal nonsolvate. An Sb K-edge spectrum of the $SbPh_5$ THF solution was also collected, which when compared to the K-edge spectra of the solids, showed a close match to the two spectra collected on the solid hemisolvates. We note this difference is subtle compared to the differences observed in the Sb L_{III}-edge spectra. We also note that, although the EXAFS oscillations could in principle provide information about the structure of $SbPh_5$ in solution, the extent of our data in *k*-space (up to 16 $Å^{-1}$) gives a bond-length resolution ($\sim\pi/2k$) of about 0.1 Å, which does not permit reliable distinction of the small differences in Sb—C distances between the two geometries.

These XAS data provide a compelling argument in favor of a trigonal bipyramidal geometry for $SbPh_5$ in solution. We acknowledge that this conclusion contradicts that supported by earlier vibration spectroscopic data,[36] which prompted us to repeat these Raman spectroscopic experiments.

Raman Spectroscopy

We decided to collect Raman spectra in a similar fashion to our XAS experiments discussed above. Raman spectra of the three crystalline solids ($SbPh_5$ nonsolvate, the C_6H_{12} hemisolvate, and the THF hemisolvate) were broadly similar apart from the vibrations from the solvate molecules (Figure 3.5). We did notice however, that there are noticeable differences in the bands near 650 cm^{-1} (Figure 3.5). Following the notation developed by Whiffen to categorize the vibrations of the monosubstituted phenyl rings, the bands near 650 cm^{-1} arise from *r*-mode vibrations, A_1-symmetric (with respect to an individual ring) vibrations that are X-sensitive, i.e., sensitive to the mass of the substituent on the phenyl ring.[46] Our assignment of these bands to *r*-mode vibrations agrees with prior vibrational assignments of $SbPh_5$ based on both IR and Raman data.[36, 47] The X-sensitivity of these bands suggests that the different geometries might afford bands with characteristic intensities and energies.

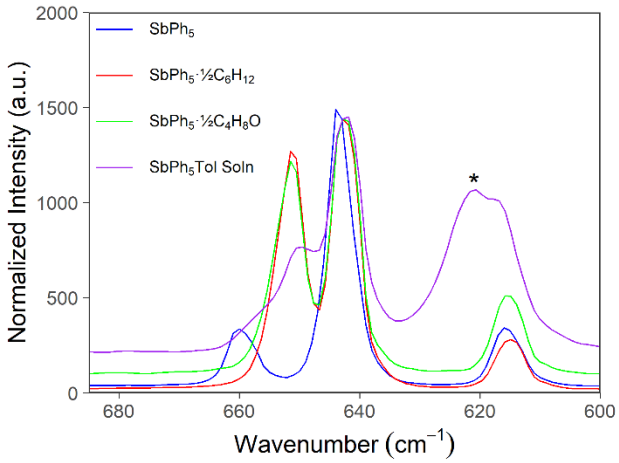

Figure 3.5. Raman spectra of crystalline antimony compounds: $SbPh_5$ nonsolvate, $SbPh_5 \cdot 0.5C_6H_{12}$, and $SbPh_5 \cdot 0.5C_4H_8O$, as well as $SbPh_5$ in a toluene solution. Spectra are expanded to the area of interest. The asterisk denotes a toluene signal from the solvent.

The Raman spectra of the two hemisolvates display two moderately intense bands centered at 642 and 650 cm^{-1}, separated by 8 cm^{-1} (Figure 3.5). The spectrum of the nonsolvate displays a moderately strong band at 643 cm^{-1} and a weaker signal centered at 660 cm^{-1}, separated by 17 cm^{-1}. Upon dissolving the nonsolvate $SbPh_5$ in toluene (THF proved too volatile for accurate data collection), the high-energy band lowers to 650 cm^{-1}, recovering the positions and 8 cm^{-1} separation present in the two hemisolvate spectra. As with the XAS experiments, the solution-state spectrum of the nonsolvate better agreed with the spectra collected from the hemisolvates featuring the trigonal bipyramidal $SbPh_5$. This agreement suggests that $SbPh_5$ assumes a trigonal bipyramidal geometry in solution.

As noted before, our conclusion differs from that reached during an earlier comparison of solid- and solution-state Raman spectra of $SbPh_5$, in which the

similarity between the spectra of the two different phases was taken as indication that the geometry assumed by $SbPh_5$ in the nonsolvate persisted in solution. In the original report, the solid-state spectrum was presumed to have been acquired on a material in which the $SbPh_5$ was square pyramidal, this will be discussed in more detail below. Upon further inspection of the previously reported spectra (Figures 1 and 2 in ref 36), we determined that they better agree with the data obtained from our hemisolvates than the nonsolvate: two moderately strong bands separated by 8 cm^{-1} are present at 646 and 654 cm^{-1}.

To further bolster our conclusions from the XAS and Raman data, a relaxed surface scan along the Berry pseudorotation coordinate from $\tau = 1$ (trigonal bipyramidal) to $\tau = 0$ (square pyramidal) was performed at the BP86-D3/def2-SVP level of theory (Figure 3.6). The scan revealed that the potential energy surface is quite shallow, which is consistent with both the fluxional behavior of this compound in solution and with $SbPh_5$'s ability to readily distort into a square pyramidal geometry under the influence of minor forces, such as crystal packing forces. Despite the shallow nature of this potential energy surface, it clearly shows that the lowest-energy geometry is indeed approximately trigonal bipyramidal.

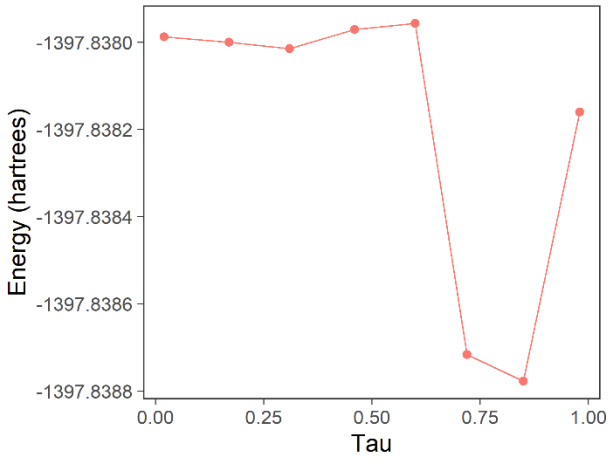

Figure 3.6. Relaxed surface scan (BP86-D3/def2-SVP) of $SbPh_5$ along the Berry pseudorotation internal coordinate.

Color of $SbPh_5$

In closing, as mentioned above, we sought to explain the discrepancy between our Raman spectroscopic data and those reported previously by calling attention to a curious observation we made during the course of this work: *the nonsolvate crystals of $SbPh_5$, in which the molecule assumes a square pyramidal geometry, are yellow*. In contrast, the two crystalline hemisolvate solids, in which $SbPh_5$ is trigonal bipyramidal, are both colorless (Figure 3.7a). Due to our scrupulous confirmation of the purity of the yellow crystals via NMR spectroscopy and combustion microanalysis, we conclude that the yellow color arises from the $SbPh_5$ and not an impurity. Under a microscope, the yellow color of a single crystal is extinguished as the crystal is rotated during illumination with plane-polarized light (Figure B.6). Further TDDFT calculations indicate that in square pyramidal $SbPh_5$, a low-energy

transition that is forbidden in the trigonal bipyramidal geometry gains intensity (Figure B.7). This transition extends into the visible region, and we propose, gives rise to the yellow color of the crystals. Upon dissolution of the yellow crystals in $CHCl_3$, CH_2Cl_2, CH_3CN, *n*-pentane, *n*-hexane, cyclohexane, THF, Et_2O, or toluene the yellow color is immediately discharged, further supporting our conclusion that $SbPh_5$ assumes a trigonal bipyramidal geometry in solution. This is further corroborated by the electronic absorption spectra of the three crystalline solids dissolved in *n*-pentane. Spectra of the three *n*-pentane solutions are identical and feature no visible absorption (Figure 3.7b). The same is observed with THF or cyclohexane solutions. We attempted to further investigate the source of the yellow color by collecting solid-state single-crystal UV-vis spectra on the three solids, however the crystals absorbed too strongly, and we could not grow thin enough crystals to collect interpretable spectra.

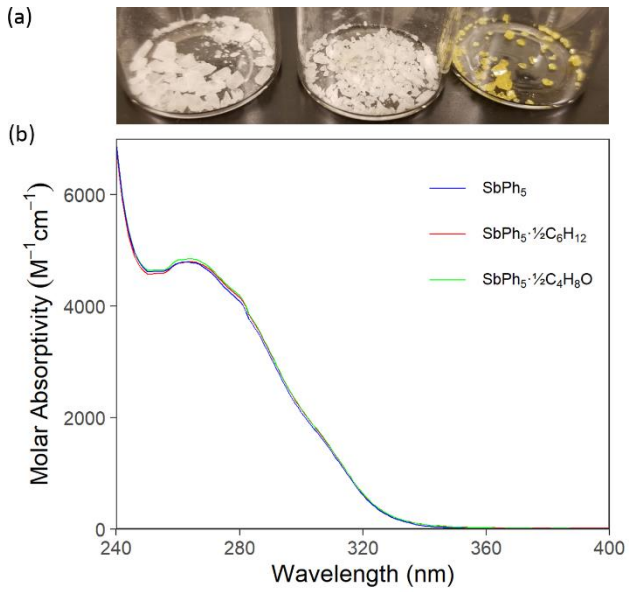

Figure 3.7. (a) Photograph of $SbPh_5 \cdot 0.5C_6H_{12}$ (left), $SbPh_5 \cdot 0.5C_4H_8O$ (middle), and $SbPh_5$ nonsolvate (right). (b) Electronic absorption spectra of these substances dissolved in *n*-pentane.

As to how the color of the nonsolvate crystals provides an explanation for the disagreement between the present work and the previous vibrational spectroscopic work; the authors of the previous work indicate that "crude pentaphenylantimony was recrystallized from isooctane. The pentaphenylantimony formed in this way had a slight yellow color, but this could be removed by dissolving the recrystallized product in a minimum amount of benzene and precipitating the pentaphenylantimony with methanol."[36] In fact, a number of preparations of $SbPh_5$ reference a yellow color in the product.[11, 36, 45, 48] The authors of the previous vibrational study sought to follow a similar strategy to that described in this work: a spectrum collected from a solid whose structure had been crystallographically determined was compared to a spectrum collected from solutions of that solid. Of great importance however, the

previous Raman and IR spectra were not collected from a yellow material based on the assumption that the yellow color arose from an impurity, and the solid-state spectra were instead collected from a presumably colorless and recrystallized material. Our results suggest that a colorless form of $SbPh_5$ may, in fact, have featured the $SbPh_5$ in a trigonal bipyramidal geometry rather than the intended square pyramidal geometry. This would explain the agreement between the previously reported solid- and solution-phase vibrational spectra and our presently reported spectra of the $SbPh_5$ hemisolvates and solutions.

3.3 Conclusion

In summary, we have collected data using Sb K-edge and L_{III}-edge XAS, as well as Raman spectroscopy, that suggest $SbPh_5$ assumes a trigonal bipyramidal geometry in solution. This resolves a long-standing physical inorganic conundrum posed by this compound, and more importantly that no factors beyond those involved in simple VSEPR theory are necessary to understand its structure. This helps reinforce the idea that despite its simplicity, VSEPR theory is still useful and significant. Crystalline solids in which $SbPh_5$ assumes a known square pyramidal or TBP geometry were used as references to which solution-state spectra were compared. The disagreement between our data and the previously reported vibrational spectroscopic work is explained with reference to the fact that the crystalline nonsolvate $SbPh_5$ is yellow in color. We believe that this work generally demonstrates the utility of XANES in elucidating the structure of Sb-containing

compounds, a problem currently faced in modern fundamental and bioinorganic main-group chemistry.

3.4 Experimental Methods

General methods

All solvents and reagents were commercially available and used as received unless stated otherwise. THF was dried using 3-Å molecular sieves. $CDCl_3$ was purchased from Cambridge Isotope Laboratories and used as received. ^{1}H and $^{13}C\{^{1}H\}$ NMR spectra were recorded on a Bruker Avance III HD 500 MHz NMR spectrometer equipped with a multinuclear Smart Probe. Chemical shifts in the ^{1}H and $^{13}C\{^{1}H\}$ NMR spectra are reported in ppm as chemical shifts from tetramethylsilane and were referenced using the $CHCl_3$ (^{1}H, 7.26 ppm) and $CDCl_3$ (^{13}C, 77.0 ppm) solvent signals. Elemental analyses were performed by Midwest Microlabs (Indianapolis, IN). UV-visible absorption spectra were measured on a Shimadzu UV-2401PC dual-beam spectrophotometer. Raman spectra were acquired using a Thermo Fisher DXR Raman microscope. Optical microscopy and image capture were performed using an SZX16 Olympus stereomicroscope equipped with an Olympus SZX2-ILLK transmitted light illumination base and an Olympus DP70 digital camera. $SbPh_5$ was synthesized as previously described.[49]

Isolation of $SbPh_5$ cyclohexane hemisolvate ($SbPh_5 \cdot \frac{1}{2}C_6H_{12}$)

Crude $SbPh_5$ (972.1 mg, 1.92 mmol) was dissolved in Et_2O (32 mL). Cyclohexane (10 mL) was added and the solution was cooled to –20 °C for 12 h. $SbPh_5 \cdot \frac{1}{2}C_6H_{12}$ was collected as large, colorless crystals. Yield 665 mg (63%). ^{1}H NMR

(500 MHz, $CDCl_3$) δ=7.42-7.33 (m, 10H; Ar-H), 7.32-7.27 (m, 5H; Ar-H), 7.25-7.19 (m, 10H; Ar-H), 1.44 ppm (s, 6H; CH_2); $^{13}C\{^1H\}$ NMR (126 MHz, $CDCl_3$) δ=147.15, 135.29, 128.48, 128.03, 27.07 ppm; UV/Vis (*n*-pentane): λ_{max} (ε, $mol^{-1}dm^3cm^{-1}$)=305 (1779), 261 (4773); elemental analysis calcd (%) for $SbC_{33}H_{31}$: C 72.15, H 5.69; found: C 72.18, H 5.74.

Isolation of $SbPh_5$ THF hemisolvate ($SbPh_5 \cdot ½C_4H_8O$)

Crude $SbPh_5$ (997.9 mg, 1.97 mmol) was dissolved in THF (12 mL). *n*-Pentane (45 mL) was added and the solution was then cooled to –20 °C for 12 h. The THF hemisolvate of $SbPh_5$ was collected as small, colorless crystals. Yield 798 mg (75%). ^1H NMR (500 MHz, $CDCl_3$) δ=7.42-7.33 (m, 10H; Ar-H), 7.32-7.27 (m, 5H; Ar-H), 7.25-7.19 (m, 10H; Ar-H), 3.76 (s, 2H; CH_2), 1.86 ppm (s, 2H; CH_2); $^{13}C\{^1H\}$ NMR (126 MHz, $CDCl_3$) δ=147.14, 135.28, 128.48, 128.02, 68.12, 25.76 ppm; UV/Vis (*n*-pentane): λ_{max} (ε, $mol^{-1}dm^3cm^{-1}$)=305 (1805), 261 (4857); elemental analysis calcd (%) for $SbC_{32}H_{29}O_{0.5}$: C 70.74, H 5.38; found: C 70.56, H 5.40.

Isolation of solvent-free $SbPh_5$

Crude $SbPh_5$ (947.5 mg, 1.87 mmol) was dissolved in Et_2O (25 mL). *n*-Pentane (20 mL) was added and the solution was cooled to –20 °C for 12 h. Solvent-free $SbPh_5$ was collected as large, yellow crystals. Yield 595 mg (63%). ^1H NMR (500 MHz, $CDCl_3$) δ=7.42-7.33 (m, 10H; Ar-H), 7.32-7.27 (m, 5H; Ar-H), 7.25-7.19 ppm (m, 10H; Ar-H); ^{13}C NMR (126 MHz, $CDCl_3$) δ=147.15, 135.29, 128.48, 128.03 ppm; UV/Vis (*n*-pentane): λ_{max} (ε, $mol^{-1}dm^3cm^{-1}$)=305 (1758), 261 (4817); elemental analysis calcd (%) for $SbC_{30}H_{25}$: C 71.03, H 4.97; found: C 70.72, H 4.97.

DFT calculations

All calculations were performed using ORCA (version 4.2.1).[50, 51] Coordinates for the two geometries of $SbPh_5$ (square pyramidal and trigonal bipyramidal) were taken from the presently refined crystal structures of $SbPh_5$ and $SbPh_5 \cdot ½C_6H_{12}$, respectively. Hydrogen atom positions were normalized to account for the systematic underestimation of C–H bond lengths by X-ray crystallography. XAS and UV-Vis TDDFT calculations were performed with the dispersion- and range-corrected functional ωB97X-D3BJ, the second-order Douglas-Kroll-Hess (DKH2) approximation, and an earlier version of the relativistically contracted TZVP basis set (old-DKH-TZVP(-f)).[52-55] The resolution of the identity chain of spheres (RIJCOSX) approximation was employed with an appropriate segmented all-electron relativistically contracted (SARC/J) auxiliary basis set.[56, 57] Increased convergence criteria were employed during the self-consistent field process (tightSCF) and the size of the integration grid was increased (Grid5 NOFINALGRID). Sb K-edge TDDFT involved the calculation of 50 singlet roots (affording 50 transitions). The effects of spin-orbit coupling (SOC) were included for Sb L-edge TDDFT calculations, which involved the calculation of 300 roots, both singlet and triplet (affording 1200 transitions). SOC was also included in the UV-Vis TDDFT, which involved the calculation of 40 roots, both singlet and triplet (affording 160 transitions).

X-ray absorption spectroscopy

XAS data were collected at beamlines 7-3 (for the Sb K edge) and 4-3 (for the Sb L_{III} edge) at the Stanford Synchrotron Radiation Lightsource (SSRL) using Si(220)

and Si(111) double crystal monochromators, respectively. On 7-3, solid samples were placed into aluminum sample holders sealed with Kapton tape and solution samples were loaded into 1-cm path-length acrylic cuvettes. Samples were flash frozen in liquid nitrogen and maintained at 10 K using a He-flow cryostat (Oxford instruments, Abingdon, UK). To gain access to the high energies of the Sb K-edge, the beamline was operated in mirrorless mode, employing a 0.5 mm vertical aperture so as to give adequate energy resolution. The X-ray absorption spectrum was measured using N_2-filled gas-ionization chambers employing a sweeping voltage of 1.8 kV and operating above the recombination region. The incident beam energy was calibrated to the lowest-energy K-edge inflection from Sb foil (assumed to be 30488.0 eV). For the Sb L_{III}-edge spectra, measurements were made at room temperature either as finely powdered solids dusted onto adhesive tape or in solution using modified SPEX CertiPrep (Metuchen NJ, USA) X-cell sample cups employing a 3 μm thick Etnom® window (Chemplex Industries, Inc, Palm City FL, USA) to transmit the X-ray fluorescence, which was measured with a large-area PIN diode (Canberra Industries, Meriden CT, USA). The incident beam energy was calibrated to the lowest L_{III}-edge inflection of an Sb foil standard (assumed to be 4132.3 eV). XAS data reduction and analysis were performed using the EXAFSPAK suite of programs.[58] Each spectrum was calibrated as described above and replicates were averaged after screening for anomalies. Because of photodegradation in the Sb L_{III}-edge spectra, only the first scan was used. A background function was subtracted from each spectrum in order to bring the pre-edge region to zero. Spectra were normalized using the spline method.

X-ray crystallography

Crystals of $SbPh_5$, $SbPh_5 \cdot ½C_6H_{12}$, and $SbPh_5 \cdot ½C_4H_8O$ were grown as described above, selected under a microscope, loaded onto a nylon fiber loop using Paratone-n, and mounted onto a Rigaku XtaLAB Synergy-S single crystal diffractometer. Each crystal was cooled to 100 K under a stream of nitrogen. Diffraction of either Cu Kα or Mo Kα radiation from a PhotonJet-S microfocus source was detected using a HyPix-6000HE hybrid photon counting detector. Screening, indexing, data collection, and data processing were performed with CrysAlis^{Pro}.[59] The structures were solved using SHELXT and refined using SHELXL.[60, 61] All non-H atoms were refined anisotropically. H atoms were placed at geometrically calculated positions and refined with a riding model. The U_{iso} of the H atoms were set equal to 1.2(U_{eq}) of the carbon atoms to which they are attached. In the case of the THF hemisolvate $SbPh_5 \cdot ½C_4H_8O$, one of the axial phenyl rings is disordered across two slightly different positions. Moreover, the single THF molecule in the unit cell was modeled as disordered across the inversion center with similarity restraints applied to the bond lengths, bond angles, and displacement parameters.[62]

Raman spectroscopy

Spectra were acquired either directly from solid crystalline samples of $SbPh_5$, $SbPh_5 \cdot ½C_6H_{12}$, and $SbPh_5 \cdot ½C_4H_8O$, which were isolated as described above. A solution of $SbPh_5$, prepared by dissolving the nonsolvate of $SbPh_5$ (20 mg) in toluene (1 mL), was also analyzed.

3.5 References

1. Haaland, A., *Molecules & Models: The molecular structures of main group element compounds*. Oxford University Press: Oxford ; New York, 2008; p xviii, 311 p.

2. Norman, N. C., *Chemistry of Arsenic, Antimony, and Bismuth*. 1st ed.; Blackie Academic & Professional: London ; New York, 1998; p xii, 483 p.

3. Greenwood, N. N.; Earnshaw, A., *Chemistry of the Elements*. 2nd ed.; Butterworth-Heinemann: Oxford ; Boston, 1997; p xxii, 1341 p.

4. Sidgwick, N. V.; Powell, H. M., Stereochemical types and valency groups. *Proceedings of the Royal Society of London. Series A. Mathematical and Physical Sciences* **1940,** *176* (965), 153-180.

5. Gillespie, R. J.; Nyholm, R. S., Inorganic stereochemistry. *Quarterly Reviews, Chemical Society* **1957,** *11* (4), 339-380.

6. Muetterties, E. L.; Mahler, W.; Schmutzler, R., Stereochemistry of Phosphorus(V) Fluorides. *Inorganic Chemistry* **1963,** *2* (3), 613-618.

7. Muetterties, E. L.; Mahler, W.; Packer, K. J.; Schmutzler, R., Five-Coordinate Stereochemistry. *Inorganic Chemistry* **1964,** *3* (9), 1298-1303.

8. Gillespie, R. J., The valence-shell electron-pair repulsion (VSEPR) theory of directed valency. *Journal of Chemical Education* **1963,** *40* (6), 295-301.

9. Wheatley, P. J.; Wittig, G., The Structure of Pentaphenyl-phosphorus, -arsenic, and -antimony. *Proceedings of the Chemical Society* **1962,** (July), 251-252.

10. Wheatley, P. J., An X-ray diffraction determination of the crystal and molecular structure of pentaphenylantimony. *Journal of the Chemical Society* **1964**, 3718-3723.

11. Beauchamp, A. L.; Bennett, M. J.; Cotton, F. A., A reinvestigation of the crystal and molecular structure of pentaphenylantimony. *Journal of the American Chemical Society* **1968,** *90* (24), 6675-6680.

12. Addison, A. W.; Rao, T. N.; Reedijk, J.; van Rijn, J.; Verschoor, G. C., Synthesis, structure, and spectroscopic properties of copper(II) compounds containing nitrogen–sulphur donor ligands; the crystal and molecular structure of aqua[1,7-bis(*N*-methylbenzimidazol-2′-yl)-2,6-dithiaheptane]copper(II) perchlorate. *Journal of the Chemical Society, Dalton Transactions* **1984,** (7), 1349-1356.

13. Brabant, C.; Blanck, B.; Beauchamp, A. L., Structure cristalline du pentaphenylantimoine dans le solvate cyclohexanique $(C_6H_5)_5Sb \cdot C_6H_{12}$. *Journal of Organometallic Chemistry* **1974,** *82* (2), 231-234.

14. Brock, C. P.; Ibers, J. A., The role of crystal packing forces in the structure of pentaphenylantimony. *Acta Crystallographica Section A* **1976,** *32* (1), 38-42.

15. Brock, C. P.; Webster, D. F., The crystal structure of pentaphenylarsenic: implications for the role of crystal packing forces in the structures of penta-aryl Group V molecules. *Acta Crystallographica Section B* **1976,** *32* (7), 2089-2094.

16. Brock, C. P., Lattice energy calculations for $(C_6H_5)_5M \cdot {}^1/_2C_6H_{12}$, *M*= P, As and Sb: Towards an understanding of crystal packing in the pentaphenyl group V compounds. *Acta Crystallographica Section A* **1977,** *33* (6), 898-902.

17. Brock, C. P., The role of Coulombic interactions in explaining the anomalous structure of pentaphenylantimony. *Acta Crystallographica Section A* **1977,** *33* (1), 193-197.

18. Brock, C. P., Systematic Study of Crystal Packing. In *Implications of Molecular and Materials Structure for New Technologies*, 1999; pp 251-262.

19. Desiraju, G. R., *The Crystal as a Supramolecular Entity*. Wiley: Chichester ; New York, 1996; p xi, 314 p., 8 p. of plates.

20. Gillespie, R. J., The VSEPR model revisited. *Chemical Society Reviews* **1992,** *21* (1), 59-69.

21. Gillespie, R. J., Fifty years of the VSEPR model. *Coordination Chemistry Reviews* **2008,** *252* (12-14), 1315-1327.

22. Clauss, A. D.; Nelsen, S. F.; Ayoub, M.; Moore, J. W.; Landis, C. R.; Weinhold, F., Rabbit-ears hybrids, VSEPR sterics, and other orbital anachronisms. *Chemistry Education Research and Practice* **2014,** *15* (4), 417-434.

23. Morse, P. M.; Girolami, G. S., Are d^0 ML_6 complexes always octahedral? The x-ray structure of trigonal-prismatic $[Li(tmed)]_2[ZrMe_6]$. *Journal of the American Chemical Society* **1989,** *111* (11), 4114-4116.

24. Haaland, A.; Hammel, A.; Rypdal, K.; Volden, H. V., The coordination geometry of gaseous hexamethyltungsten is not octahedral. *Journal of the American Chemical Society* **1990,** *112* (11), 4547-4549.

25. Kaupp, M., The Structure of Hexamethyltungsten, $W(CH_3)_6$: Distorted Trigonal Prismatic with C_3 Symmetry. *Journal of the American Chemical Society* **1996,** *118* (12), 3018-3024.

26. Landis, C. R.; Cleveland, T.; Firman, T. K., Structure of $W(CH_3)_6$. *Science* **1996,** *272* (5259), 182a.

27. Pfennig, V.; Seppelt, K., Crystal and Molecular Structures of Hexamethyltungsten and Hexamethylrhenium. *Science* **1996,** *271* (5249), 626-628.

28. Landis, C. R.; Cleveland, T.; Firman, T. K., Making Sense of the Shapes of Simple Metal Hydrides. *Journal of the American Chemical Society* **1995,** *117* (6), 1859-1860.

29. Seppelt, K., Nonoctahedral Structures. *Accounts of Chemical Research* **2003,** *36* (2), 147-153.

30. Beattie, I. R.; Livingston, K. M. S.; Ozin, G. A.; Sabine, R., The shape of pentaphenylantimony and pentaphenylarsenic in solution. *Journal of the Chemical Society, Dalton Transactions* **1972,** (7), 784-786.

31. Brabant, C.; Hubert, J.; Beauchamp, A. L., The Crystal and Molecular Structure of Penta-*p*-tolylantimony, $(p\text{-}CH_3C_6H_4)_5Sb$. *Canadian Journal of Chemistry* **1973,** *51* (17), 2952-2957.

32. Kuykendall, G. L.; Mills, J. L., Solution studies of some pentaarylantimony(V) compounds. *Journal of Organometallic Chemistry* **1976,** *118* (2), 123-128.

33. Berry, R. S., Correlation of Rates of Intramolecular Tunneling Processes, with Application to Some Group V Compounds. *The Journal of Chemical Physics* **1960,** *32* (3), 933-938.

34. Wheatley, P. J., The crystal and molecular structure of pentaphenylphosphorus. *Journal of the Chemical Society (Resumed)* **1964**, 2202-2206.

35. Müller, G.; Bildmann, U. J., Crystal and Molecular Structure of $P(C_6H_5)_5 \cdot 0.5$ THF. *Zeitschrift für Naturforschung B* **2004,** *59* (11-12), 1411-1414.

36. Kok, G. L., A reinvestigation of the vibrational spectroscopy of pentaphenylarsenic and pentaphenylantimony. *Spectrochimica Acta Part A: Molecular Spectroscopy* **1974,** *30* (4), 961-967.

37. Schmuck, A.; Buschmann, J.; Fuchs, J.; Seppelt, K., Structure and Color of Pentaphenylbismuth. *Angewandte Chemie International Edition in English* **1987,** *26* (11), 1180-1182.

38. Schmuck, A.; Buschmann, J.; Fuchs, J.; Seppelt, K., Structure and Color of Substituted Pentaphenylbismuth. *Angewandte Chemie International Edition in English* **1987,** *26* (11), 1180-1182.

39. El-Issa, B. D.; Pyykko, P.; Zanati, H. M., MS Xα studies on the colors of $BiPh_5$, $PbCl_6^{2-}$ and WS_4^{2-}: Are relativistic effects on the LUMO important? *Inorganic Chemistry* **1991,** *30* (13), 2781-2787.

40. Seppelt, K., Structure, Color, and Chemistry of Pentaaryl Bismuth Compounds. *Advances in Organometallic Chemistry* **1992,** *34*, 207-217.

41. García-Monforte, M. A.; Alonso, P. J.; Ara, I.; Menjón, B.; Romero, P., Solid-State and Solution Structure of a Hypervalent AX_5 Compound: $Sb(C_6F_5)_5$. *Angewandte Chemie International Edition* **2012,** *51* (11), 2754-2757.

42. Schröder, G.; Okinaka, T.; Mimura, Y.; Watanabe, M.; Matsuzaki, T.; Hasuoka, A.; Yamamoto, Y.; Matsukawa, S.; Akiba, K. Y., Syntheses, crystal and solution structures, ligand-exchange, and ligand coupling reactions of mixed pentaarylantimony compounds. *Chemistry - A European Journal* **2007,** *13* (9), 2517-2529.

43. Lindquist-Kleissler, B.; Wenger, J. S.; Johnstone, T. C., Analysis of Oxygen–Pnictogen Bonding with Full Bond Path Topological Analysis of the Electron Density. *Inorganic Chemistry* **2021,** *60* (3), 1846-1856.

44. Wenger, J. S.; Johnstone, T. C., Unsupported monomeric stibine oxides (R_3SbO) remain undiscovered. *Chemical Communications* **2021,** *57* (28), 3484-3487.

45. Thepe, T. C.; Richard, S. J.; Garascia, J.; Selvoski, M. A.; Patel, A. N., Brief Note Improved Methods for the Synthesis of Antimony Triacetate, Triphenylantimony Diacetate, and Pentaphenylantimony. *Ohio Journal of Science* **1977,** *77* (3), 134-135.

46. Whiffen, D. H., 273. Vibrational frequencies and thermodynamic properties of fluoro-, chloro-, bromo-, and iodo-benzene. *Journal of the Chemical Society* **1956**, 1350-1356.

47. Mackay, K. M.; Sowerby, D. B.; Young, W. C., Infrared spectra of phenyl derivatives of germanium, arsenic and antimony. *Spectrochimica Acta Part A: Molecular Spectroscopy* **1968,** *24* (5), 611-631.

48. Wittig, G.; Clauß, K., Pentaphenyl-arsen und Pentaphenyl-antimon. *Justus Liebigs Annalen der Chemie* **1952,** *577* (1), 26-39.

49. Fujiwara, M.; Tanaka, M.; Baba, A.; Ando, H.; Souma, Y., Reaction of pentaarylantimony with acid halide, aldehyde and ketone. *Journal of Organometallic Chemistry* **1996,** *508* (1-2), 49-52.

50. Neese, F., The ORCA program system. *WIREs Computational Molecular Science* **2012,** *2* (1), 73-78.

51. Neese, F., Software update: the ORCA program system, version 4.0. *WIREs Computational Molecular Science* **2018,** *8* (1), e1327.

52. Chai, J.-D.; Head-Gordon, M., Systematic optimization of long-range corrected hybrid density functionals. *The Journal of Chemical Physics* **2008,** *128* (8), 084106.

53. Grimme, S.; Antony, J.; Ehrlich, S.; Krieg, H., A consistent and accurate ab initio parametrization of density functional dispersion correction (DFT-D) for the 94 elements H-Pu. *The Journal of Chemical Physics* **2010,** *132* (15), 154104.

54. Grimme, S.; Ehrlich, S.; Goerigk, L., Effect of the damping function in dispersion corrected density functional theory. *Journal of Computational Chemistry* **2011,** *32* (7), 1456-1465.

55. Weigend, F.; Ahlrichs, R., Balanced basis sets of split valence, triple zeta valence and quadruple zeta valence quality for H to Rn: Design and assessment of accuracy. *Physical Chemistry Chemical Physics* **2005,** *7* (18), 3297-3305.

56. Neese, F.; Wennmohs, F.; Hansen, A.; Becker, U., Efficient, approximate and parallel Hartree–Fock and hybrid DFT calculations. A 'chain-of-spheres' algorithm for the Hartree–Fock exchange. *Chemical Physics* **2009,** *356* (1-3), 98-109.

57. Pantazis, D. A.; Chen, X.-Y.; Landis, C. R.; Neese, F., All-Electron Scalar Relativistic Basis Sets for Third-Row Transition Metal Atoms. *Journal of Chemical Theory and Computation* **2008,** *4* (6), 908-919.

58. George, G. N.; Pickering, I. J. *EXAFSPAK: A suite of computer programs for analysis of X-ray absorption spectra*, Stanford Synchrotron Radiation Laboratory: Stanford, CA, USA, 1995.

59. Rigaku Oxford Diffraction *CrysAlis^{Pro} software system*, version 1.171.40.78a; Rigaku Corporation: Wroclaw, Poland, 2020.

60. Sheldrick, G. M., *SHELXT* - Integrated space-group and crystal-structure determination. *Acta Crystallographica, Section A* **2015,** *71*, 3-8.

61. Sheldrick, G. M., Crystal structure refinement with *SHELXL*. *Acta crystallographica, Section C* **2015,** *71*, 3-8.

62. Muller, P., Practical suggestions for better crystal structures. *Crystallography Reviews* **2009,** *15* (1), 57-83.

Chapter 4

Synthesis and Characterization of $Sb(Tol)_3(O_2R)$ Model Compounds

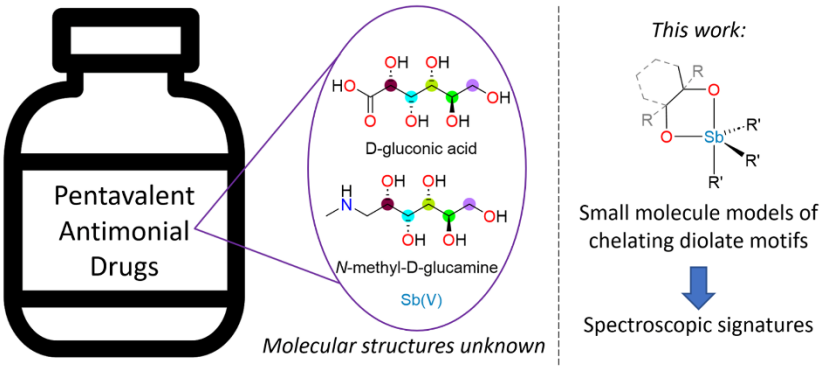

Published in part in: Lindquist-Kleissler, B.; Johnstone, T. C. *Dalton Trans.*, **2023,** *52*, 9229.

4.1 Introduction

The pentavalent antimonials, sodium stibogluconate and meglumine antimoniate, are prepared by combining an Sb(V) precursor and a polyalchol, D-gluconic acid (GLU) or *N*-methyl-D-glucamine (NMG).[1] Although the structures of these molecules are still unknown, the oxophilicity of Sb(V) suggests Sb binds to the polyalcohol ligand through one or more deprotonated hydroxyl groups (Scheme 4.1). Furthermore, chelation by two hydroxyl groups is favorable due to the formation of an unstrained five-membered ring. As described in Chapter 1, both of these drugs have been studied previously via NMR spectroscopy and mass spectrometry, however the insight gained is hampered by complicated and difficult to interpret data.[1] Due to the nature of the ligands' complexity (i.e number of possible binding modes, stereochemistry and potential mixtures of compounds), spectra of these molecules can be very difficult to decipher. We hypothesized that, by simplifying the organic ligands, we might gain clearer insight on the bonding and structure of the pentavalent antimonials.

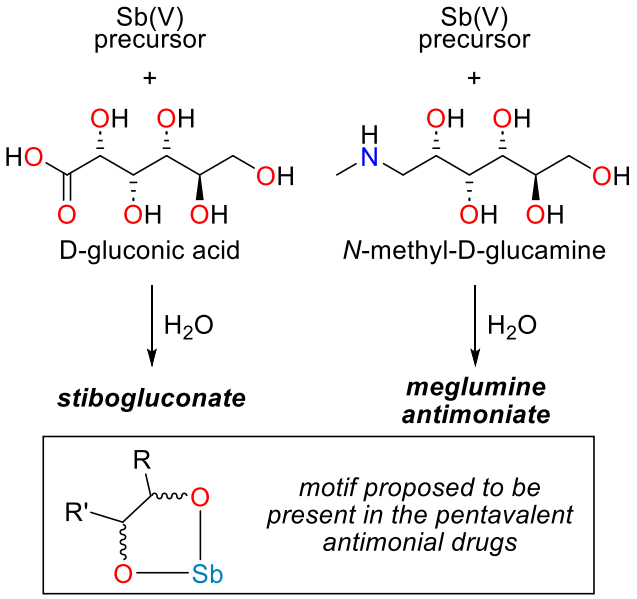

Scheme 4.1. Overall synthesis of the antileishmanial pentavalent antimonial drugs stibogluconate and meglumine antimoniate from an Sb(V) precursor such as hydrolyzed $SbCl_5$ or $K[Sb(OH)_6]$. Boxed at bottom is a representation of the chelating diolate motif commonly proposed to be present in the drugs.

To investigate this question, we synthesized a series of cyclic organostiboranes spanning the stereochemical space afforded by a vicinal diolate motif. We chose to work with the $Sb(tol)_3$ fragment based on the work presented in Chapter 3.[2] Due to the stability of the molecules in the pentaphenylantimony work, we believed further increasing the bulk of the molecules by installing tolyl groups would increase their stability and ability to crystallize. Further advantages of this framework are the ease of synthesis and the compounds' solubility in a variety of organic solvents. Although there are a number of options for diols chelating the Sb center, chelation *via* vicinal diols is particularly favorable due to the formation of unstrained five-membered rings. For these reasons we chose to focus on compounds

where the Sb atom is bound by a vicinal diol, of which NMG and GLU have several (Scheme 4.2). We acknowledge that GLU contains a carboxylic acid that could potentially bind to the Sb center, but we have chosen to restrict this work to investigating the vicinal diolate motif. For both NMG and GLU, there are three types of vicinal hydroxyls to which the Sb can bind: those with the same stereochemistry (i.e. *R,R* or *S,S)*, those with opposite stereochemistry (i.e. *R,S*), and one secondary alcohol and one primary alcohol (Scheme 4.2).

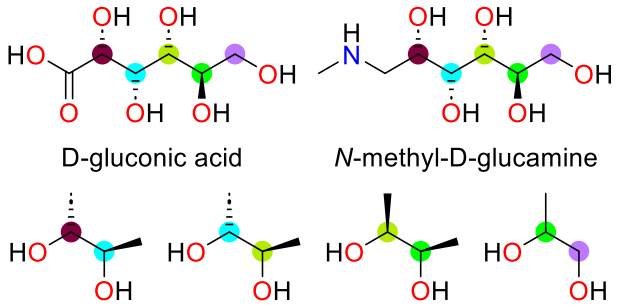

Scheme 4.2. Depiction of the relationship between the stereochemistry of the vicinal diols used in this study (*bottom*) and the stereochemistry of the *N*-methyl-D-glucamine and D-gluconic acid ligand precursors used in the pentavalent antimonial antileishmanial drugs (*top*).

Knowing the structure and spectroscopic signatures of these compounds could provide insight into the structures of the pentavalent antimonials and allow for clearer understanding of their mechanisms of action and ultimately their derivatization, as discussed in Chapters 1 and 3.

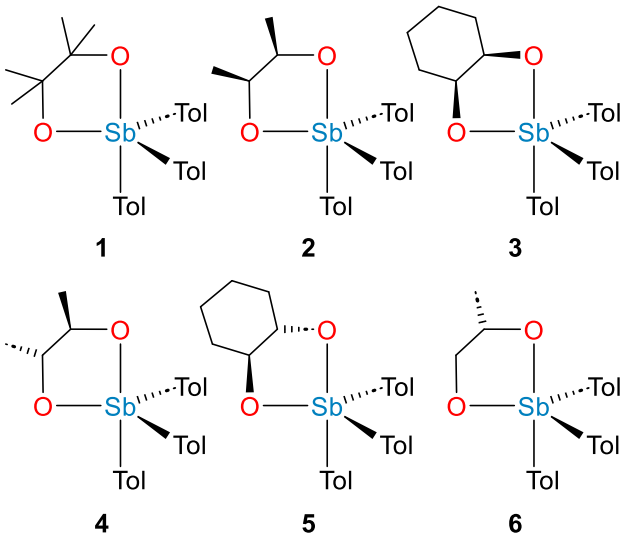

Scheme 4.3. Structures of model compounds **1-6** investigated in this study.

4.2 Results and Discussion

Synthesis of Model Compounds

The cyclic organostiboranes **1-6** can also be viewed as derivatives of the five-membered 1,3-dioxa-2-stibolane heterocycle, however, for this work we will discuss them as Sb(V) complexes bearing chelating diolate ligands. Similar cyclic organostiboranes have been previously reported in the literature, but the majority of them contain chelating dicarboxylates or α-hydroxycarboxylates.[3-5] A few examples from the literature do contain the chelating diolate motif, and an analog of **1** (with Ph instead of tol substituents) has been previously reported.[6] This analog was isolated in an orthogonal fashion to our own synthesis. The synthesis of the analog of **1** was achieved by insertion of $SbPh_3$ into the O—O bond of 3,3,4,4-tetramethyl-1,2-dioxetane, which could be described as an oxidative addition of the 1,2-dioxetane

derivative to the stibine. Another similar compound from the literature, a derivative of **6**, contains a 1,2-ethanediolate ligand instead of the 1,2-propanediolate featured in **6**. The isolation of this derivative was achieved by oxidizing a triarylstibine with *tert*-butyl hydroxide in the presence of ethylene glycol.[7] The last analog of note found in the literature features two pinacolate ligands and a single tolyl group and was prepared from tolylstibonic acid.[8] We note that 1-oxa-3-aza-2-(σ^5,λ^5)-stibolanes have been prepared in a similar manner to our own, from dihalostiboranes and *o*-aminophenols.[9]

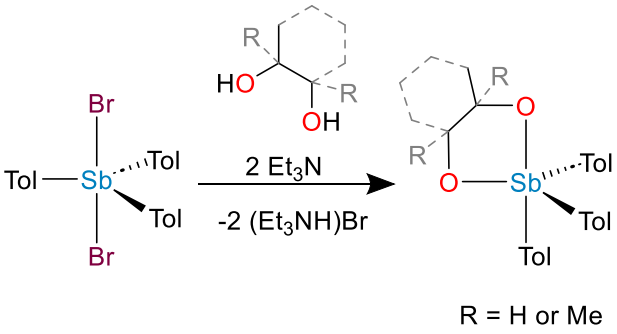

Scheme 4.4. Synthesis of **1-6**.

Synthesis of **1-6** was done as depicted in Scheme 4.4. The synthesis of $Sb(tol)_3Br_2$ was done as previously described.[10] Compounds **1-6** were synthesized by stirring an equimolar mixture of $Sb(tol)_3Br_2$ and the diol of interest at room temperature in DCM with 2 equiv Et_3N for 1 h. The DCM was then removed to yield a mixture of the target compound and $(Et_3NH)Br$. The Sb(V) compound was extracted with Et_2O and recrystallized from MeCN at —20 ℃ to yield colorless crystals. These crystals appear to be stable in ambient conditions for long periods of

time. We also found the solid mixture of $(Et_3NH)Br$ and the target compound could be washed with H_2O to remove the $(Et_3NH)Br$ and leave the product, however this procedure appeared to promote hydrolysis of the target compounds, resulting in oxo-bridged species, including the oxo-bridged species $[(tol)_3Sb(\mu\text{-}C_4H_8O_2)]_2O$, which was crystallographically characterized (Figure 4.1). We note that these procedures can be carried out in toluene as in similar previously reported syntheses, however we obtained cleaner product formation in DCM.

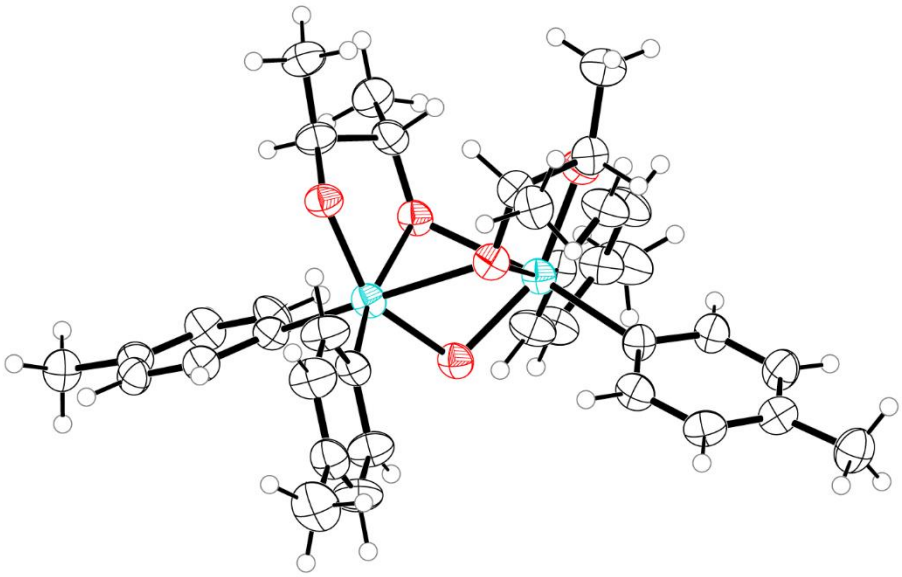

Figure 4.1. Thermal ellipsoid plot (50% probability, H atoms as spheres of arbitrary radius) of a hydrolysis decomposition product observed to form during the synthesis of butanediolate complexes**.** Color code: Sb teal, O red, C black, H white.

Compound **1** served as a starting point to validate our synthetic methodology and to provide us with a foundation to base our analyses, due to its simplicity and lack of any stereochemistry. Compound **4**, prepared with 2*R*,3*R*-butanediol, provides an example of a complex bearing a chelating diolate motif with the two stereocenters

of identical handedness as mentioned above. Compound **5**, prepared with 1*S*,2*S*-cyclohexanediol, provides robustness in our method of analysis due to it containing two stereocenters of identical handedness (as in **1**) but with a different diolate ligand. The syntheses of **2** and **3**, prepared from the *meso* compounds 2*R*,3*S*-butanediol and 1*R*,2*S*-cyclohexanediol respectively, were motivated by the same philosophy as above. These two compounds provide examples of chelating diolates containing two stereocenters with opposite handedness. Finally, compound **6**, prepared from *S*-1,2-propanediol, provides an example of a chelating, vicinal diolate bound through one primary alkoxide and one secondary alkoxide.

X-Ray Crystallography

The structures of all six compounds were unambiguously confirmed crystallographically (Figure 4.1 and Table 4.1). The starting stibine $Sb(tol)_3$ was also crystallographically characterized (Figure C.1 and Table C.1). Crystals suitable for X-ray diffraction analysis were grown from saturated MeCN solutions at —20 °C for all six model compounds. Compound **1** crystallized in the centrosymmetric space group $P2_1/c$, which is unsurprising as it lacks any stereocenter in the pinacolate ligand. Compounds **2** and **3** also crystallized with centrosymmetry in space group $P\bar{1}$. Compounds **4-6**, all crystallized in Sohncke space groups, as expected due to the enantiomerically pure diols used in their preparation. Crystals of **4**, **5**, and **6** all feature two crystallographically independent molecules in the asymmetric unit. Interestingly, in each structure, the two crystallographically independent molecules are related by a pseudoinversion center. For all three crystal structures, the Sb atom

and the aryl rings observe the pseudosymmetry, but the enantiomerically pure diolate ligand does not. In the structure of **4** (Figure 4.2), the pseudoinversion center lies at (0.74, 0.50, 0.76); a true inversion center at (0.75, 0.50, 0.75) would afford space group C_2/c. In the case of **5**, the pseudoinversion center lies at (0.49, 0.48, 0.50) and a true inversion center at (0.50, 0.50, 0.50) would afford space group $P\bar{1}$. In the case of **6**, the pseudoinversion center lies at (0.75, 0.75, 0.25); a true inversion center at this position would afford space group *Pbca*. The Flack parameters for **4**, **5**, and **6** do not deviate from 0 within 3σ, consistent with our proposal that these pseudoinversion centers are not missed, true crystallographic symmetries.

These intriguing observations, in part, lead us to further study the crystal structures of these molecules and promoted the work discussed in Chapter 5 of this thesis.

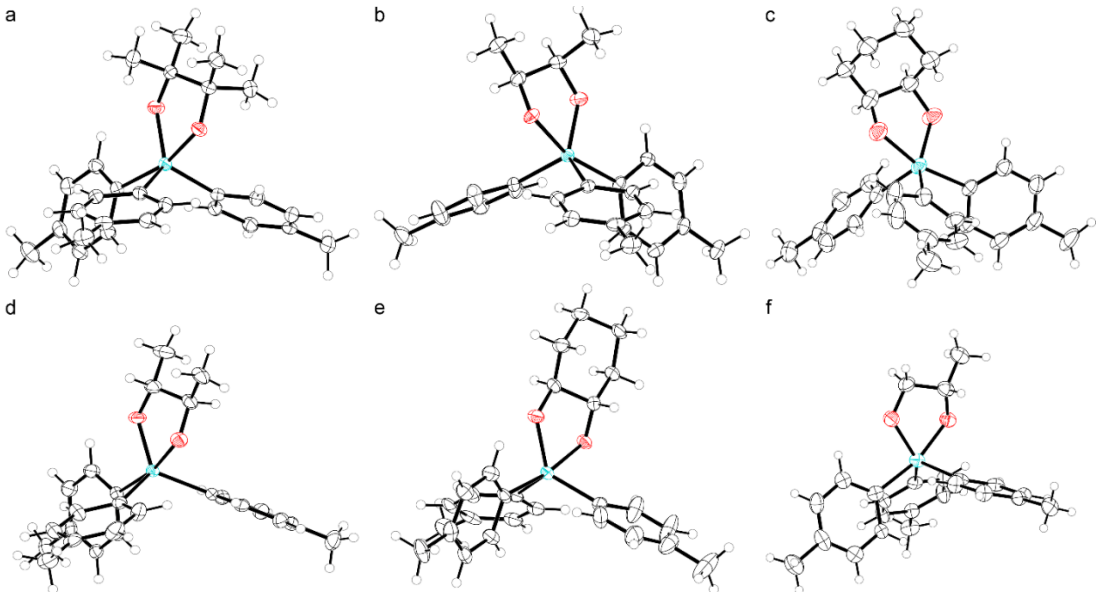

Figure 4.2. Thermal ellipsoid plots (50% probability) of **1**-**6** (a-f). Color code: Sb teal, O red, C black, H white spheres of arbitrary radius. For crystals with *Z*' > 1 (d-f), only one of the molecules in the asymmetric unit is shown. For **3** (c), only the major component of disorder is shown.

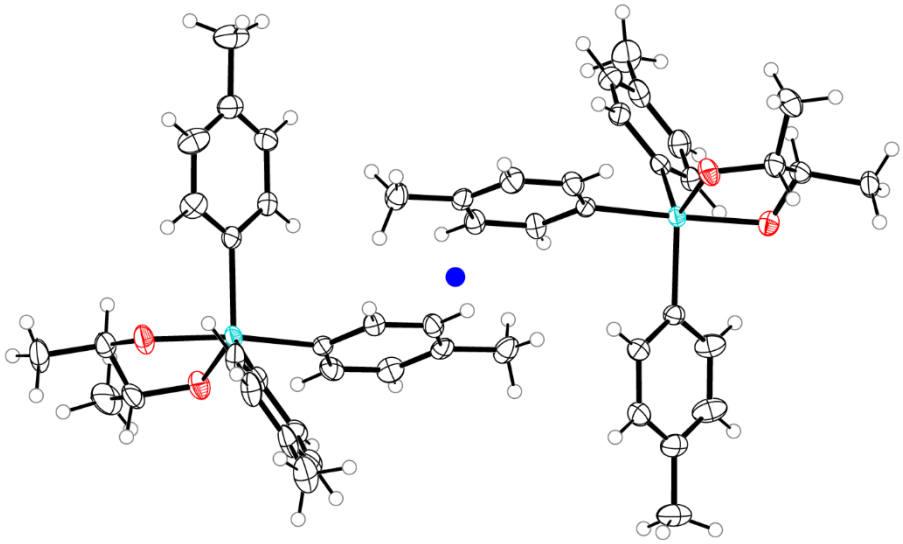

Figure 4.3. Thermal ellipsoid plots (50% probability, H atoms as spheres of arbitrary radius) of the complete contents of the asymmetric unit of the crystal structure of **4**. Blue disc represents the pseudoinversion center between the two molecules. Color code: Sb teal, O red, C black, H white.

Table 4.1. Refinement details for the crystal structures of compounds **1-3.**

	1	**2**	**3**
Formula	$C_{27}H_{33}O_2Sb$	$C_{25}H_{29}O_2Sb$	$C_{27}H_{31}O_2Sb$
FW	511.28	483.23	509.27
T (K)	100(2)	101(1)	101(2)
λ (Å)	1.54184	1.54184	1.54184
Crystal System	Monoclinic	Triclinic	Triclinic
Space group	$P2_1/c$	$P\bar{1}$	$P\bar{1}$
a (Å)	9.82520(10)	8.6242(2)	10.0944(4)
b (Å)	11.8813(2)	9.3045(2)	11.6974(5)
c (Å)	20.2807(3)	14.1213(3)	12.2709(6)
α (°)		79.804(2)	63.873(5)
β (°)	90.7870(10)	83.183(2)	84.156(4)
γ (°)		80.822(2)	65.488(4)
Volume (Å^3)	2367.27(6)	1096.19(4)	1177.82(11)
Z	4	2	2
ρ_{calc} (Mg/m^3)	1.435	1.464	1.436
Size (mm^3)	0.16×0.09× 0.06	0.15×0.13× 0.06	0.11×0.07×0.04
θ range (°)	4.313-67.684	3.194-67.684	4.032-67.070
Total data	33440	27604	27689
Unique data	4482	4461	4184
Parameters	278	258	338
Completeness	100.0%	99.7%	99.7%
R_{int}	5.16%	7.09%	6.63%
R_1 (I > 2σ)	2.37%	3.10%	3.92%
R_1 (all data)	2.61%	3.21%	4.38%
wR_2 (I > 2σ)	6.14%	8.17%	9.39%
wR_2 (all data)	6.28%	8.25%	9.61%
S	1.050	1.101	1.093
Flack *x*	—	—	—

Table 4.2. Refinement details for the crystal structures of compounds **4-6.**

	4	**5**	**6**
Formula	$C_{25}H_{29}O_2Sb$	$C_{27}H_{31}O_2Sb$	$C_{24}H_{27}O_2Sb$
FW	483.23	509.27	469.20
T (K)	100.5(9)	100(1)	100(1)
λ (Å)	1.54184	1.54184	1.54184
Crystal System	Monoclinic	Triclinic	Orthorhombic
Space group	*C*2	*P*1	$P2_12_12_1$
a (Å)	13.81140(10)	8.8969(2)	15.1979(5)
b (Å)	11.47050(10)	9.3354(2)	16.3230(8)
c (Å)	28.9055(2)	15.1475(4)	16.9475(6)
α (°)		76.082(2)	
β (°)	103.8970(10)	78.930(2)	
γ (°)		74.721(2)	
Volume ($Å^3$)	4445.27(6)	1166.83(5)	4204.3(3)
Z	8	2	8
ρ_{calc} (Mg/m^3)	1.444	1.449	1.483
Size (mm^3)	0.18×0.10×0.07	0.11×0.08×0.06	0.09×0.06×0.05
θ range (°)	3.150-67.684	3.034-66.575	3.760-67.684
Total data	68817	28265	60946
Unique data	8124	7799	7984
Parameters	516	585	496
Completeness	99.9%	100.0%	100.0%
R_{int}	4.92%	4.56%	9.96%
R_1 (I > 2σ)	2.04%	2.51%	4.83%
R_1 (all data)	2.05%	2.63%	5.71%
wR_2 (I > 2σ)	5.31%	6.05%	11.56%
wR_2 (all data)	5.31%	6.12%	11.99%
S	1.031	1.047	1.080
Flack *x*	-0.009(5)	-0.021(10)	0.001(13)

Geometry

Notably, the structure of each of the 2,3-butanediolate complexes superimposes upon that of the corresponding 1,2-cyclohexanediolate. For example, the structure of the 2*R*,3*S*-butanediolate (**2**) superimposes upon that of the *cis*-1,2-cycohexanediolate (**3**) and the structure of the 2*R*,3*R*-butanediolate (**4**) superimposes upon that of the *trans*-1,2-butanediolate (**5**). For **4** and **5**, their direct comparison requires inversion of one of the structures due to 1*S*,2*S*-cyclohexanediol being used instead of 1*R*,2*R*-cyclohexanediol. Furthermore, the 2*R*,3*R*-butanediolate (**4**) and 1,2-propanediolate (**6**) complexes superimpose upon the pinacolate complex (**1**). With successively more H atoms replaced by methyl groups (Figure C.2). This information leads us to believe that the molecular geometries obtained in these crystallographic experiments do indeed reflect the lowest-energy structures of these molecules. In the case of the two cyclohexanediolate complexes (**3** and **5**), there are distinct differences in the geometry and position of the cyclohexyl ring in the crystal structures. Due to the backbone stereochemistry of **3**, there is a significant deviation from coplanarity with the SbO_2C_2 ring (Figure 4.4). The angles between the normal of the planes that best fit the SbO_2C_2 ring and the C_6 ring for the two components of the disorder are 121.2(3)° and 121.4(5)°. The corresponding angles for the two crystallographically inequivalent molecules in compound **5** are 1.2(3)° and 2.1(3)°. As previously discussed in Chapters 1 and 3, valence-shell electron pair repulsion (VSEPR) theory predicts that the most stable geometry for a pentasubstituted, pentavalent (σ^5,λ^5) metal/metalloid compound is trigonal bipyramidal (D_{3h}). The other most common

geometry for these types of compounds is square pyramidal (C_{4v}). The τ parameter is useful in describing the geometry of such molecules because it captures the position of the molecule along the C_{2v}-symmetric normal coordinate that connects C_{4v} square pyramidal ($\tau = 0$) and D_{3h} trigonal bipyramidal ($\tau = 1$) geometries.[11] Interestingly, **1**-**6** display a large range in τ values, from 0.33 for **3** to 0.82 for **5** (Figure 4.2). The two compounds prepared from the *R*,*S*-diols (**2** and **3**) had the lowest τ values, and those prepared from the *R*,*R*-diols (**4** and **5**) had the highest τ values (Table 4.3).

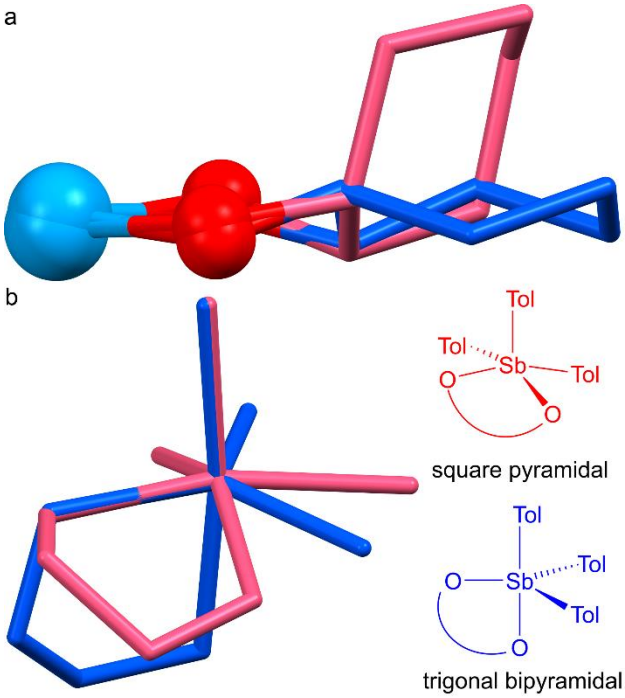

Figure 4.4. a) Side view of an overlay of the Sb-diolate moieties of **3** (light red) and **5** (blue) shown as sticks with the Sb and O atoms shown as teal and red spheres, respectively. b) Overlaid stick diagrams of square pyramidal **3** (light red, $\tau = 0.33$) and trigonal bipyramidal **5** (blue, $\tau = 0.82$) showing the differences in geometry about the Sb center. Tolyl groups are omitted for clarity.

Table 4.3. Crystallographically determined bond metrics for **1**-**6**.

	τ^c	Sb–O (Å)
1	0.56	1.9802(15), 2.0182(16)
2	0.45	1.990(2), 2.0211(19)
3[a]	0.33	1.986(8)/2.018(5), 2.017(3)
4[b]	0.75	1.975(3), 2.023(3) / 1.979(3), 2.023(3)
5[b]	0.82	1.981(6), 2.042(6) / 1.978(6), 2.045(6)
6[b]	0.64	1.980(7), 2.055(6) / 1.976(7), 2.050(6)

[a] Sb–O values provided for both components of the disordered cyclohexanediolate.
[b] Sb–O values provided for both crystallographically independent molecules in the asymmetric unit.
[c] Average values provided in instances of disorder or multiple crystallographically independent molecules.

Conformational Isomers

Compounds **1**-**6** all feature five-membered chelate rings containing the Sb atom, the O atoms, and the two backbone C atoms (SbO_2C_2). This ring, which can be described as a 1,3-dioxa-2-stibolane ring, is puckered in all compounds, making it nonplanar. These rings can be described using the ring twist notation with chirality assigned as either λ or δ using the skew line convention. For the achiral compounds **1**, **2**, and **3**, both ring twist conformers are present in the crystal structure and are isoenergetic. Compound **3** is disordered, and the major component of the disorder features the cyclohexane ring puckered in such a fashion as to afford the δ ring twist conformation of the chelate ring (SbO_2C_2). The minor component of the disorder in **3** features the flipped chair conformation of the cyclohexane ring, giving rise to the λ ring twist conformation of the chelate ring. The crystal structure of **3** ($P\bar{1}$) is

centrosymmetric, which ensures that both ring twist conformations are present in equal proportions. In contrast, the structures of **4** and **5** feature only one ring twist isomer each: **4**, prepared from 2*R*,3*R*-butanediol, crystallized as the λ isomer, while **5**, prepared from 1*S*,2*S*-cyclohexanediol, crystallized as the δ ring twist isomer (Figure 4.2). In the structures of **4** and **5**, the rings pucker in such a way as to allow the methyl groups to assume the less sterically encumbered equatorial positions on the cyclohexane ring. The same phenomenon is observed in the crystal structure of **6**, where the δ isomer is present, allowing the methyl group bound to C2 of the *S*-1,2-propanediolate to assume an equatorial position on the five-membered ring. Of note, only a diolate ligand with identical stereocenters (*i.e. R,R* or *S,S*) allows for both vicinal substituents on the five-membered ring to assume equatorial positions. For **2** and **3**, prepared from the *meso* diols, this necessitates that one substituent assumes an axial position and one assumes an equatorial position. These structural data indicate that the chiral diols afford a thermodynamic preference for a specific conformational isomer, however, the barrier to interconversion between the two ring twist isomers (λ and δ) is often low and they are most likely interconverting in solution.

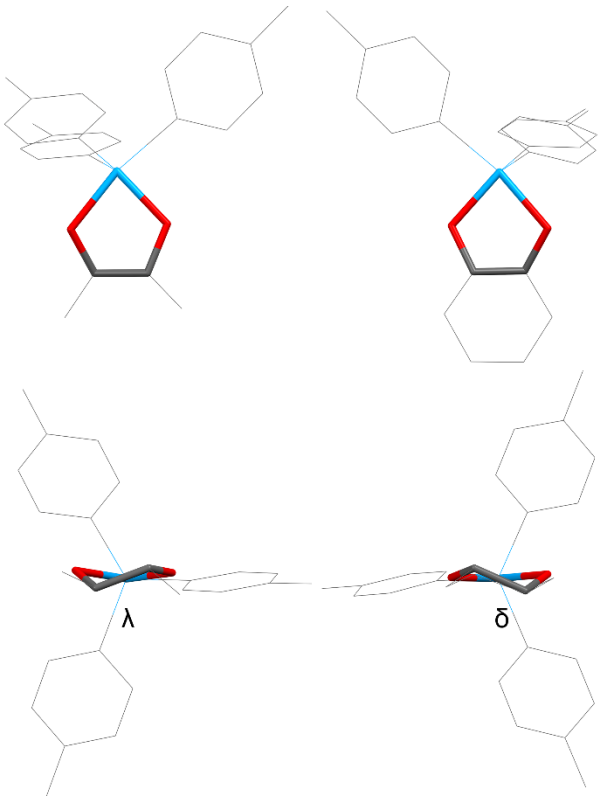

Figure 4.5. Crystallographically determined molecular structures of **4** (*left*) and **5** (*right*) shown with the five-membered chelate ring parallel (*top*) and perpendicular (*bottom*) to the page. The labels indicate the different ring conformations. The atoms forming the chelate ring are shown as sticks and all others as lines. Hydrogen atoms omitted for clarity. Color code: Sb teal, O red, C grey.

Compounds **1**-**6** possess Sb—O bond lengths ranging from 1.975(3) Å in **4** to 2.055(6) Å in **6** (Table 4.3). For all compounds, there is one shorter Sb—O bond of approximately 1.98 Å and a slightly, but statistically significantly, longer Sb—O bond between 2.02 and 2.05 Å in length. Compounds **2** and **3**, the two compounds prepared from *R*,*S*-diols, possess the smallest difference between the short and long Sb—O bond lengths as well as the overall longest of the "short" Sb—O bond lengths. Notably, these two compounds deviate the most strongly from trigonal bipyramidal geometries towards square pyramidal (Table 4.3). For the trigonal bipyramidal

compounds, the longer Sb—O bond is consistently identifiable as the axial, whereas the shorter is the equatorial. This is as expected, given the three-center-four-electron bonding expected along the trigonal bipyramidal axis.

NMR Spectroscopy

As described in chapter 3, pentasubstituted, pentavalent pnictogen compounds are frequently highly fluxional.[2, 12, 13] This often manifests in a coalescence of NMR signals at room temperature and above. Although the diols used to prepare compounds **1**-**5** all possess internal symmetries, we expect a lowering of symmetry for these diols once bound to the $Sb(tol)_3$ motif. This is evidenced in the crystallographically determined structures discussed above. This lowering of symmetry of the diols should give rise to two or more sets of peaks for the diolate in the ^1H NMR spectra, however, due to the fluxionality of these molecules we observe only one set of peaks for compounds **1**-**5**. For example, assuming that the geometries of **1**, **2**, and **4** are trigonal bipyramidal in solution, one would expect to see two distinct methyl resonances in the ^1H NMR spectrum of each: one for the methyl group(s) closest to the O atom that is bound axially, and one for the methyl group(s) closest to the O atom that is bound equatorially. For **2** and **4**, one would expect the methyl resonances to be further split by the backbone CH's, resulting in doublets. Instead, the ^1H NMR spectra of **2** and **4** each feature a single doublet integrating to 6H (all NMR studies were performed in $CDCl_3$). The spectrum of **1** similarly features a single ^1H methyl resonance and all three compounds feature a single methyl resonance in their ^{13}C NMR spectrum. These data clearly confirm that these

compounds are indeed fluxional on the NMR time scale, and that some form of polytopal rearrangement (likely related to the Berry pseudorotation) allows the methyl groups to exchange chemical environments. The NMR spectra of **3** and **5** are similarly devoid of the complexity expected of non-fluxional species. Due to the lack of symmetry in *S*-1,2-propanediol, used to prepare **6**, one would expect the same number of NMR signals regardless of whether it was fluxional. At this time, we have not been able to observe low-temperature decoalescence of any of the NMR signals for **1**-**6**.

With the ^{1}H and ^{13}C NMR spectra of the six model compounds in hand, we investigated if there were any spectroscopic signatures that we could use to distinguish the different types of metalloid-ligand interactions (Scheme 4.2). We began by analyzing the ^{13}C NMR spectra and focusing on the resonances of the C atoms bound directly to the coordinating O atoms. For **1**, prepared with pinacol, there is an upfield shift for this resonance, as compared to the corresponding resonance of pinacol. A similar upfield shift is observed for both of the Sb compounds derived from *R*,*S* diols (**2** and **3**). In contrast, the compounds derived from the *R*,*R*/*S*,*S* diols exhibited either a smaller upfield shift (**4**) or a marked downfield shift (**5**). We observed a similar distinction between **2**/**3** and **4**/**5** in the ^{1}H NMR resonances of the OC*H* nuclei of the diols and bound diolates (Figure C.3). For **2** and **3**, the OC*H* resonance shifts downfield upon binding to the Sb(V) center (Table 4.4). In contrast, there is an upfield shift in the OC*H* resonance for both **4** and **5** (Table 4.4).

Table 4.4.NMR spectroscopic signatures of metalloid-ligand interactions in **1**-**6**.[a]

	$\Delta(\delta^{13}C_{OC})$	$\Delta(\delta^{1}H_{OCH})$
1	–1.45	–
2	–2.27	+0.13
3	–1.50	+0.03
4	–0.28	–0.04
5	+1.62	–0.22
6 (CH)	–2.75	+0.03
6 (CH_2)	–0.72	+0.36, –0.19

[a] Changes in δ were calculated by subtracting the value of the bound ligand from that of the free diol.

Compound **6**, prepared from *S*-1,2-propanediol, provides an interesting comparator for compounds **1**-**5**. Since the propanediolate in **6** chelates through one primary alkoxide and one secondary alkoxide (whereas **1**-**5** chelate through two secondary alkoxides), there are two distinct ^{13}C NMR signals and three distinct ^{1}H NMR signals from the chelate ring (the OCH_2 unit exhibits diastereotopic splitting). For **6**, both ^{13}C resonances are shifted upfield once bound to the $Sb(tol)_3$ motif, but the O*C*H unit shifts by significantly more. In the ^{1}H NMR spectrum of **6**, the shifts are more variable, with the OC*H* signal shifting slightly downfield, while one of the OCH_2 signals shifts strongly upfield and the other shifts strongly downfield. The desymmetrized ligand in **6** gives us another advantage, that of the ability to obtain all of the coupling constants between the ligand proton resonances from a first-order spectral analysis (Figure C.4). Upon binding to Sb(V), the $^{3}J_{HH}$ value for the coupling of the OC*H* to one of the OCH_2 protons increases by 2 Hz whereas that for coupling to the other OCH_2 proton decreases by 0.4 Hz. These shifts are fully consistent with

those expected upon transitioning from a staggered antiperiplanar configuration in the free diol to a staggered *gauche* configuration in the complex (Figure C.4). The slight decrease of 0.4 Hz for one of the OCH_2 protons even suggests that the *gauche* configuration is not perfectly staggered and that the H–C–C–H dihedral angle for this interaction is slightly less than 60°. Indeed, analysis of the crystal structure of **6** affords H–C–C–H dihedral angles for this H atom of 49.5(9)° and 43.2(9)° for the two crystallographically independent molecules in the asymmetric unit.

4.3 Conclusion

The pentavalent antimonial drugs remain an important last line of defense against leishmaniasis, but important issues of toxicity and rising levels of Sb resistance in the causative parasites motivate further research into the fundamental chemistry and biology of these drugs. Due to a lack of information about these drugs molecular structures, there is a vast deficit in the community's understanding of the safety/activity of them. The structure of the carrier ligands used in the preparation of the drugs, being polyalcohols, suggests that chelating polyalkoxide motifs are likely present. Within this work, we have prepared a small molecular library containing small molecule models of Sb(V) complexes for each of the distinct classes of vicinal diolate environments possible in sodium stibogluconate and meglumine antimoniate. All three of the vicinal diolate environments are capable of forming stable chelate complexes as discussed above. With the NMR data acquired on these six model compounds, we have been able to establish spectroscopic signatures for each binding

environment. Compound **6** was most notably diagnostic due to the ability to track variation in $^{3}J_{HH}$ values following Sb(V) binding of a primary-secondary diol.

We wish to expand this study by synthesizing model compounds containing other possible binding modes for the pentavalent antimonials. Future work in the lab will focus on elucidating the possible binding modes of chelating triols to elucidate their spectroscopic signatures and provide more insight into the structures of the pentavalent antimonials. We attempted to synthesize triolate complexes using this framework by replacing one tolyl group and the diolate for glycerol, however it proved unsuccessful. We believe that Sb-triolate complexes can be made and future attempts will be attempted in the group. Glycerol was chosen as a simple triol as a proof of concept, however, similar to this work, the library of Sb-triolates could be expanded to better model *N*-methyl-D-glucamine and D-gluconic acid. Once in hand, these model compounds could provide spectroscopic signatures that could be used to help elucidate the components of the pentavalent antimonials.

4.4 Experimental Methods

General methods

All solvents and reagents were commercially available and used as received unless stated otherwise. $Sb(tol)_3$ and $Sb(tol)_3Br_2$ were prepared as previously described.[10, 14] Et_2O was dried using 3 Å molecular sieves. $CDCl_3$ was purchased from Cambridge Isotope Laboratories and used as received. ^{1}H and $^{13}C\{^{1}H\}$ NMR

spectra were recorded on a Bruker Avance III HD 500 MHz NMR spectrometer equipped with a multinuclear Smart Probe. Chemical shifts in the ^{1}H and $^{13}C\{^{1}H\}$ NMR spectra are reported in ppm as chemical shifts from tetramethylsilane and were referenced using the $CHCl_3$ (^{1}H, 7.26 ppm) and $CDCl_3$ (^{13}C, 77.0 ppm) solvent signals. *J* values are reported in Hz. Elemental analyses were performed by Micro-Analysis, Inc. (Wilmington, DE).

General synthesis of 1–6

$Sb(tol)_3Br_2$ (0.54 mmol) was dissolved in DCM (5 mL). A solution of the necessary diol (0.54 mmol) in DCM (2 mL) was added to the dihalostiborane solution. Et_3N (1.08 mmol) was added to the mixture. The reaction was stirred at room temperature for 1 h. The reaction was then dried under reduced pressure to yield a white solid. The product was then extracted with Et_2O (2 mL × 3). The Et_2O solution was then dried under reduced pressure to yield the crude product as a colorless oil. The oil was dissolved in MeCN (20 mL) and placed at −20 °C for 12 h. The product was collected as colorless crystals on a Hirsch funnel, washed with cold MeCN and dried under air.

Isolation of 1

Prepared with pinacol. Yield (227 mg, 82%). ^{1}H NMR (500 MHz, $CDCl_3$) δ = 7.55 (d, ^{3}J = 8.0 6H; Ar–H), 7.18 (d, ^{3}J = 7.6, 6H; Ar–H), 2.35 (s, 9H; CH_3), 1.17 ppm (s, 12H; CH_3); $^{13}C\{^{1}H\}$ NMR (126 MHz, $CDCl_3$) δ = 140.22, 136.95, 135.39,

129.52, 73.72, 25.85, 21.60 ppm; elemental analysis calcd (%) for $SbC_{27}H_{33}O_2$: C 63.42, H 6.51; found: C 63.15, H 6.59.

Isolation of 2

Prepared with 2*R*,3*S*-butanediol. Yield (210 mg, 81%). ^{1}H NMR (500 MHz, $CDCl_3$) δ = 7.57 (d, ^3J = 7.9, 6H; Ar–H), 7.21 (d, ^3J = 7.7, 6H; Ar–H), 3.92 (dt, ^3J = 5.6, ^3J = 5.2, 2H; CH), 2.37 (s, 9H; CH_3), 1.10 ppm (d, ^3J = 5.7, 6H; CH_3); ^{13}C{^{1}H} NMR (126 MHz, $CDCl_3$) δ = 140.50, 135.99, 135.17, 129.66, 68.61, 21.60, 18.20 ppm; elemental analysis calcd (%) for $SbC_{25}H_{29}O_2$: C 62.13, H 6.05; found: C 62.09, H 5.99.

Isolation of 3

Prepared with 1*R*,2*S*-cyclohexanediol. Yield (193 mg, 70%). ^{1}H NMR (500 MHz, $CDCl_3$) δ = 7.57 (d, ^3J = 8.0, 6H; Ar–H), 7.21 (d, ^3J = 7.7, 6H; Ar–H), 3.81 (m, 2H; CH), 2.36 (s, 9H; CH_3), 1.74 (m, 2H; CH_2), 1.68 (m, 2H; CH_2), 1.55 (m, 2H; CH_2), 1.27 ppm (m, 2H; CH_2); ^{13}C{^{1}H} NMR (126 MHz, $CDCl_3$) δ = 140.49, 136.09, 135.24, 129.68, 69.26, 32.29, 21.96, 21.61 ppm; elemental analysis calcd (%) for $SbC_{27}H_{31}O_2$: C 63.67, H 6.14; found: C 63.77, H 6.22.

Isolation of 4

Prepared with 2*R*,3*R*-butanediol. Yield (191 mg, 73%). ^{1}H NMR (500 MHz, $CDCl_3$) δ = 7.55 (d, ^3J = 8.0, 6H; Ar–H), 7.20 (d, ^3J = 7.6, 6H; Ar–H), 3.38 (m, 2H;

CH), 2.36 (s, 9H; CH_3), 1.20 ppm (d, ^3J = 5.6, 6H; CH_3); $^{13}C\{^1H\}$ NMR (126 MHz, CDCl3) δ = 140.50, 136.12, 135.22, 129.66, 72.13, 21.61, 21.13 ppm; elemental analysis calcd (%) for $SbC_{25}H_{29}O_2$: C 62.13, H 6.05; found: C 62.00, H 6.21.

Isolation of 5

Prepared with 1*S*,2*S*-cyclohexanediol. Yield (198 mg, 73%). ^1H NMR (500 MHz, $CDCl_3$) δ = 7.56 (d, ^3J = 8.0, 6H; Ar–H), 7.20 (d, ^3J = 7.7, 6H; Ar–H), 3.11 (m, 2H; CH), 2.36 (s, 9H; CH_3), 2.08 (m, 2H; CH_2), 1.70 (m, 2H; CH_2) 1.37 ppm (m, 4H; CH_2); $^{13}C\{^1H\}$ NMR (126 MHz, $CDCl_3$) δ = 140.58, 135.94, 135.35, 129.69, 77.23, 32.79, 25.37, 21.61 ppm; elemental analysis calcd (%) for $SbC_{27}H_{31}O_2$: C 63.67, H 6.14; found: C 63.44, H 5.99.

Isolation of 6

Prepared with *S*-1,2-propanediol. Yield (200 mg, 79%). ^1H NMR (500 MHz, $CDCl_3$) δ = 7.56 (d, ^3J = 8.0, 6H; Ar–H), 7.21 (d, ^3J = 7.7, 6H; Ar–H), 3.95 (dd, ^2J = 8.5, ^3J = 5.0, 1H; CH_2), 3.84 (dq, ^2J = 11.1, ^3J = 5.9, 1H; CH), 3.17 (dd, ^2J = 8.5, ^3J = 7.5 1H; CH_2), 2.36 (s, 9H; CH_3), 1.21 ppm (d, ^3J = 5.9, 3H; CH_3); $^{13}C\{^1H\}$ NMR (126 MHz, $CDCl_3$) δ = 140.66, 135.75, 135.21, 129.73, 67.14, 65.61, 21.61, 21.47 ppm; elemental analysis calcd (%) for $SbC_{24}H_{27}O_2$: C 61.43, H 5.80; found: C 61.73, H 5.73.

X-ray crystallography

Crystals of compounds **1–6** were grown as described above, crystals of $Sb(tol)_3$ were grown from a saturated EtOH solution at −20 °C over 12 h, and crystals of the decomposition product were grown from a saturated MeCN solution at −20 °C over 12 h. X-ray diffraction quality crystals of each were selected under a microscope, loaded onto a nylon fiber loop using Paratone-*n*, and mounted onto a Rigaku XtaLAB Synergy-S single crystal diffractometer. Each crystal was cooled to 100 K under a stream of nitrogen. Diffraction of Cu Kα radiation from a PhotonJet-S microfocus source was detected using a HyPix-6000HE hybrid photon counting detector. Screening, indexing, data collection, and data processing were performed with CrysAlisPro. The structures were solved using SHELXT and refined using SHELXL.[15, 16] All non-H atoms were refined anisotropically. H atoms were placed at geometrically calculated positions and refined with a riding model. The U_{iso} of the H atoms were set equal to 1.2(U_{eq}) of the C atom to which each is attached for CH_2 and aromatic CH units or 1.5(U_{eq}) for methyl groups.

4.5 References

1. Frézard, F.; Martins, P. S.; Barbosa, M. C. M.; Pimenta, A. M. C.; Ferreira, W. A.; de Melo, J. E.; Mangrum, J. B.; Demicheli, C., New insights into the chemical structure and composition of the pentavalent antimonial drugs, meglumine antimonate and sodium stibogluconate. *Journal of Inorganic Biochemistry* **2008,** *102* (4), 656-665.

2. Lindquist-Kleissler, B.; Weng, M.; Le Magueres, P.; George, G. N.; Johnstone, T. C., Geometry of Pentaphenylantimony in Solution: Support for a Trigonal Bipyramidal Assignment from X-ray Absorption Spectroscopy and Vibrational Spectroscopic Data. *Inorganic Chemistry* **2021,** *60* (12), 8566-8574.

3. Barucki, H.; Coles, S. J.; Costello, J. F.; Hursthouse, M. B., Synthesis and structure of organoantimony (V) cyclometallates: transannular interactions and the barrier to cyclisation. *Journal of Organometallic Chemistry* **2001,** *622* (1-2), 265-273.

4. Matsumura, Y.; Shindo, M.; Okawara, R., Preparation and properties of triorganoantimony thioglycolates and glycolates. *Journal of Organometallic Chemistry* **1971,** *27* (3), 357-363.

5. Stevani, C. V.; Baader, W. J., Preparation and Characterisation of 2,2,2-Triphenyl-2λ5-1,3,2-Dioxastibolane-4,5-Dione as Standard For an Attempt to Trap 1,2-Dioxetanedione, A Possible High-Energy Intermediate in Peroxyoxalate Chemiluminescence. *Journal of Chemical Research* **2002,** *2002* (9), 430-432.

6. Baumstark, A. L.; Landis, M. E.; Brooks, P. J., Insertion reaction of triphenylarsine and triphenylantimony with tetramethyl-1,2-dioxetane: preparation of 2,2-dihydro-4,4,5,5-tetramethyl-2,2,2-triphenyl-1,3,2-dioxarsolane and -dioxastibolane. *Journal of Organic Chemistry* **1979,** *44* (24), 4251-4253.

7. Sharutin, V. V.; Sharutina, O. K.; Shalabanova, N. A., Syntheses and Structures of the Hexacoordinated Antimony Complexes: Ph3(C2H4O2)Sb···DMSO, (3-FC6H4)3(C2H4O2)Sb···DMSO, and (4-MeC6H4)3(C6H4O2)Sb···DMSO. *Russ. Journal of Coordination Chemistry* **2019,** *44* (12), 765-771.

8. Holmes, R. R.; Day, R. O.; Chandrasekhar, V.; Holmes, J. M., Pentacoordinated molecules. 68. Distortion coordinate for nonrigid five-coordinated antimony. Synthesis and structure of oxygen- and sulfur-containing cyclic organostiboranes. *Inorganic Chemistry* **1987,** *26* (1), 163-168.

9. Poddel'sky, A. I.; Fukin, G. K.; Baranov, E. V., Triphenylantimony(V) Complexes Based on o-Aminophenols with the Ambivalent N-Aryl Group. *Russ. Journal of Coordination Chemistry* **2022,** *48* (12), 902-908.

10. Shen, K.-W.; McEwen, W. E.; La Placa, S. J.; Hamilton, W. C.; Wolf, A. P., Crystal and molecular structures of methoxytetraphenylantimony and dimethoxytriphenylantimony. *Journal of the American Chemical Society* **1968,** *90* (7), 1718-1723.

11. Addison, A. W.; Rao, T. N.; Reedijk, J.; van Rijn, J.; Verschoor, G. C., Synthesis, structure, and spectroscopic properties of copper(II) compounds containing nitrogen–sulphur donor ligands; the crystal and molecular structure of aqua[1,7-bis(N-methylbenzimidazol-2′-yl)-2,6-dithiaheptane]copper(II) perchlorate. *Dalton Transactions* **1984,** (7), 1349-1356.

12. Muetterties, E. L.; Mahler, W.; Schmutzler, R., Stereochemistry of Phosphorus(V) Fluorides. *Inorganic Chemistry* **1963,** *2* (3), 613-618.

13. Muetterties, E. L.; Mahler, W.; Packer, K. J.; Schmutzler, R., Five-Coordinate Stereochemistry. *Inorganic Chemistry* **1964,** *3* (9), 1298-1303.

14. Brabant, C.; Hubert, J.; Beauchamp, A. L., The Crystal and Molecular Structure of Penta-*P*-tolylantimony, (p-$CH_3C_6H_4)_5Sb$. *Canadian Journal of Chemistry* **1973,** *51* (17), 2952-2957.

15. Sheldrick, G. M., *SHELXT* - Integrated space-group and crystal-structure determination. *Acta Crystallographica, Section A* **2015,** *71*, 3-8.

16. Sheldrick, G. M., Crystal structure refinement with *SHELXL*. *Acta crystallographica, Section C* **2015,** *71*, 3-8.

Chapter 5

Investigations on the Crystal Structures of $Sb(Ar)_3(O_2R)$ Model Compounds

5.1 Introduction

Our previous work, discussed at length in Chapter 4, left us interested in how the $Sb(tol)_3(O_2R)$ compounds crystallized. Specifically, we wanted to achieve a deeper understanding of how the stereochemistry of the diolate ligands might influence the space groups that these compounds crystallize in. In the work presented in Chapter 4, we synthesized compounds **1**-**6**, all of which contained a diolate ligand bound to an $Sb(tol)_3$ fragment. Curiously, we noticed that the crystals of **4**, **5**, and **6** all feature two crystallographically independent molecules in the asymmetric unit, and in each crystal structure, the two molecules are related by a pseudoinversion center. For all three crystal structures, the pseudosymmetry is observed by the Sb atom and aryl rings, but not the enantiomerically pure diolate ligand. This led us to wonder: if the two enantiomers of a specific diolate were crystallized together, would that pseudoinversion center be replaced by a true inversion center? To test this, we prepared the enantiomer of **4** with 2*S*,3*S*-butandeiol to get compound **7**. Compounds **4** and **7** were then used to make the racemate **10**. We further tested our hypothesis by preparing analogs of **4** and **7** by replacing the $Sb(tol)_3$ framework with the bulkier $Sb(m\text{-xyl})_3$ fragment to get **8** and **9**. Compounds **8** and **9** were then used to make the racemate **11** (Scheme 5.2).

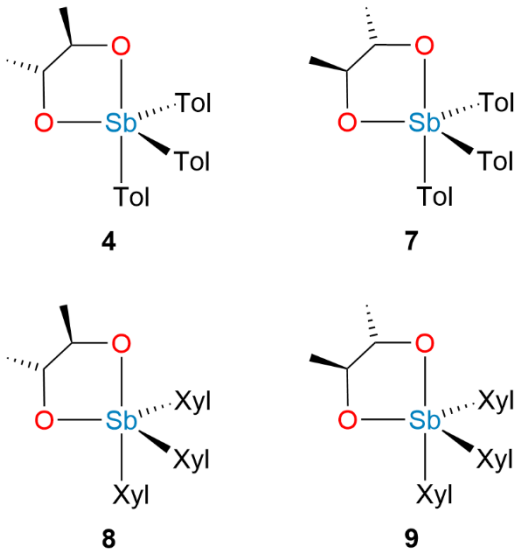

Scheme 5.1. Structures of compounds **4** and **7-9**.

5.2 Results and Discussion

Synthesis

Synthesis of **4** and **7-9** was done as depicted in Scheme 5.2, the same synthetic approach used in Chapter 4. The synthesis of $Sb(tol)_3Br_2$ was done as previously described.[1] The synthesis of $Sb(m\text{-xyl})_3Br_2$ was done in the same fashion. Compounds **4** and **7** were synthesized by stirring an equimolar mixture of $Sb(tol)_3Br_2$ and either 2*R*,3*R*-butanediol (**4**) or 2*S*,3*S*-butanediol (**7**) at room temperature in DCM with 2 equiv Et_3N for 1 h. Compounds **8** and **9** were synthesized in the same fashion, substituting $Sb(m\text{-xyl})_3Br_2$ for $Sb(tol)_3Br_2$. Compound **8** was prepared with 2*R*,3*R*-butandeiol and **9** with 2*S*,3*S*-butanediol. The DCM was then removed to yield a mixture of the target compound and $(Et_3NH)Br$. The Sb(V) compound was extracted with Et_2O and recrystallized from MeCN at —20 °C to yield colorless crystals.

Compound **10** was synthesized by dissolving equimolar amounts of **7** and **8** in MeCN and recrystallizing the racemate at —20 °C, yielding colorless crystals. Compound **11** was synthesized in the same way, replacing **4** and **7** for **8** and **9**.

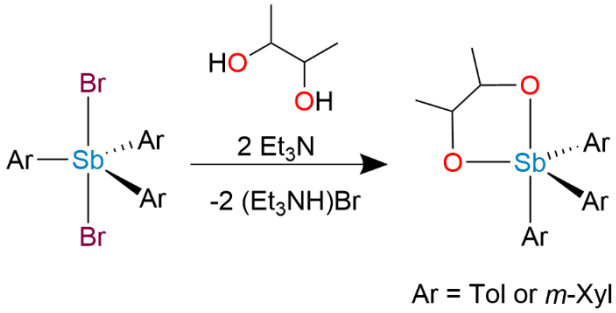

Scheme 5.2. Synthesis of **4** and **7-9**.

Compound **4**, prepared with 2*R*,3*R*-butanediol, was already on hand from our previous work in Chapter 4 and helped inspire this study. Compound **7**, prepared with 2*S*,3*S*-butanediol, is the enantiomer of **4** and served to test our premise: crystallizing the two enantiomers together would yield a crystal structure where the pseudoinversion center present in **4** would be replaced by a true inversion center, giving us the expected space group (Figure 5.1). Compounds **8** and **9**, prepared with 2*R*,3*R*-butanediol and 2*S*,3*S*-butanediol respectively, served to test the robustness of our theory due to it containing the same diolate ligands with the same stereochemistry (as in **4** and **7**) but with the $Sb(tol)_3$ fragment replaced for a $Sb(m\text{-xyl})_3$ fragment. Compound **10** is the racemate of **4** and **7**. Finally, **11** is the racemate of **8** and **9**.

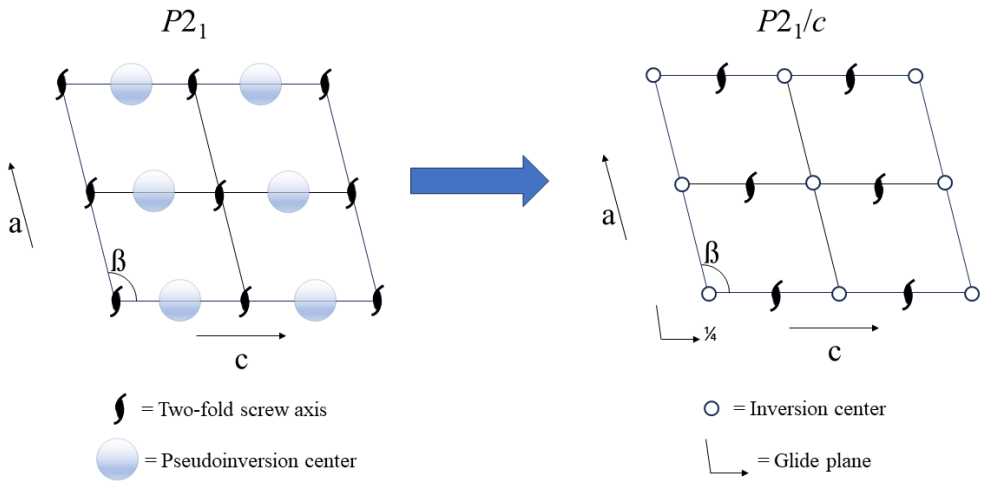

Figure 5.1. Space group diagrams of $P2_1$ and $P2_1/c$ showing the position of the pseudoinversion center present in the crystal structures of **4** and **7**.

X-Ray Crystallography

The structures of all six compounds were unambiguously confirmed crystallographically (Figure 5.2, Table 5.1, and Table 5.2). Crystals suitable for X-ray diffraction analysis were grown from saturated MeCN solutions at —20 ℃ for all six compounds. In Chapter 4, crystals of **4** obtained from slow evaporation of $CDCl_3$ crystallized in the Sohncke space group *C*2. The Sohncke space groups are space groups that only contain symmetry operations of the first kind (rotations, screw rotations, and translations). Enantiomerically pure molecules cannot crystallize in non-Sohncke space groups because all they contain symmetry operations of the second kind, those that invert handedness. Compounds **4**, **7**, **8**, and **9** cannot possess symmetry of any other kind due to the enantiomerically pure diolate ligands used in

their preparation, and therefore are expected to crystallize in a Sohncke space group. When grown from a saturated MeCN solution at —20 °C, **4** crystallized in the Sohncke space group $P2_1$. Determination of the correct space group was achieved by determining the Laue symmetry, the presence of systematic absences, and the $<E^2\text{-}1>$ statistic. The Laue symmetry was determined based on the symmetries present in the diffraction pattern. The diffraction pattern was determined to contain 2-fold symmetry that, in combination with the centrosymmetry inherent to all diffraction patterns, affords the Laue symmetry of 2/*m*. Certain lattice centering and symmetry operations with translational components cause some reflections to have exactly zero intensity in the diffraction pattern, these are known as systematic absences. For **4** and **7**, all reflections where *h* is 0, *l* is 0, and *k* is odd, are missing, indicating that there is a 2_1 screw axis parallel to *b* present. The lack of any other systematically absent reflections rules out the possibility of glides and lattice centering. With the above information, the only two space groups possible for **4** and **7** are $P2_1$ or $P2_1/m$, where the main difference between the two is the presence of inversion symmetry in $P2_1/m$, which $P2_1$ lacks. The $<E^2\text{-}1>$ statistic is used to determine if a crystal is centrosymmetric (contains inversion symmetry) or non-centrosymmetric (lacks inversion symmetry). Although all diffraction patterns are centrosymmetric, the $<E^2\text{-}1>$ statistic measures the "clumpiness" of a diffraction pattern by measuring the distribution of the intensity of reflections present in the diffraction pattern. The intensity of a reflection is related to the structure factors (*F*), which are then normalized via squaring, giving us E^2. An $<E^2\text{-}1>$ value close to 0.736 suggests that a

structure is non-centrosymmetric and a value closer to 0.968 suggests that it is centrosymmetric. Interestingly, the $<E^2-1>$ statistics for both **4** and **7**, 0.932 and 0.929 respectively, suggest that both these structures are centrosymmetric. However, due to the enantiomerically pure diols used in the preparation of **4** and **7**, they cannot crystallize in a centrosymmetric space group, giving us the correct space group as $P2_1$.

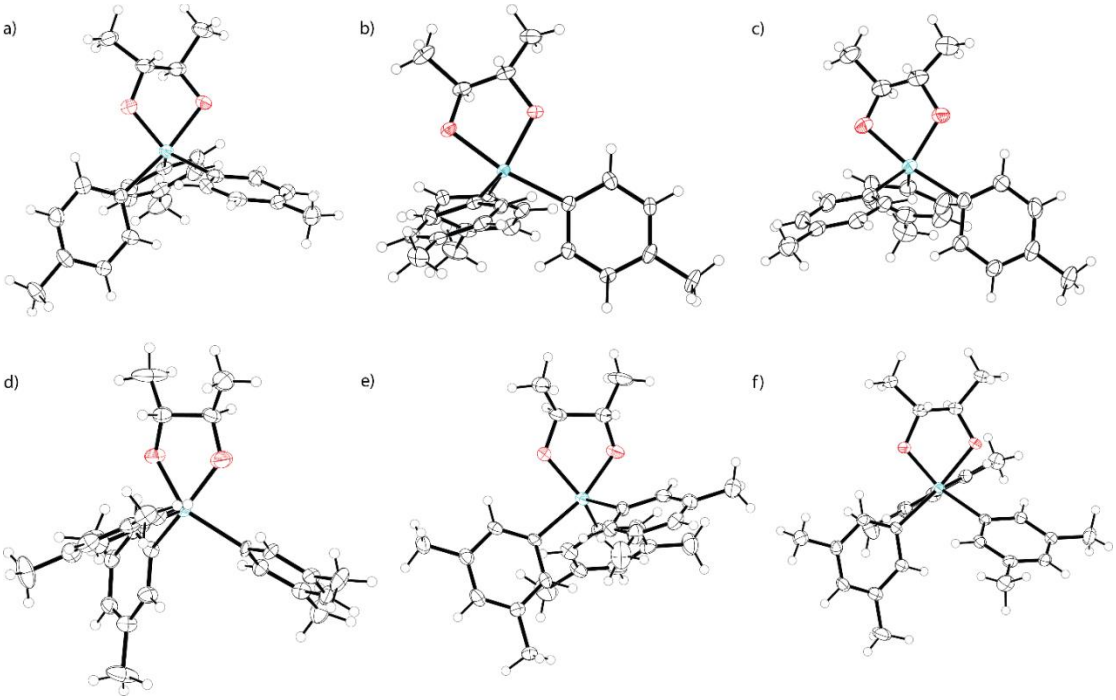

Figure 5.2. Thermal ellipsoid plots (50% probability) of **4** and **7-11** (a-f). Color code: Sb teal, O red, C black, H white spheres of arbitrary radius. For crystals with $Z' > 1$ (a, b, d, and e), only one of the molecules in the asymmetric unit is shown.

Compounds **7-9**, all crystallized in Sohncke space groups as well, as expected due to the enantiomerically pure diols used in their preparation. Crystals of **4**, **7**, **8**, and **9** all feature two crystallographically independent molecules in the asymmetric

unit. For each structure the two crystallographically independent molecules are related by a pseudoinversion center. In all four crystal structures, the Sb atom and the aryl rings observe the pseudosymmetry, but the enantiomerically pure diolate ligand does not. This is all consistent with what we observed and expected from the work in Chapter 4. The Flack parameter is used to describe the absolute structure of a non-centrosymmetric crystal and, if the crystal is comprised of an enantiomerically pure chiral molecule, the absolute configuration of that molecule. This allows one to determine the handedness of a molecule in the crystal structure (i.e., if a stereocenter is *R* or *S*). A Flack parameter of 0 means that the refined model possesses the correct stereochemistry, while a Flack parameter of 1 means that the model needs to be inverted. Any non-integer Flack parameter means there is a combination of both stereoisomers. The Flack parameters for **4**, **7**, **8** and **9** do not deviate from 0 within 3σ, consistent with our proposal that these pseudoinversion centers are not missed, true crystallographic symmetries. In the crystal structures of **4** and **7**, the pseudoinversion center lies at approximately (0.50, 0.50, 0.75); a true inversion center at these same coordinates would afford the space group $P2_1/c$ (Figure 5.1). This led us to believe that the crystal structure of the racemate of **4** and **7** would crystallize in $P2_1/c$. Interestingly, the racemate, compound **10**, crystallized in the space group $P\bar{1}$. In the crystal structures of **8** and **9**, the pseudoinversion center lies at approximately (0.49, 0.50, 0.50) and (0.51, 0.50, 0.50) respectively; a true inversion center at (0.50, 0.50, 0.50) would afford the space group $P\bar{1}$. The racemate of **8** and **9**, compound **11**,

crystallized in the space group $P\bar{1}$, as expected based on the crystal structures of **8** and **9**.

Table 5.1. Refinement details for the crystal structures of compounds **4**, **7**, and **10**.

	4	**7**	**10**
Formula	$C_{25}H_{29}O_2Sb$	$C_{25}H_{29}O_2Sb$	$C_{25}H_{29}O_2Sb$
FW	483.23	483.23	483.23
T (K)	101(3)	107(2)	103(4)
λ (Å)	1.54184	1.54184	1.54184
Crystal System	Monoclinic	Monoclinic	Triclinic
Space group	$P2_1$	$P2_1$	$P\bar{1}$
a (Å)	8.70780(10)	8.70850(10)	8.6690(3)
b (Å)	15.4287(2)	15.44630(10)	9.2367(3)
c (Å)	16.6758(2)	16.6628(2)	14.2286(5)
α (°)			78.914(2)
β (°)	101.2980(10)	101.2130(10)	84.766(3)
γ (°)			78.770(2)
Volume (Å^3)	2196.98(5)	2198.60(4)	1094.95(7)
Z	4	4	2
ρ_{calc} (Mg/m^3)	1.461	1.460	1.466
Size (mm^3)	0.19×0.11×0.07	0.27×0.23×0.08	0.1×0.08×0.05
θ range (°)	2.702-68.239	3.938-68.251	3.170-68.251
Total data	65745	34974	27622
Unique data	8050	7888	4012
Parameters	516	516	258
Completeness	100.0%	99.8%	99.9%
R_{int}	5.95%	4.36%	6.44%
R_1 (I > 2σ)	2.63%	3.54%	3.42%
R_1 (all data)	2.80%	3.61%	3.59%
wR_2 (I > 2σ)	7.36%	9.39%	8.03%
wR_2 (all data)	7.48%	9.46%	8.14%
S	1.059	1.072	1.038
Flack *x*	0.002(9)	0.014(8)	—

Table 5.2. Refinement details for the crystal structures of compounds **8**, **9**, and **11**.

	8	**9**	**11**
Formula	$C_{28}H_{35}O_2Sb$	$C_{28}H_{35}O_2Sb$	$C_{28}H_{35}O_2Sb$
FW	525.31	525.31	525.31
T (K)	105(7)	107(4)	108(4)
λ (Å)	1.54184	1.54184	1.54184
Crystal System	Triclinic	Triclinic	Triclinic
Space group	*P*1	*P*1	$P\bar{1}$
a (Å)	9.6092(2)	9.60900(10)	9.6369(2)
b (Å)	10.6217(3)	10.6249(2)	10.4594(2)
c (Å)	13.0406(2)	13.02660(10)	13.0831(3)
α (°)	102.494(2)	102.4910(10)	102.195(2)
β (°)	91.5870(10)	91.6280(10)	92.245(2)
γ (°)	99.425(2)	99.3620(10)	99.022(2)
Volume (Å^3)	1279.18(5)	1278.38(3)	1269.45(5)
Z	2	2	2
ρ_{calc} (Mg/m^3)	1.364	1.365	1.374
Size (mm^3)	0.07×0.05×0.03	0.16×0.07×0.06	0.31×0.27×0.21
θ range (°)	3.479-68.238	3.483-68.246	3.466-68.222
Total data	34763	35972	34433
Unique data	8873	8843	4650
Parameters	576	576	288
Completeness	100.0%	99.9%	99.9%
R_{int}	5.55%	5.58%	4.52%
R_1 (I > 2σ)	3.03%	3.38%	2.51%
R_1 (all data)	3.30%	3.55%	2.52%
wR_2 (I > 2σ)	7.41%	8.80%	6.47%
wR_2 (all data)	7.54%	8.94%	6.48%
S	1.066	1.075	1.068
Flack *x*	-0.001(15)	-0.008(14)	—

We would like to note a problem that we consistently ran into while trying to collect X-ray diffraction data on these compounds was large residual electron density

near the Sb atom and along the Sb—O bonds. We would often observe residual electron density maxima greater than 4.5 e $Å^{-3}$. Suspecting that this could be an issue due to the strong absorption of the 1.54 Å wavelength Cu Kα radiation that we used, we also collected data from a crystal of **7** using Mo Kα radiation in hopes that the shorter wavelength (0.71 Å) would eliminate this artefact, however the large residual electron density remained. In the course of screening multiple crystals, I observed a trend whereby relatively large crystals (> 0.15 x 0.15 x 0.05 mm^3) minimized the residual electron density observed. Whether eliminating this residual electron density was due to the shorter collection times required for larger crystals, or simply due to better crystal quality, we are unsure.

It is interesting that our hypothesis concerning how the racemates of **4**/**7** and **8**/**9** would crystallize was correct in one instance, the racemate of **8**/**9** (**11**), but incorrect for the racemate of **4**/**7** (**10**). Compound **11** crystallized in the expected space group $P\bar{1}$, based on **8** and **9** crystallizing in *P*1. However, based on **4** and **7** crystallizing in $P2_1$, we expected it to crystallize in $P2_1/c$ due to the pseudoinversion center in **4** and **7** being replaced by a true inversion center once both enantiomers were present in **10**. We are unsure of why one set of compounds was observed to crystallize in the expected manner, while the other did not, but it could likely be due to the different aryl groups employed. Compounds **4** and **7** contained tolyl substituents while **8** and **9** contained the bulkier *m*-xylyl substituents. It is possible that the bulkier *m*-xylyl substituents influence packing more than those of the tolyl substituents, which is why the unit cell of **11** is roughly the same size as the unit cells

of **8** and **9**; while the unit cell of **10** is slightly smaller than the unit cells of **4** and **7**. Interestingly, the molecules in the crystal structure of **11** are no longer oriented in the same way as those in the crystal structures of **8** and **9** (Figure 5.3). Inspection of the crystal structure of **10** shows that instead of two tolyl groups (one from each enantiomer) overlapping each other, as is the case in the structures of **4**, **7**, **8**, and **9**, the two diolate substituents are overlapping (Figure 5.4).

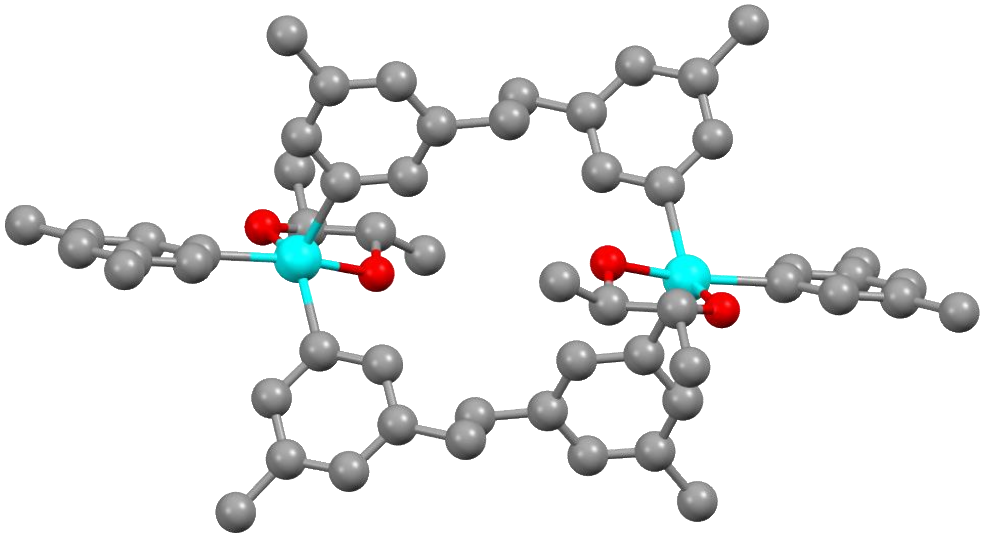

Figure 5.3. Ball-and-stick representation of both isomers in the crystal structure of **11**.

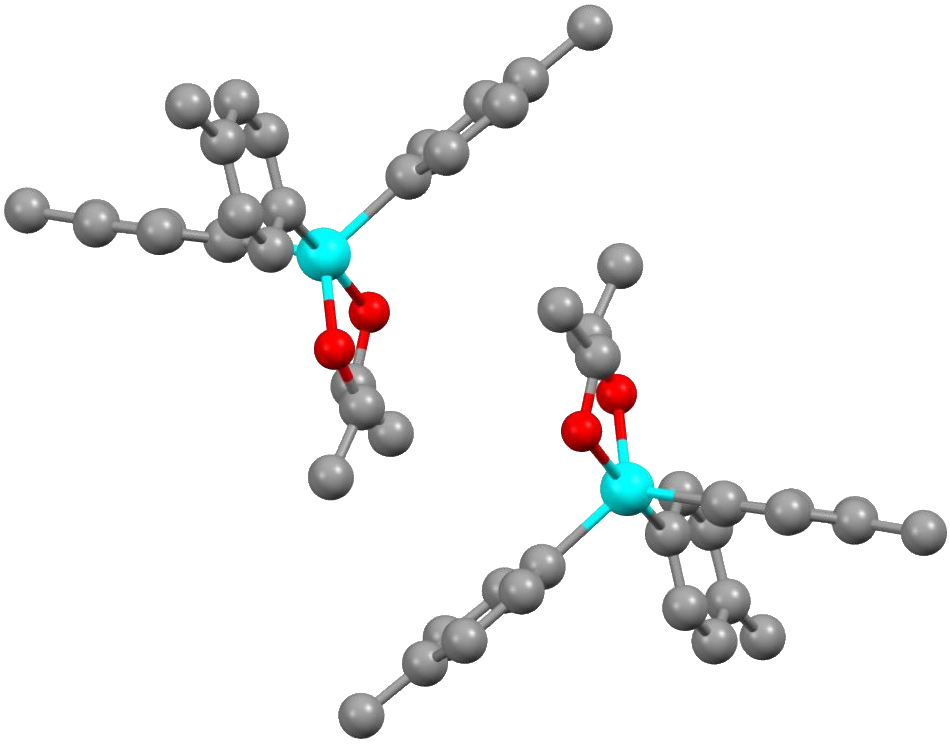

Figure 5.4. Ball-and-stick representation of both isomers in the crystal structure of **10**.

Geometry

As discussed in previous chapters, VSEPR theory predicts that the most stable geometry for a pentasubstituted, pentavalent (σ^5,λ^5) metal/metalloid compound is trigonal bipyramidal (D_{3h}), while square pyramidal is another common geometry for these types of molecules. The τ parameter, also discussed in previous chapters, is a measure of how square pyramidal or trigonal bipyramidal a molecule is. For compound **4**, the τ parameter stayed relatively consistent from the *C*2 structure in Chapter 4 (τ = 0.75) to the $P2_1$ (τ = 0.79) structure presented in this chapter (Table

5.3). In the crystal structures of **4** and **7,** both have relatively high τ values which represent the approximate trigonal bipyramidal geometry of the tolyl-containing compounds. The two crystallographically independent molecules in each of these crystal structures both have high τ values, above 0.76 for all four molecules. This is in contrast to the geometries present in the crystal structures of **8** and **9**. For both compounds, one molecule in the crystal structures of each has a higher τ value (> 0.54) closer to a trigonal bipyramidal geometry; while the other molecule in each crystal structure has a lower τ value (< 0.27). These interesting observations are most likely a result of crystal packing forces. Once racemized, we see these τ values stay relatively consistent with the τ values present in the enantiomers that makeup the racemate. In the crystal structure of **10**, the racemate of **4** and **7**, the τ value is 0.74; whereas the τ value in the crystal structure of **11**, the racemate of **8** and **9**, the τ value is 0.46. These observations show the evident difference in the packing of these molecules, most likely a result of the increase steric bulk of the *m*-xylyl groups present in **8** and **9**.

Table 5.3. Crystallographically determined bond metrics for **4** and **7-11**.

	τ^b	Sb–O (Å)
4[a]	0.79	1.964(4), 2.031(5) / 1.976(4), 2.033(4)
7[a]	0.78	1.974(3), 2.029(4) / 1.968(3), 2.024(5)
8[a]	0.41	1.978(8), 2.007(9) / 1.988(8), 2.043(8)
9[a]	0.40	1.978(7), 2.030(7) / 1.981(7), 2.008(8)
10	0.74	1.974(3), 2.031(3)
11	0.46	1.9882(17), 2.0194(17)

[a] Sb–O values provided for both crystallographically independent molecules in the asymmetric unit.
[b] Average values provided in instances of disorder or multiple crystallographically independent molecules

Compounds **4** and **7-11** possess Sb—O bond lengths ranging from 1.964(4) Å in **4** to 2.043(8) Å in **8** (Table 5.3). Similar to what was observed in the crystal structures presented in Chapter 4, each compound has a significantly shorter Sb—O bond between 1.96 Å and 1.99 Å and a slightly, but statistically significantly, longer Sb—O bond between 2.0 and 2.04 Å in length. For the trigonal bipyramidal molecules **4**, **7** and **10**, the longer Sb—O bond is consistently the axial. This is consistent with the three-center-four-electron bonding present in these molecules and discussed in Chapter 1.

5.3 Conclusions

This work, although not directly related to our interest in the pentavalent antimonials used to treat leishmaniasis, serves to further our understanding of the

structures of pentasubstituted, pentavalent antimony-containing complexes. The similarities in bonding and geometry between the compounds in this work and the compounds presented in Chapter 4 further confirms the robust nature of the interactions of vicinal diolate ligands and antimony. These consistencies, along with the difficulties of installing a triolate ligand on the $Sb(Ar)_3$ framework (Chapter 4) further support our hypothesis that binding of a vicinal diol is likely present in the structures of the pentavalent antimonials.

5.4 Experimental Methods

General methods

All solvents and reagents were commercially available and used as received unless stated otherwise. $Sb(tol)_3$ and $Sb(tol)_3Br_2$ were prepared as previously described.[1, 2] Et_2O was dried using 3-Å molecular sieves. $CDCl_3$ was purchased from Cambridge Isotope Laboratories and used as received. ^1H and $^{13}C\{^1H\}$ NMR spectra were recorded on a Bruker Avance III HD 500 MHz NMR spectrometer equipped with a multinuclear Smart Probe. Chemical shifts in the ^1H and $^{13}C\{^1H\}$ NMR spectra are reported in ppm as chemical shifts from tetramethylsilane and were referenced using the $CHCl_3$ (^1H, 7.26 ppm) and $CDCl_3$ (^{13}C, 77.0 ppm) solvent signals. *J* values are reported in Hz. Elemental analyses were performed by Micro-Analysis, Inc (Wilmington, DE) and Midwest Microlabs (Indianapolis, IN).

General Synthesis of 4, 7, 8, 9

$Sb(tol)_3Br_2$ (**4**/**7**) or $Sb(xyl)_3Br_2$ (**8**/**9**) (0.54 mmol) was dissolved in DCM (5 mL). A solution of the necessary diol (0.54 mmol) in DCM (2 mL) was added to the dihalostiborane solution. Et_3N (1.08 mmol) was added to the mixture. The reaction was stirred at room temperature for 1 h. The reaction was then dried under reduced pressure to yield a white solid. The product was then extracted with Et_2O (2 mL × 3). The Et_2O solution was then dried under reduced pressure to yield the crude product as a colorless oil. The oil was dissolved in MeCN (20 mL) and placed at –20 °C for 12 h. The product was collected as colorless crystals on a Hirsch funnel, washed with cold MeCN and dried under air.

Isolation of 4

Prepared with 2*R*,3*R*-butanediol. Yield (191 mg, 73%). ^{1}H NMR (500 MHz, $CDCl_3$) δ=7.55 (d, ^3J= 8.0, 6H; Ar-H), 7.20 (d, ^3J= 7.6, 6H; Ar-H), 3.38 (m, 2H; CH), 2.36 (s, 9H; CH_3), 1.20 ppm (d, ^3J= 5.6, 6H; CH_3); $^{13}C\{^1H\}$ NMR (126 MHz, $CDCl_3$) δ=140.50, 136.12, 135.22, 129.66, 72.13, 21.61, 21.13 ppm; elemental analysis calcd (%) for $SbC_{25}H_{29}O_2$: C 62.13, H 6.05; found: C 62.00, H 6.21.

Isolation of 7

Prepared with 2*S*,3*S*-butanediol. Yield (155 mg, 60%). ^{1}H NMR (500 MHz, $CDCl_3$) δ=7.55 (d, ^3J= 8.0, 6H; Ar-H), 7.20 (d, ^3J= 7.7, 6H; Ar-H), 3.38 (m, 2H; CH), 2.36 (s, 9H; CH_3), 1.20 ppm (d, ^3J= 5.6, 6H; CH_3); $^{13}C\{^1H\}$ NMR (126 MHz, $CDCl_3$)

δ=140.51, 136.12, 135.23, 129.67, 72.14, 21.61, 21.13 ppm; elemental analysis calcd (%) for $SbC_{25}H_{29}O_2$: C 62.13, H 6.05; found: C 62.23, H 6.06.

Isolation of 8

Prepared with 2*R*,3*R*-butanediol. Yield (132 mg, 50%). ^{1}H NMR (500 MHz, $CDCl_3$) δ=7.26 (s, 6H; Ar-H), 7.04 (s, 3H; Ar-H), 3.40 (m, 2H; CH), 2.28 (s, 18H; CH_3), 1.22 ppm (d, ^3J = 5.6, 6H; CH_3). $^{13}C\{^1H\}$ NMR (126 MHz, $CDCl_3$) δ=139.29, 138.19, 132.72, 132.18, 72.14, 21.60, 21.17 ppm; elemental analysis calcd (%) for $SbC_{28}H_{35}O_2$: C 64.02, H 6.72; found: C 64.07, H 6.73.

Isolation of 9

Prepared with 2*S*,3*S*-butanediol. Yield (147 mg, 56%). ^{1}H NMR (500 MHz, $CDCl_3$) δ=7.26 (s, 6H; Ar-H), 7.04 (s, 3H; Ar-H), 3.40 (m, 2H; CH), 2.28 (s, 18H; CH_3), 1.22 ppm (d, ^3J = 5.6, 6H; CH_3). $^{13}C\{^1H\}$ NMR (126 MHz, $CDCl_3$) δ=139.29, 138.19, 132.72, 132.18, 72.14, 21.60, 21.17 ppm; elemental analysis calcd (%) for $SbC_{28}H_{35}O_2$: C 64.02, H 6.72; found: C 64.08, H 6.71.

Crystallization of 10

Compounds **4** (0.03 mmol) and **7** (0.03 mmol) were mixed and dissolved in MeCN (5 mL) and placed at –20 °C for 12 h. The product was collected as colorless crystals on a Hirsch funnel, washed with cold MeCN and dried under air.

Crystallization of 11

Compounds **8** (0.03 mmol) and **9** (0.03 mmol) were mixed and dissolved in MeCN (10 mL) and placed at –20 °C for 12 h. The product was collected as colorless crystals on a Hirsch funnel, washed with cold MeCN and dried under air.

X-ray crystallography

Crystals of compounds **4** and **7-11** were grown as described above. X-ray diffraction quality crystals of each were selected under a microscope, loaded onto a MiTeGen polyimide loop using Paratone-*n*, and mounted onto a Rigaku XtaLAB Synergy-S single crystal diffractometer. Each crystal was cooled to 100 K under a stream of nitrogen. Diffraction of Cu Kα radiation from a PhotonJet-S microfocus source was detected using a HyPix-6000HE hybrid photon counting detector. Screening, indexing, data collection, and data processing were performed with CrysAlisPro. The structures were solved using SHELXT and refined using SHELXL.[3, 4] All non-H atoms were refined anisotropically. H atoms were placed at geometrically calculated positions and refined with a riding model. The U_{iso} of the H atoms were set equal to 1.2(U_{eq}) of the C atom to which each is attached for CH_2 and aromatic CH units or 1.5(U_{eq}) for methyl groups.

5.5 References

1. Shen, K.-W.; McEwen, W. E.; La Placa, S. J.; Hamilton, W. C.; Wolf, A. P., Crystal and molecular structures of methoxytetraphenylantimony and dimethoxytriphenylantimony. *Journal of the American Chemical Society* **1968,** *90* (7), 1718-1723.

2. Brabant, C.; Hubert, J.; Beauchamp, A. L., The Crystal and Molecular Structure of Penta-*P*-tolylantimony, (*p*-$CH_3C_6H_4)_5Sb$. *Canadian Journal of Chemistry* **1973,** *51* (17), 2952-2957.

3. Sheldrick, G. M., *SHELXT* - Integrated space-group and crystal-structure determination. *Acta Crystallographica, Section A* **2015,** *71*, 3-8.

4. Sheldrick, G. M., Crystal structure refinement with *SHELXL*. *Acta crystallographica, Section C* **2015,** *71*, 3-8.

Appendix A: Supplementary Experimental Data for Chapter 2

Published in part in: Lindquist-Kleissler, B.; Johnstone, T. C. *Inorg. Chem.*, **2021,** *60*, 1846.

Table A.1. Comparison of computationally and experimentally determined geometric parameters for O—E compounds under investigation.

Compound	Experimental O–E Bond Length (Å)	Method and Reference	MP2/def2-QZVPP Calculated O–E Bond Length (Å)	PBE0/def2-TZVPP Calculated O–E Bond Length (Å)
NO^+	1.062(4)	X-ray crystallography[1] IF_5 cocrystal of NO_3^- salt	1.079	1.054
	1.063250(24)	Photoelectron spectroscopy[2] (r_e)		
PO^+	1.4249927(4)	Microwave spectroscopy[3] (r_e)	1.445	1.420
	1.419(5)	Photoelectron spectroscopy[4] (r_e)		
AsO^+	1.568*	UV spectroscopy[5] (r_e)	1.589	1.557
SbO^+	1.8074*	UV spectroscopy[6] (r_e)	1.795	1.752
HNO	1.211(6)	Microwave spectroscopy[7] (r_0)	1.217	1.190
	1.20880(2)	Millimeterwave spectroscopy[8] ($r_m^{(1)}$)		
HPO	1.4801(1)	Laser-induced fluorescence[9] (r_e)	1.493	1.478
	1.4800(9)	Microwave spectroscopy[10] (r_e)		

HAsO	1.6342(5)	Laser-induced fluorescence[11] (r_0)	1.641	1.622
	1.631*	Estimated[12] r_e using r_0 value from ref 11 and MRCI-F12/CVQZ-F12 potential energy functions		
H_2NOH	1.47(3)	X-ray crystallography[13]	1.436	1.423
	1.453(2)	Microwave spectroscopy[14]		
H_3NOH^+	1.411(2)	X-ray crystallography[15] of chloride salt	1.393	1.385
H_3PO	1.4763*	Microwave spectroscopy[16] (r_0)	1.479	1.474

* No experimental error reported in reference.

Table A.2. Numerical values of ρ_b, $\nabla^2\rho_b$, and ε_b depicted in Figure 2.2.

	ρ_b (a.u.)	**$\nabla^2\rho_b$ (a.u.)**	**ε_b**
NO^+	0.747	-3.538	0.000
PO^+	0.257	1.869	0.000
AsO^+	0.245	1.076	0.000
SbO^+	0.189	0.827	0.000
BiO^+	0.174	0.646	0.000
HNO	0.521	-1.548	0.113
HPO	0.232	1.381	0.129
HAsO	0.218	0.766	0.091
HSbO	0.173	0.672	0.063
HBiO	0.157	0.527	0.058
H_2NOH	0.298	-0.398	0.027
H_2POH	0.163	0.542	0.002
H_2AsOH	0.154	0.360	0.040
H_2SbOH	0.128	0.424	0.065
H_2BiOH	0.115	0.358	0.074
H_3NOH^+	0.347	-0.637	0.055
H_3POH^+	0.207	0.935	0.080
H_3AsOH^+	0.194	0.528	0.072
H_3SbOH^+	0.157	0.559	0.084
H_3BiOH^+	0.142	0.423	0.088
H_3NO	0.366	-0.442	0.000
H_3PO	0.243	1.375	0.000
H_3AsO	0.229	0.609	0.000

H_3SbO	0.183	0.598	0.000
H_3BiO	0.168	0.452	0.000

Table A.3. AIM atomic charges (CCSD/ANO-RCC-QZP//MP2/def2-QZVPP).

	Charge on O	**Charge on E**	**Charge separation**
NO^+	-0.30	1.30	1.60
PO^+	-1.20	2.20	3.41
AsO^+	-0.83	1.83	2.66
SbO^+	-0.86	1.86	2.73
BiO^+	-0.79	1.79	2.57
HNO	-0.42	0.10	0.52
HPO	-1.39	2.02	3.41
HAsO	-1.04	1.39	2.44
HSbO	-1.06	1.46	2.51
HBiO	-0.96	1.31	2.28
H_2NOH	-0.85	-0.54	0.31
H_2POH	-1.44	2.03	3.46
H_2AsOH	-1.26	1.28	2.54
H_2SbOH	-1.27	1.41	2.68
H_2BiOH	-1.23	1.27	2.50
H_3NOH^+	-0.72	-0.65	0.07
H_3POH^+	-1.52	3.51	5.03
H_3AsOH^+	-1.28	2.18	3.47
H_3SbOH^+	-1.30	2.36	3.66
H_3BiOH^+	-1.23	1.94	3.17

H_3NO	-0.71	-0.52	0.19
H_3PO	-1.57	3.46	5.03
H_3AsO	-1.19	2.07	3.27
H_3SbO	-1.18	2.18	3.36
H_3BiO	-1.04	1.77	2.81

REFERENCES

1. Zhang, X.; Seppelt, K., Nitrosonium Nitrate, an Isomer of N_2O_4 in IF_5. *Zeitschrift fur anorganische und allgemeine Chemie* **1998,** *624* (4), 667-670.

2. Albritton, D. L.; Schmeltekopf, A. L.; Zare, R. N., Potential energy curves for NO^+. *Journal of Chemical Physics* **1979,** *71* (8), 3271-3279.

3. Petrmichl, R. H.; Peterson, K. A.; Woods, R. C., The microwave spectrum of PO^+: Comparison to SiF^+. *Journal of Chemical Physics* **1991,** *94* (5), 3504-3510.

4. Dyke, J. M.; Morris, A.; Ridha, A., Study of the ground state of PO^+ using photoelectron spectroscopy. *Journal of the Chemical Society, Faraday Transactions 2* **1982,** *78* (12), 2077-2082.

5. Rao, D. V. K.; Rao, P. T., Rotational analysis of the ultra-violet system of AsO^+. *Journal of Physics B* **1970,** *3* (3), 430-437.

6. Tripathi, R.; Rai, S. B.; Upadhya, K. N., The A-X system of the SbO^+ molecule. *Journal of Physics B* **1981,** *14* (3), 441-445.

7. Saito, S.; Takagi, K., Microwave spectrum of nitroxyl. *Journal of Molecular Spectroscopy* **1973,** *47* (1), 99-106.

8. Zaleski, D. P.; Prozument, K., Pseudo-equilibrium geometry of HNO determined by an E-Band CP-FTmmW spectrometer. *Chemical Physics Letters* **2017,** *680*, 101-108.

9. Tackett, B. S.; Clouthier, D. J., HPO does not follow Walsh's rules! Improved molecular structures from the spectroscopy of jet-cooled HPO and DPO. *Journal of Chemical Physics* **2002,** *117* (23), 10604-10612.

10. Ozeki, H.; Saito, S., Microwave spectra of HPO and DPO: molecular structure. *Journal of Molecular Spectroscopy* **2003,** *219* (2), 305-312.

11. Grimminger, R.; Clouthier, D. J., The electronic spectrum of the previously unknown HAsO transient molecule. *Journal of Chemical Physics* **2011,** *135* (18), 184308.

12. Mok, D. K. W.; Lee, E. P. F.; Dyke, J. M., Simulation of the single-vibronic-level emission spectra of HAsO and DAsO. *Journal of Chemical Physics* **2016,** *144* (18), 184303.

13. Meyers, E. A.; Lipscomb, W. N., The crystal structure of hydroxylamine. *Acta Crystallographica* **1955,** *8* (9), 583-587.

14. Tsunekawa, S., Microwave Spectrum of Hydroxylamine. *Journal of the Physical Society of Japan* **1972,** *33* (1), 167-174.

15. Shi, K.-L.; Wang, R.-Q.; Mak, T. C. W., On the N-O bond length in free and *N*-protonated hydroxylamine, and redetermination of the crystal structure of hydroxylammonium chloride, (H_3NOH)Cl. *Journal of Molecular Structure* **1987,** *160* (1-2), 109-116.

16. Ahmad, I. K.; Ozeki, H.; Saito, S., Microwave spectroscopic detection of a transient phosphorus-bearing molecule, H_3PO. *Journal of Chemical Physics* **1999,** *110* (2), 912-917.

Appendix B: Supplementary Experimental Data for Chapter 3

Published in part in: Lindquist-Kleissler, B.; Johnstone, T. C. *Inorg. Chem.* **2021,** *60*, 8566.

Table B.1. Refinement details for the crystal structures of $SbPh_5$, $SbPh_5 \cdot ½C_6H_{12}$, and $SbPh_5 \cdot ½C_4H_8O$.

Compound	**$SbPh_5$**	**$SbPh_5 \cdot ½C_6H_{12}$**	**$SbPh_5 \cdot ½C_4H_8O$**
Formula	$C_{30}H_{25}Sb$	$C_{33}H_{31}Sb$	$C_{32}H_{29}O_{0.5}Sb$
FW	507.25	549.33	543.3
T (K)	100(2)	100(2)	100(2)
λ (Å)	1.54184	1.54184	0.71073
Crystal System	Triclinic	Triclinic	Triclinic
Space group	$P\bar{1}$	$P\bar{1}$	$P\bar{1}$
a (Å)	10.1928(3)	10.2897(3)	10.4264(5)
b (Å)	10.3972(2)	10.5423(3)	10.4877(4)
c (Å)	13.4432(3)	13.1942(4)	13.3125(5)
α (°)	67.791(2)	68.599(2)	69.334(4)
β (°)	78.375(2)	78.209(2)	76.277(4)
γ (°)	61.226(2)	88.616(2)	86.523(4)
Volume ($Å^3$)	1155.78(5)	1302.47(7)	1322.73(10)
Z	2	2	2
ρ_{calc} (Mg/m^3)	1.458	1.401	1.364
Size (mm^3)	0.06×0.05×0.02	0.10×0.08×0.02	0.10×0.07×0.04
θ range (°)	3.55-66.59	3.68-68.24	1.68-25.02
Total data	13596	13670	15049
Unique data	4052	4738	4651
Parameters	280	307	425
Completeness	99.3%	99.6%	99.4%
R_{int}	2.53%	3.46%	3.69%
R_1 ($I > 2\sigma$)	2.01%	2.28%	3.55%
R_1 (all data)	2.11%	2.46%	3.78%
wR_2 ($I > 2\sigma$)	5.19%	5.37%	8.93%
wR_2 (all data)	5.23%	5.43%	9.05%
S	1.072	1.082	1.053

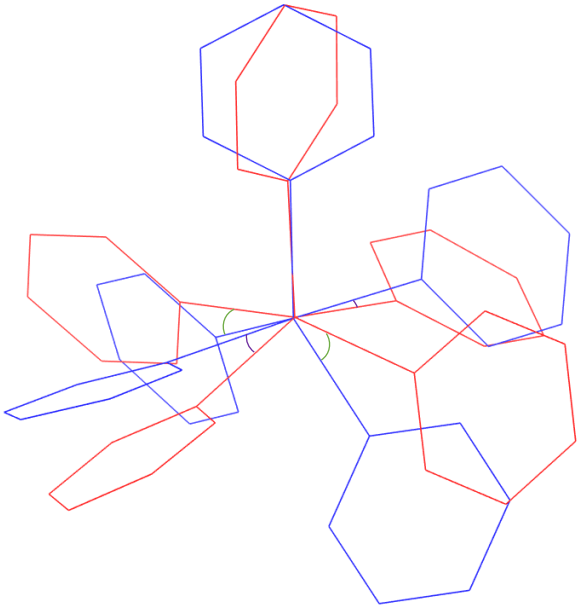

Figure B.1. Overlaid wireframe diagrams of $SbPh_5$ (red) and $SbPh_5 \cdot ½C_6H_{12}$ (blue). Solvent and hydrogen atoms omitted for clarity. Purple and green arcs highlight the angular deviations between the two structures.

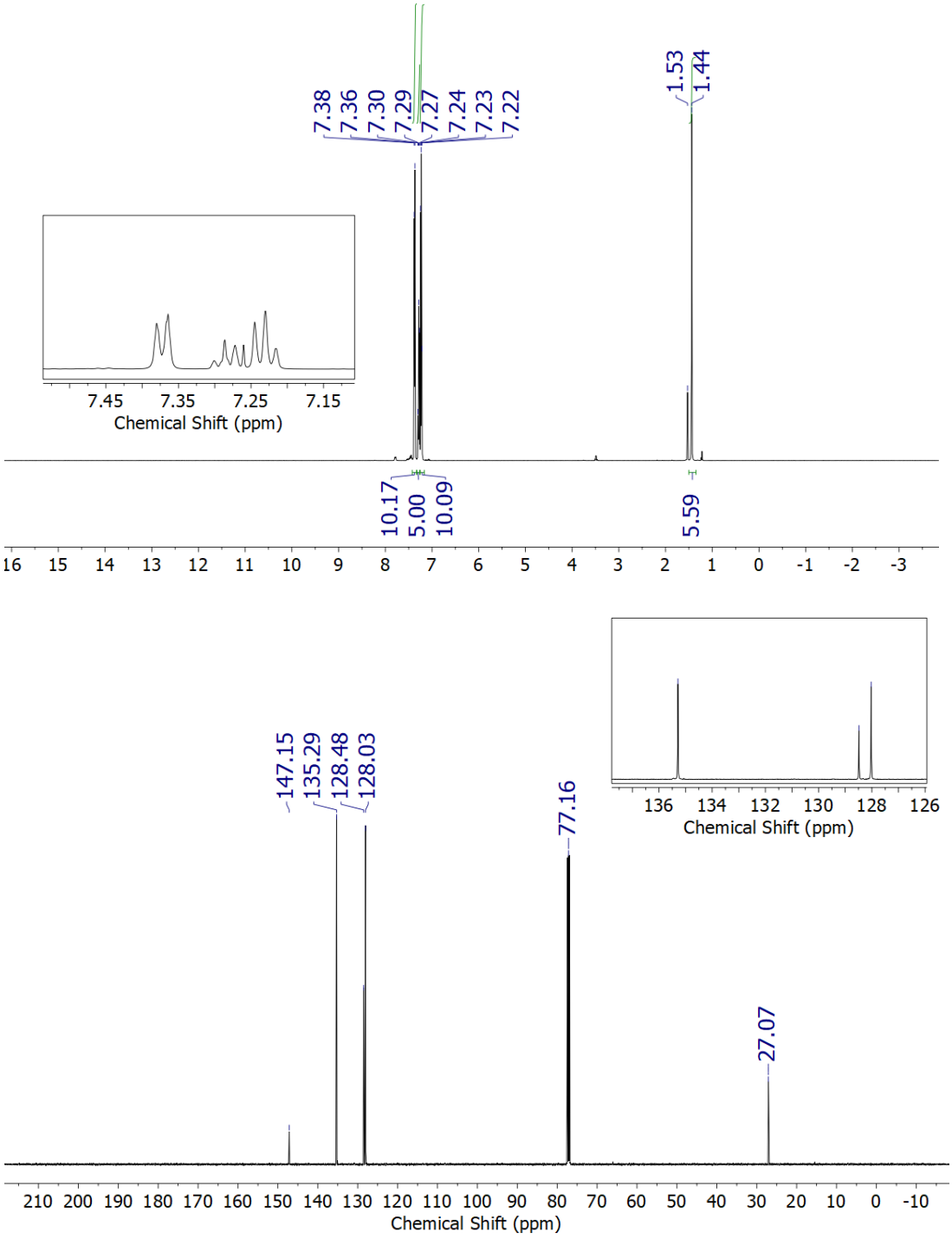

Figure B.2. *Top*: ^{1}H NMR (500 MHz, $CDCl_3$) spectrum of $SbPh_5 \cdot ½C_6H_{12}$. *Bottom*: $^{13}C\{^{1}H\}$ NMR (126 MHz, $CDCl_3$) spectrum of $SbPh_5 \cdot ½C_6H_{12}$.

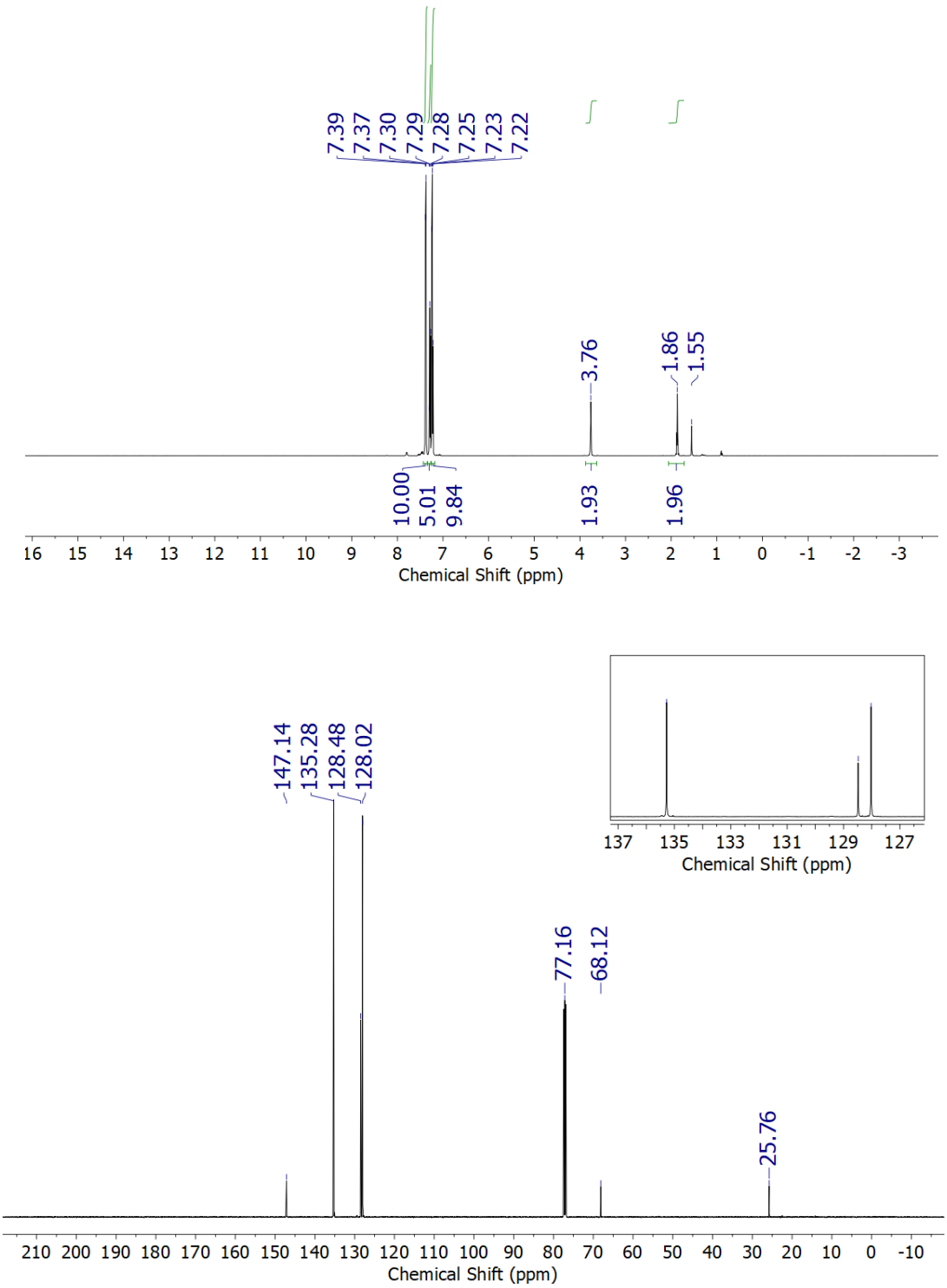

Figure B.3. *Top*: ^{1}H NMR (500 MHz, $CDCl_3$) spectrum of $SbPh_5 \cdot ½C_4H_8O$. *Bottom*: $^{13}C\{^{1}H\}$ NMR (126 MHz, $CDCl_3$) spectrum of $SbPh_5 \cdot ½C_4H_8O$.

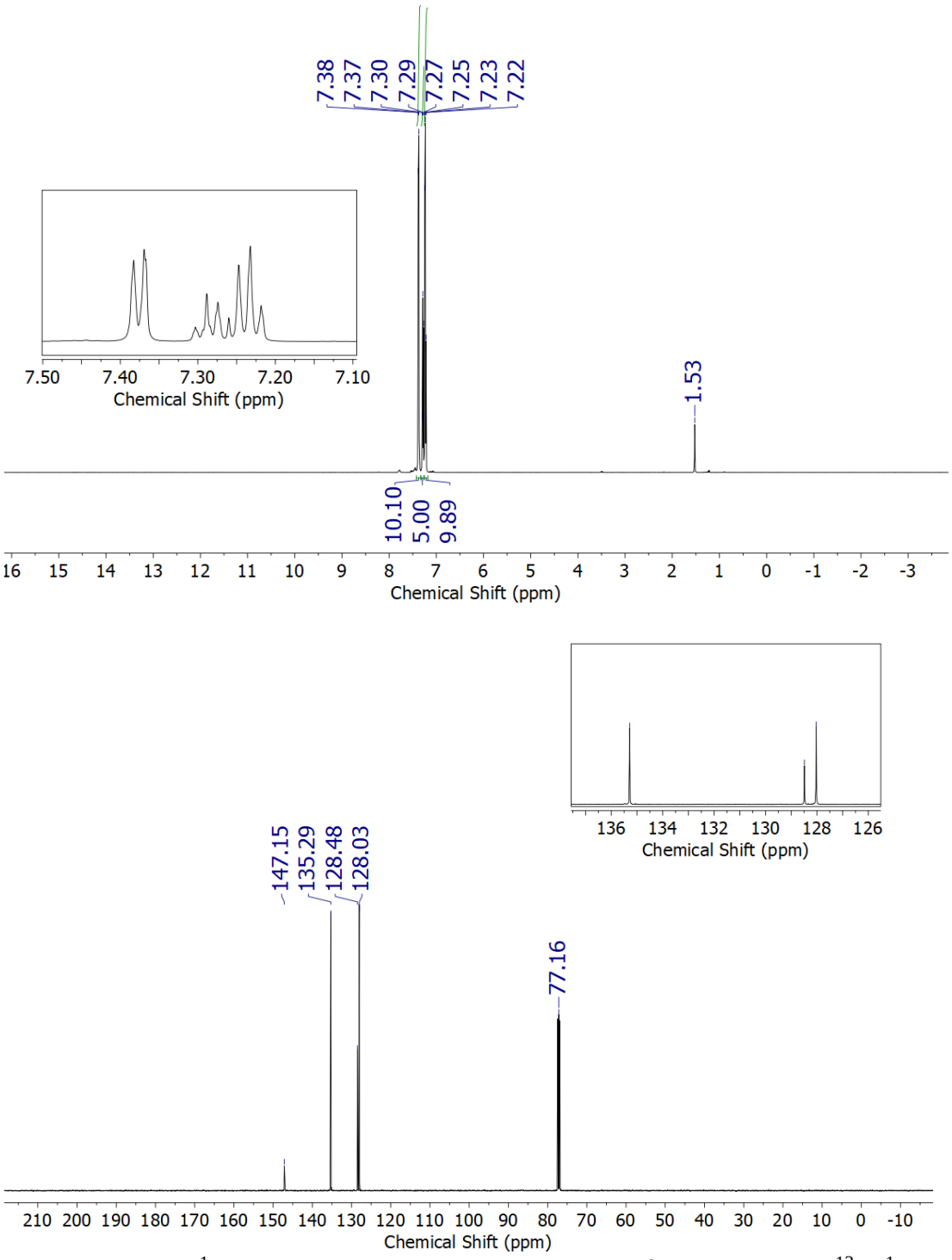

Figure B.4. *Top*: ^{1}H NMR (500 MHz, $CDCl_3$) spectrum of $SbPh_5$. *Bottom*: $^{13}C\{^{1}H\}$ NMR (126 MHz, $CDCl_3$) spectrum of $SbPh_5$.

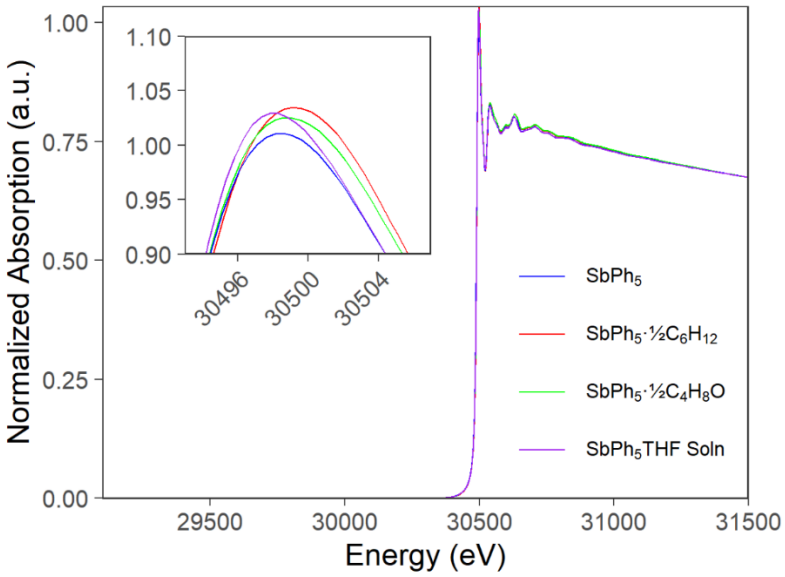

Figure B.5. Sb K-edge spectra of the three solid forms of $SbPh_5$ as well as a sample of non-solvated $SbPh_5$ dissolved in THF.

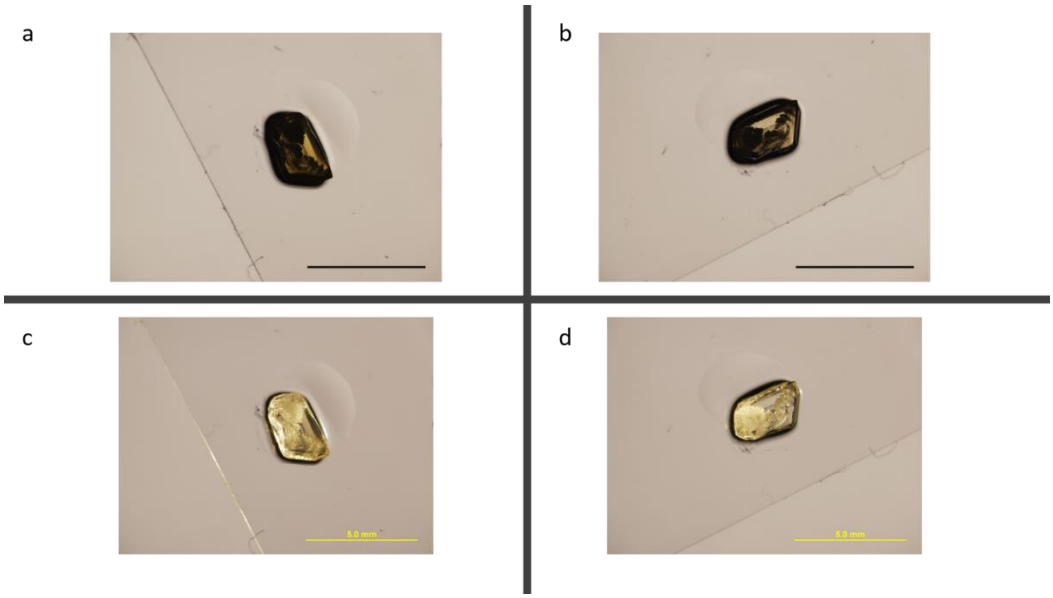

Figure B.6. Stereomicrographs of a crystal of solvent-free $SbPh_5$. (a) $SbPh_5$ crystal with only transmission lighting. (b) $SbPh_5$ crystal with only transmission lighting and rotated 90º from a. (c) $SbPh_5$ crystal with external illumination. (d) $SbPh_5$ crystal with external illumination and rotated 90º from c.

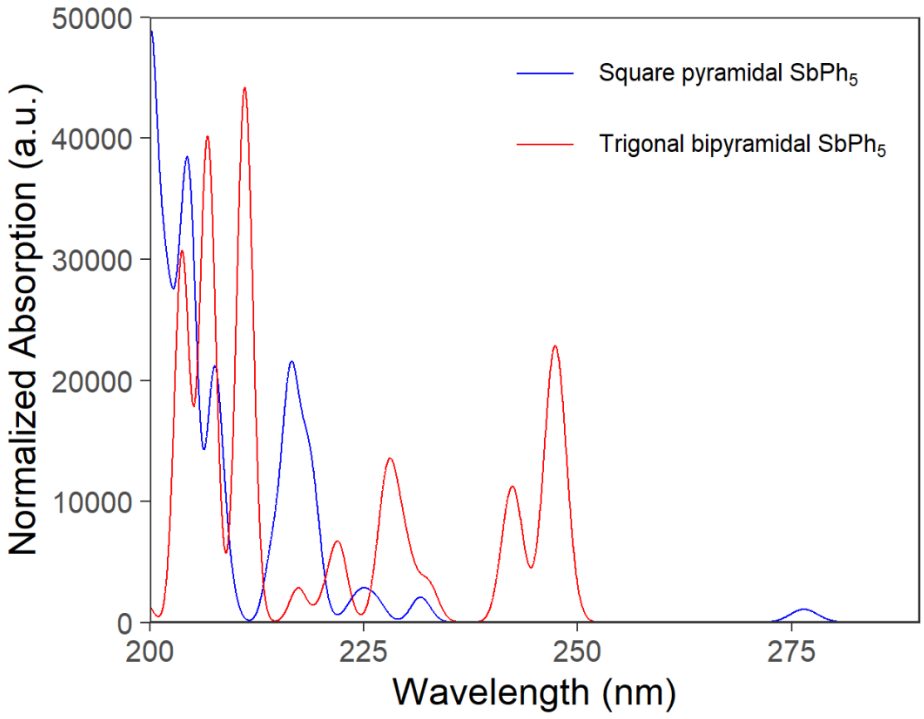

Figure B.7. Overlay of TDDFT calculated (DKH2-ωB97X-D3BJ/old-DKH-TZVP(-f)) electronic absorption spectra for $SbPh_5$ in a square pyramidal (blue) or trigonal bipyramidal (red) geometry.

Table B.2. Calculated (DKH2-ωB97X-D3BJ/old-DKH-TZVP(-f)) Sb K-edge energies and oscillator strengths (f_{osc}) for $SbPh_5$ in both square pyramidal and trigonal bipyramidal geometries. The most intense transition (14) is italicized; energies are unshifted.

Square Pyramidal $SbPh_5$		
State	**Energy (eV)**	**f_{osc}**
1	30293.7085	0.00020608
2	30295.4680	0.00006039
3	30296.0829	0.00017092
4	30296.2665	0.00009417
5	30296.5589	0.00000776
6	30296.9210	0.00000015
7	30297.0112	0.00001080
8	30297.1538	0.00000366
9	30297.4348	0.00000162
10	30297.5001	0.00000373
11	30297.9590	0.00000891
12	30298.0505	0.00012728
13	30298.1229	0.00015997
14	*30298.6883*	*0.00025553*
15	30298.8222	0.00002955
16	30299.6019	0.00004845
17	30299.8124	0.00002741
18	30299.9718	0.00000869
19	30300.0697	0.00000623
20	30300.1527	0.00000591
21	30300.4147	0.00004283
22	30300.5309	0.00000191
23	30300.8548	0.00000219
24	30300.9825	0.00000010
25	30301.0111	0.00000391
26	30301.0890	0.00000035
27	30301.1876	0.00000858
28	30301.2275	0.00000431
29	30301.2830	0.00001056
30	30301.3709	0.00000274
31	30301.4568	0.00000323
32	30301.4771	0.00000799
33	30301.5442	0.00003427
34	30301.7010	0.00001392
35	30301.7395	0.00003282
36	30302.0585	0.00001508
37	30302.0926	0.00001099
38	30302.1652	0.00000801
39	30302.2709	0.00000083
40	30302.3276	0.00000207
41	30302.3541	0.00001698
42	30302.4571	0.00000391
43	30302.5947	0.00000159
44	30302.6375	0.00000607
45	30302.6897	0.00000242
46	30302.8330	0.00004185
47	30302.9216	0.00001129
48	30302.9513	0.00002607
49	30303.1160	0.00001379
50	30303.2054	0.00002926

Trigonal Bipyramidal $SbPh_5$		
State	**Energy (eV)**	**f_{osc}**
1	30294.8501	0.00021737
2	30295.1160	0.00000365
3	30295.2004	0.00020681
4	30296.3310	0.00001226
5	30296.4829	0.00003678
6	30296.6390	0.00011535
7	30296.9650	0.00000353
8	30297.0198	0.00000583
9	30297.0922	0.00000375
10	30297.6236	0.00005927
11	30297.7704	0.00003187
12	30297.8655	0.00004478
13	30297.9698	0.00003198
14	*30298.6415*	*0.00028405*
15	30298.8677	0.00000054
16	30299.4371	0.00001279
17	30299.5249	0.00002223
18	30299.5885	0.00003250
19	30300.0380	0.00004190
20	30300.1073	0.00003089
21	30300.3875	0.00001271
22	30300.5225	0.00001107
23	30300.6995	0.00000024
24	30300.9368	0.00000147
25	30300.9785	0.00000130
26	30301.0295	0.00000169
27	30301.1015	0.00000494
28	30301.1667	0.00000067
29	30301.3143	0.00000078
30	30301.4179	0.00000533
31	30301.4659	0.00000914
32	30301.5589	0.00000120
33	30301.5721	0.00000467
34	30301.6311	0.00002490
35	30301.6730	0.00003284
36	30301.8814	0.00001188
37	30302.0331	0.00000424
38	30302.0531	0.00000930
39	30302.1368	0.00000295
40	30302.1606	0.00000656
41	30302.2791	0.00000766
42	30302.3410	0.00001047
43	30302.4443	0.00000822
44	30302.6125	0.00000125
45	30302.6849	0.00001466
46	30302.7521	0.00000837
47	30302.8370	0.00000293
48	30302.9480	0.00000468
49	30303.0352	0.00001009
50	30303.0486	0.00001994

Appendix C: Supplementary Experimental Data for Chapter 4

Published in part in: Lindquist-Kleissler, B.; Johnstone, T. C. *Dalton Trans*. **2023**, 52, 9229.

Table C.1. Refinement details for the crystal structures of $Sb(tol)_3$ and $[(tol)_3Sb(\mu\text{-}C_4H_8O_2)]_2O$.

	$Sb(tol)_3$	**$[(tol)_3Sb(\mu\text{-}C_4H_8O_2)]_2O$**
Formula	$C_{21}H_{21}Sb$	$C_{36}H_{44}O_5Sb_2$
FW	395.13	800.21
T (K)	101.1(6)	102(2)
λ (Å)	1.54184	1.54184
Crystal System	Trigonal	Orthorhombic
Space group	$R\bar{3}$	$P2_12_12_1$
a (Å)	12.6758(3)	12.17550(10)
b (Å)		13.5809(2)
c (Å)	19.8058(4)	20.6690(3)
Volume (Å^3)	2755.96(14)	3417.71(8)
Z	6	4
ρ_{calc} (Mg/m^3)	1.428	1.555
Size (mm^3)	0.21×0.14×0.04	0.12×0.06×0.05
θ range (°)	4.605-67.036	3.895-67.684
Total data	6111	51012
Unique data	1099	7095
Parameters	68	397
Completeness	100.0%	100.0%
R_{int}	4.87%	5.45%
R_1 (I > 2σ)	2.11%	3.25%
R_1 (all data)	2.16%	3.39%
wR_2 (I > 2σ)	5.41%	8.52%
wR_2 (all data)	5.43%	8.64%
S	1.098	1.078
Flack *x*	—	-0.015(9)

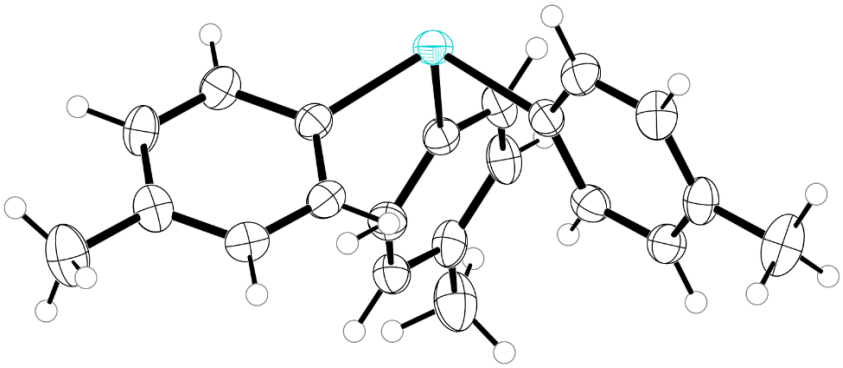

Figure C.1. Thermal ellipsoid plot (50% probability, H atoms as spheres of arbitrary radius) of $Sb(tol)_3$**.** Color code: Sb teal, C black, H white.

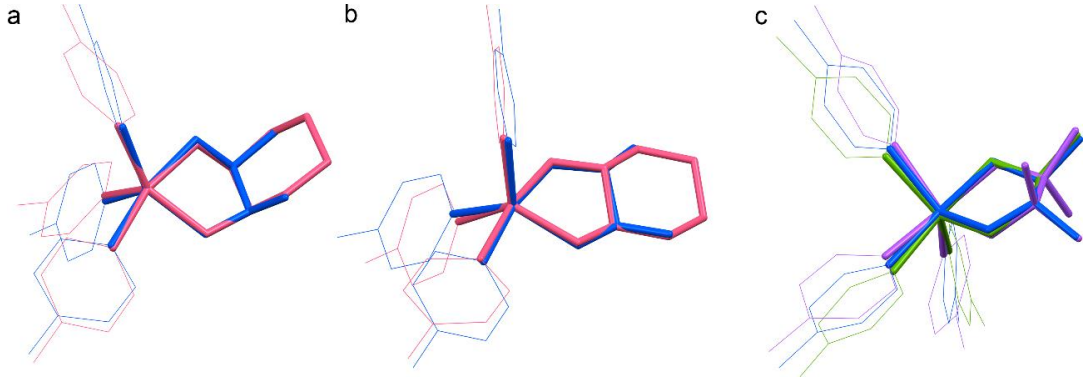

Figure C.2. Overlays of: a) **2** (blue) and **3** (pink). b) **4** (blue) and **5** (pink). c) **1** (purple), **4** (blue), and **6** (green).

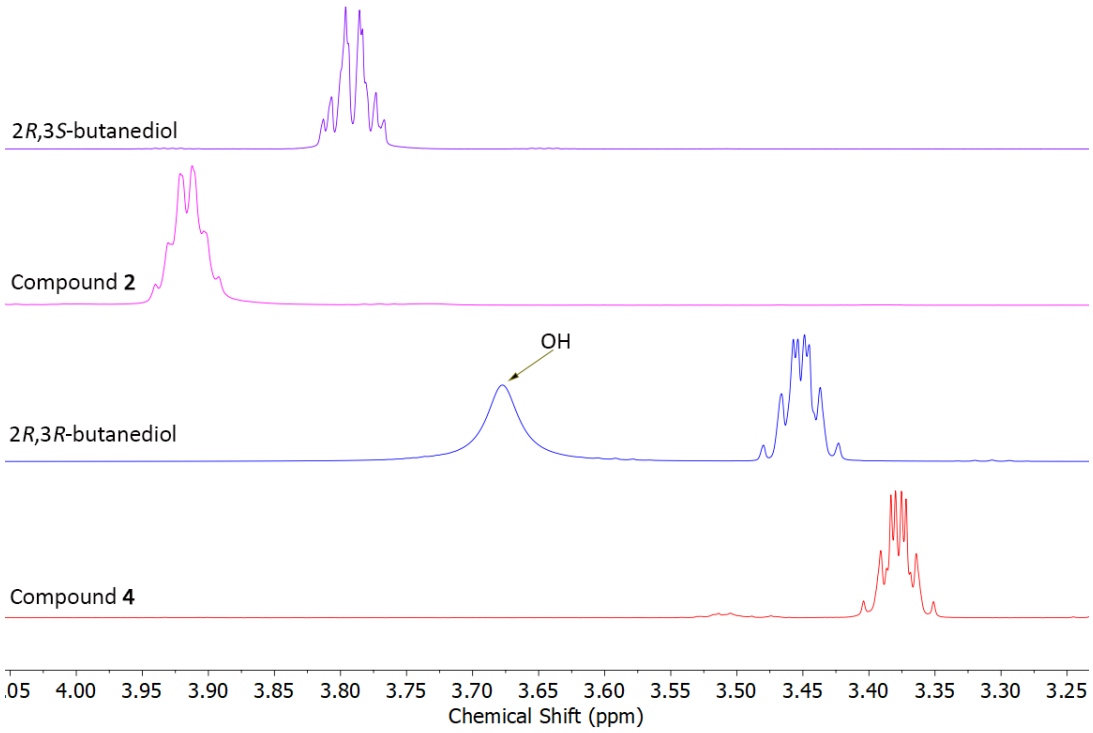

Figure C.3. Stacked ^{1}H NMR spectra showing shift in backbone CH resonances. Color code: unbound 2*R*,3*S*-butanediol purple, compound **2** pink, unbound 2*R*,3*R*-butanediol blue, compound **4** red.

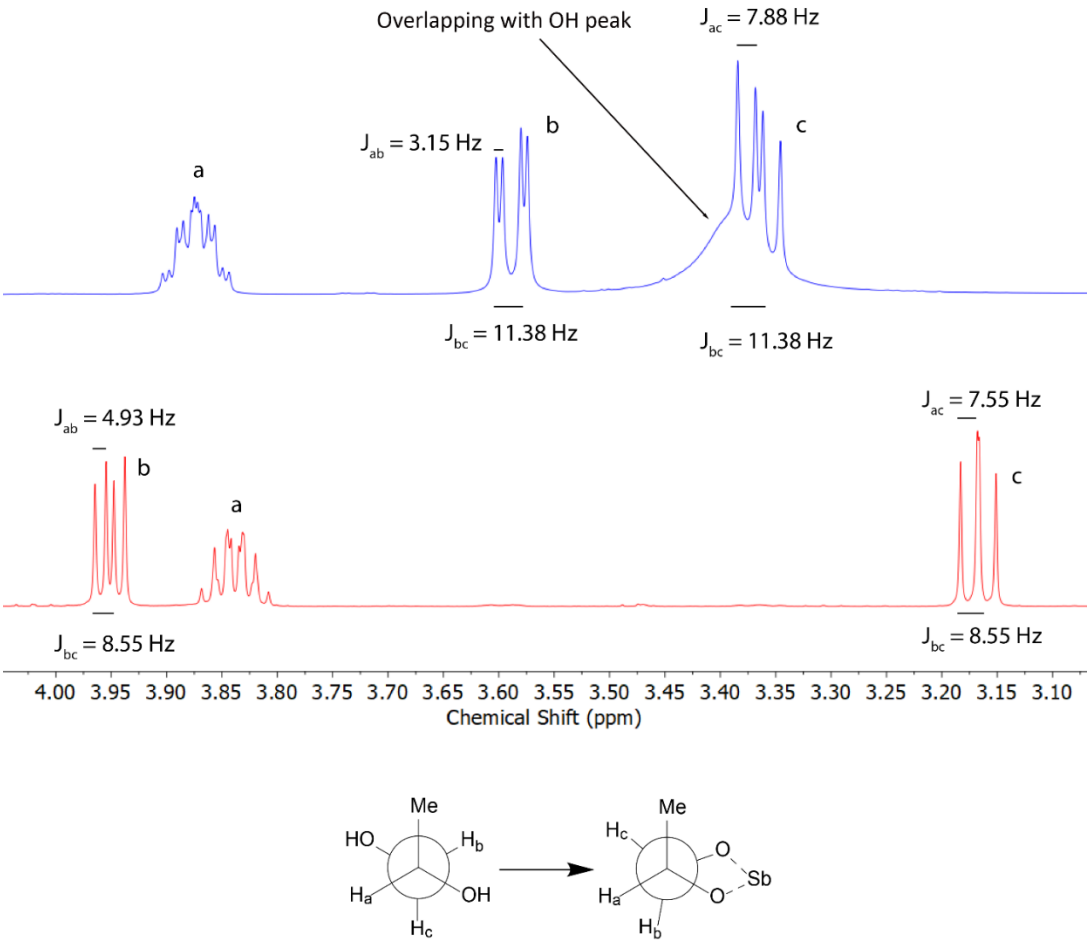

Figure C.4. *Top (blue)*: ^{1}H NMR spectrum of free (*S*)-1,2-propanediol. Peaks are arbitrarily labeled based on the labelling scheme used for the Newman projections. *Middle (red)*: ^{1}H NMR spectrum of **6**. *Bottom*: Newman projections displaying conformational change of (*S*)-1,2-propanediol upon binding to Sb.

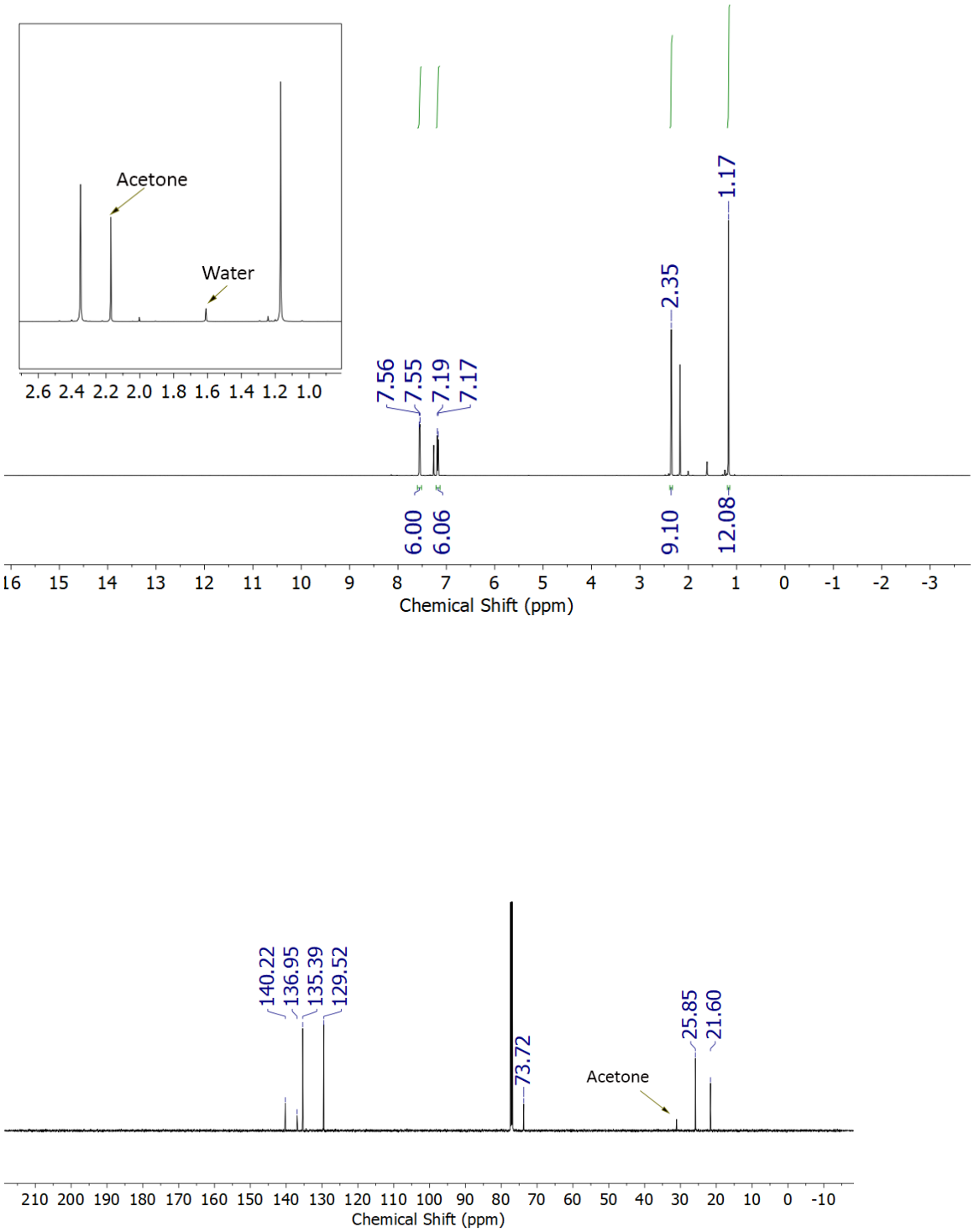

Figure C.5. *Top*: ^{1}H NMR (500 MHz, $CDCl_3$) spectrum of **1**. *Bottom*: $^{13}C\{^{1}H\}$ NMR (126 MHz, $CDCl_3$) spectrum of **1**.

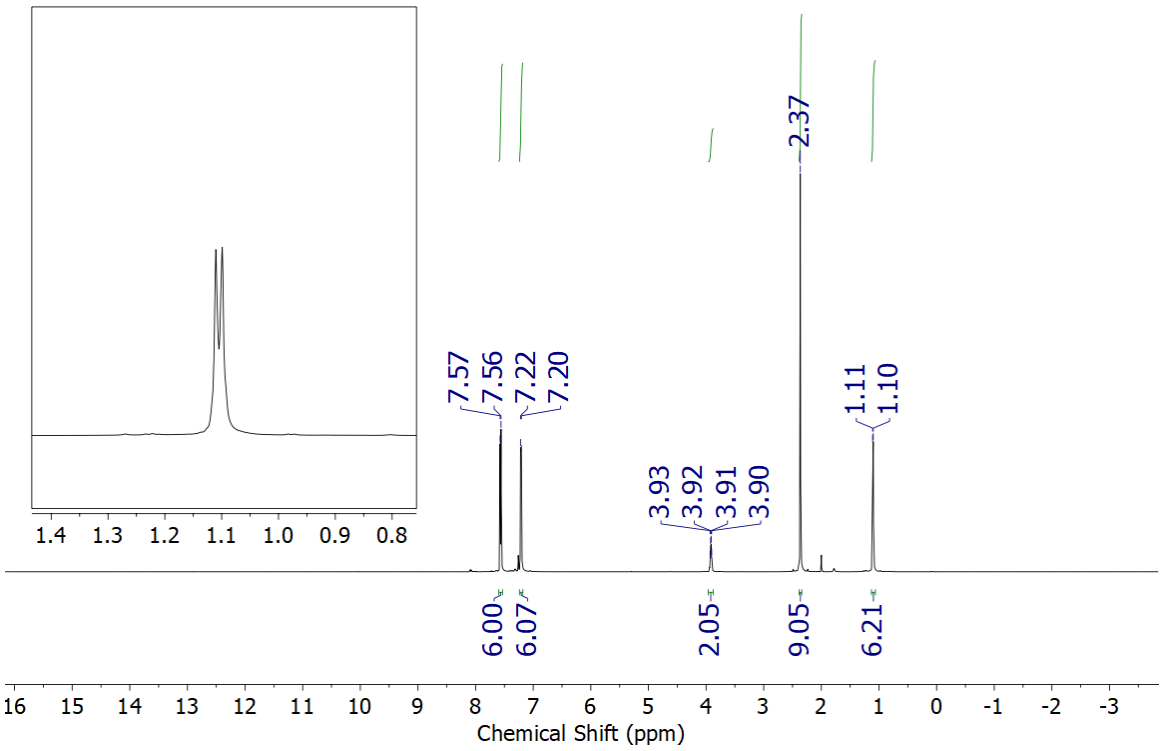

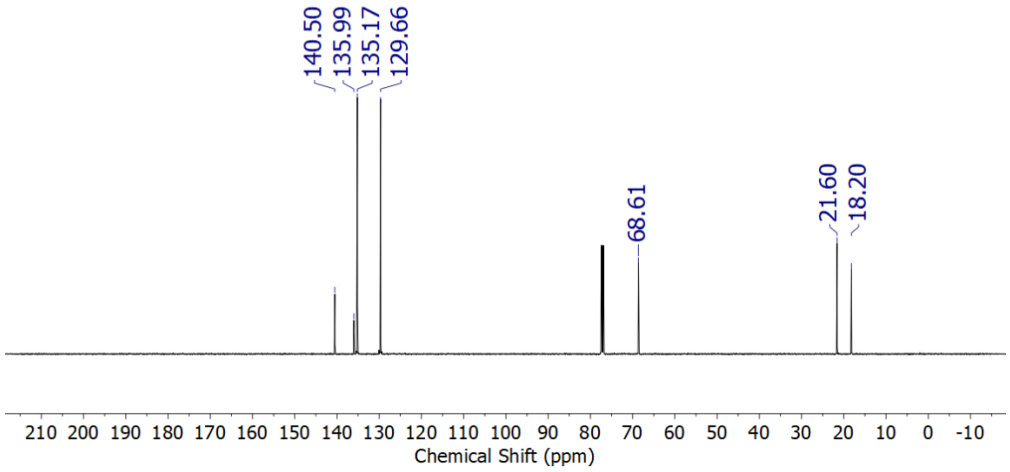

Figure C.6. *Top*: ^{1}H NMR (500 MHz, $CDCl_3$) spectrum of **2**. *Bottom*: $^{13}C\{^{1}H\}$ NMR (126 MHz, $CDCl_3$) spectrum of **2**.

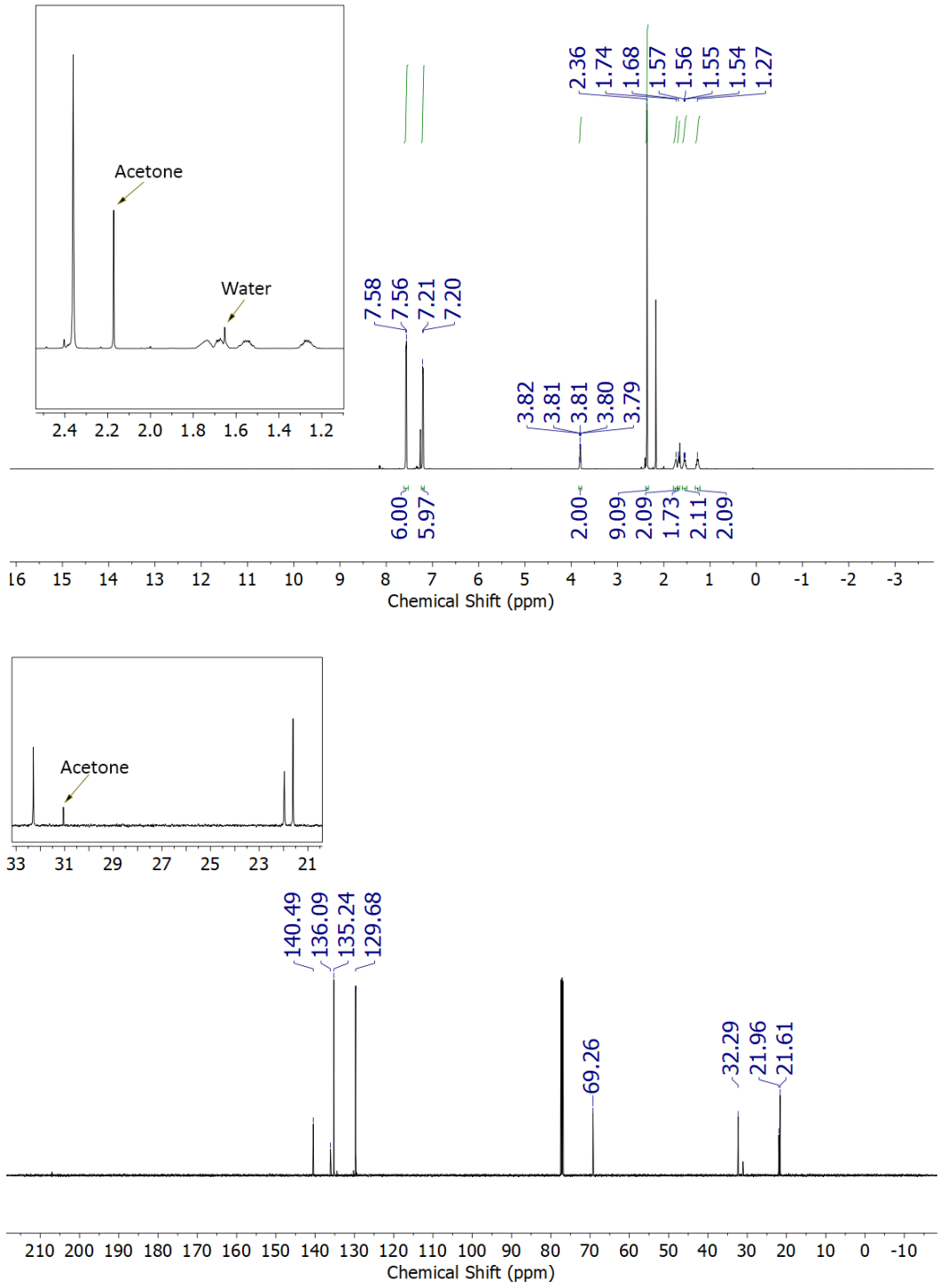

Figure C.7. *Top*: ^{1}H NMR (500 MHz, $CDCl_3$) spectrum of **3**. *Bottom*: $^{13}C\{^{1}H\}$ NMR (126 MHz, $CDCl_3$) spectrum of **3**.

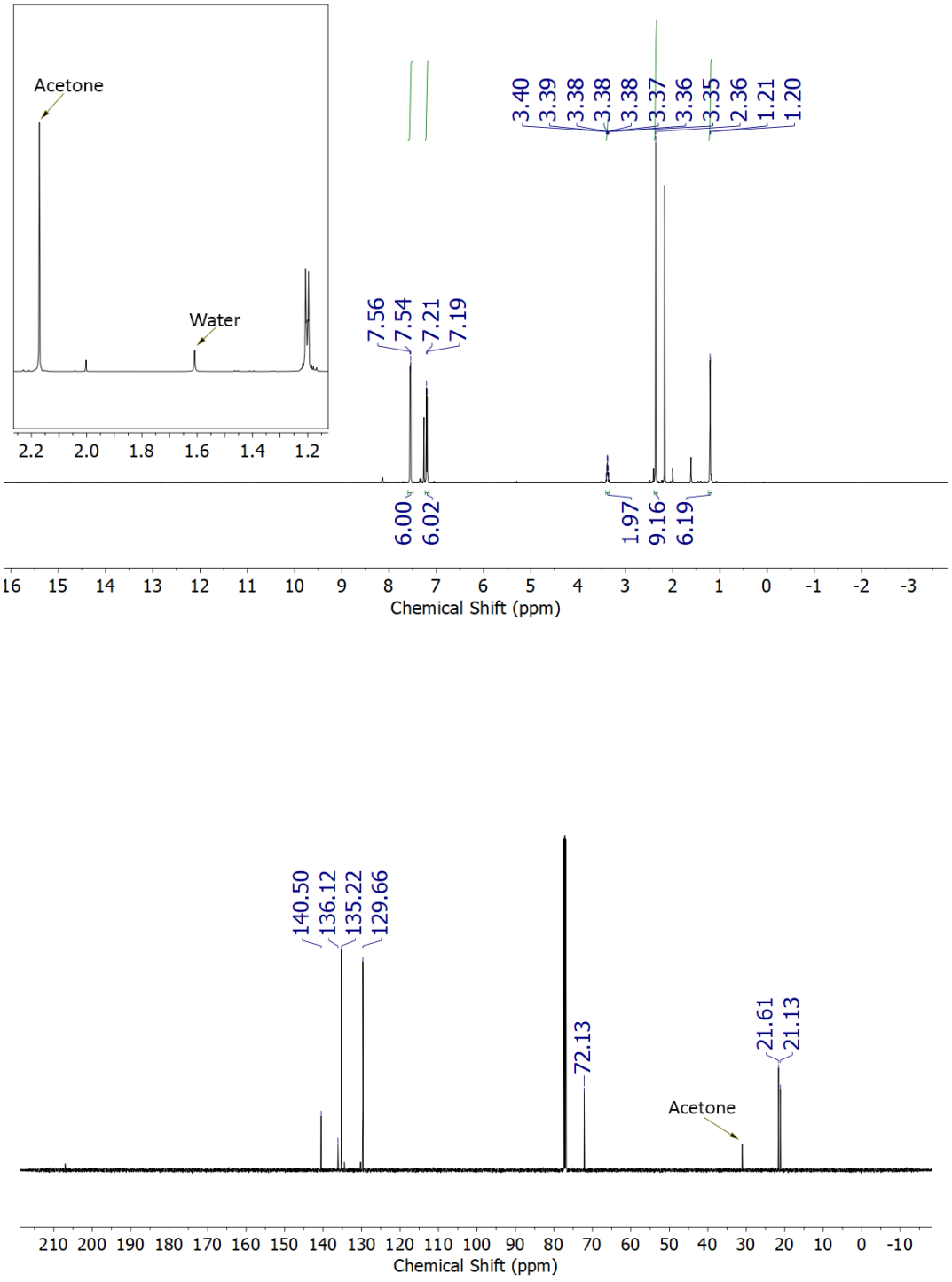

Figure C.8. *Top*: ^{1}H NMR (500 MHz, $CDCl_3$) spectrum of **4**. *Bottom*: $^{13}C\{^{1}H\}$ NMR (126 MHz, $CDCl_3$) spectrum of **4**.

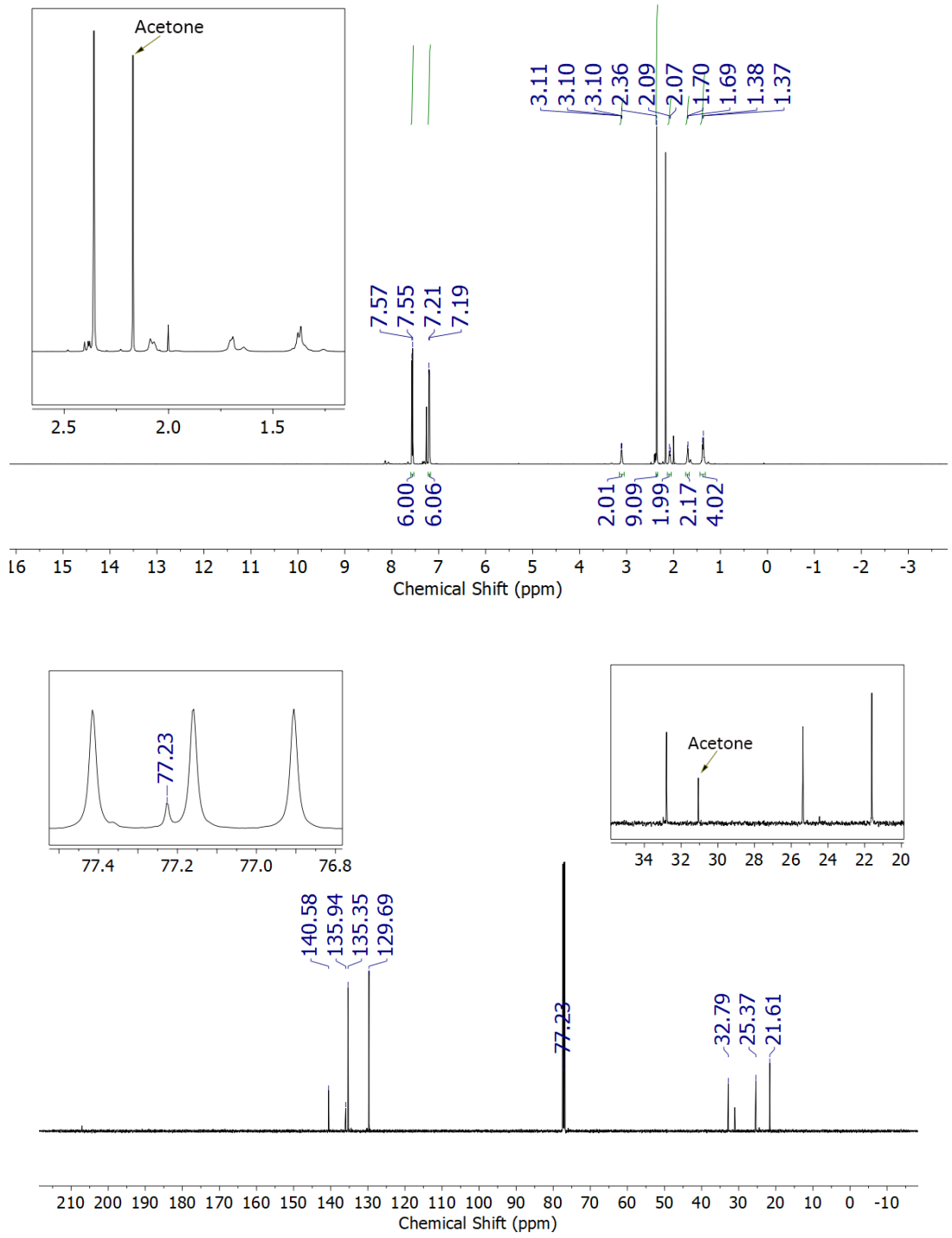

Figure C.9. *Top*: ^{1}H NMR (500 MHz, $CDCl_3$) spectrum of **5**. *Bottom*: $^{13}C\{^{1}H\}$ NMR (126 MHz, $CDCl_3$) spectrum of **5**.

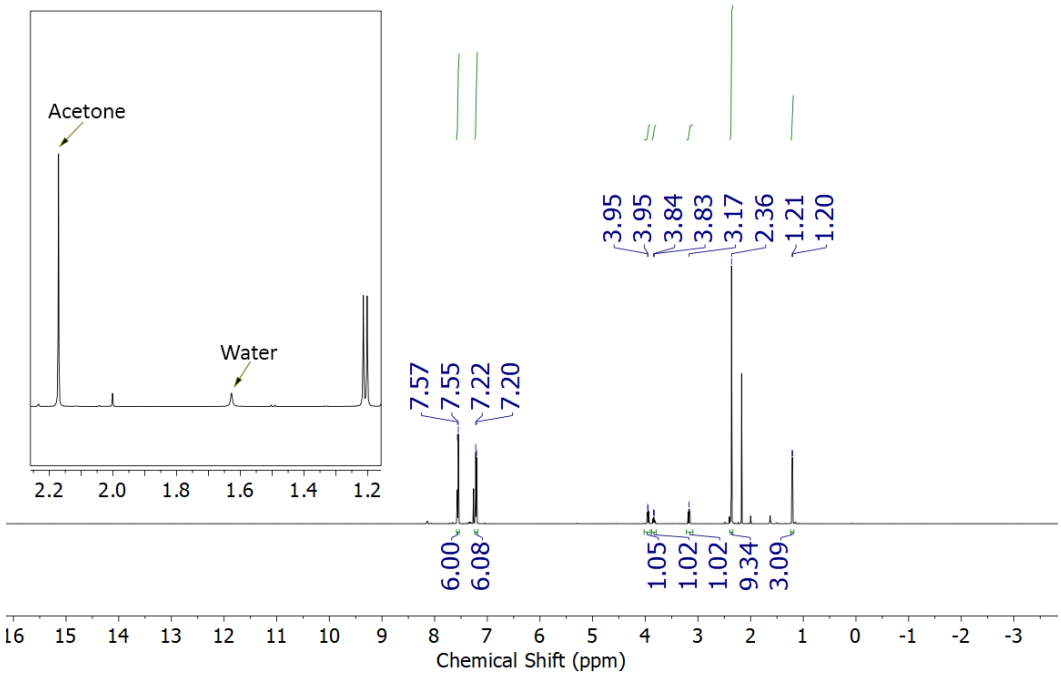

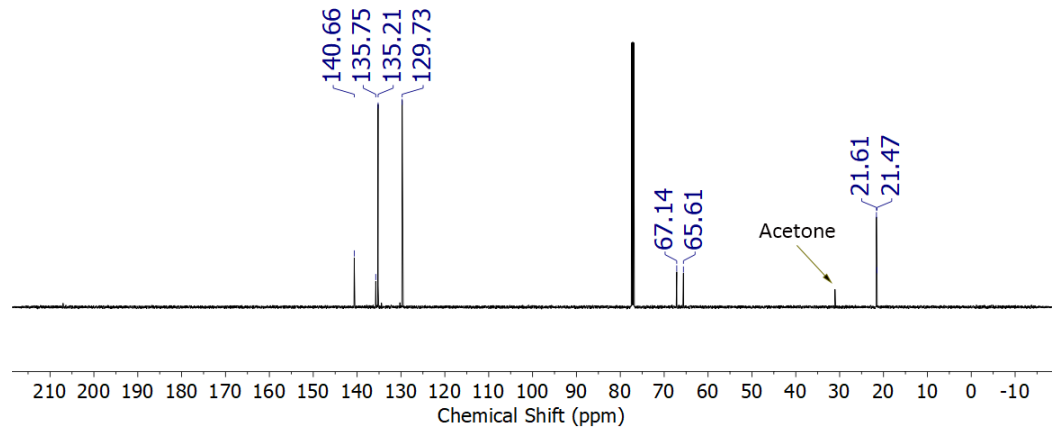

Figure C.10. *Top*: ^{1}H NMR (500 MHz, $CDCl_3$) spectrum of **6**. *Bottom*: $^{13}C\{^{1}H\}$ NMR (126 MHz, $CDCl_3$) spectrum of **6**.

Appendix D: Supplementary Experimental Data for Chapter 5

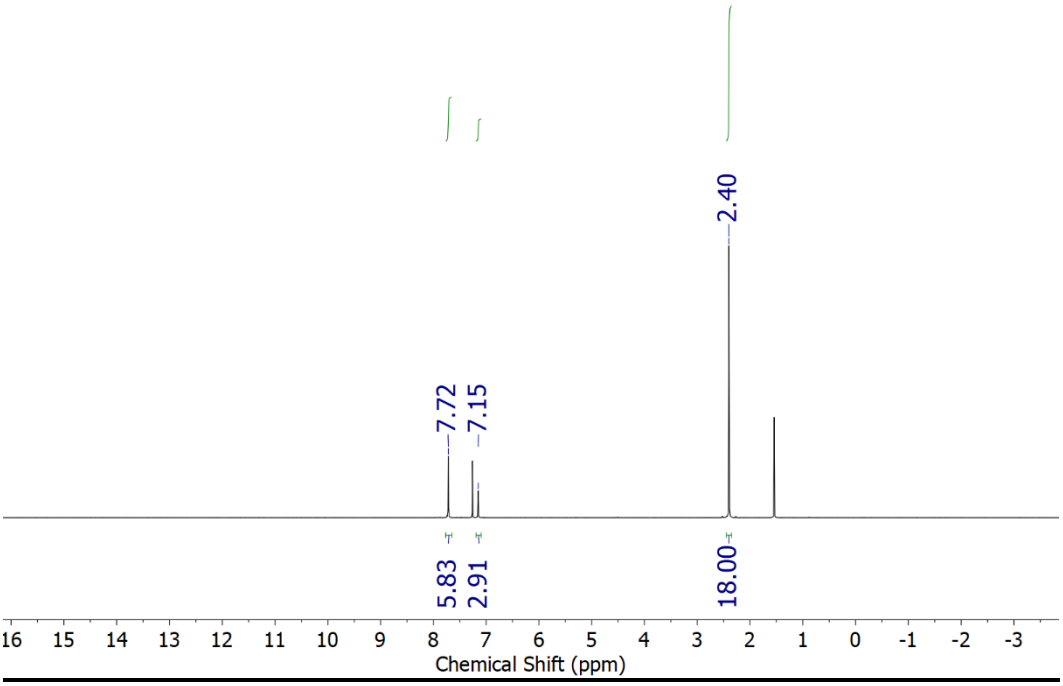

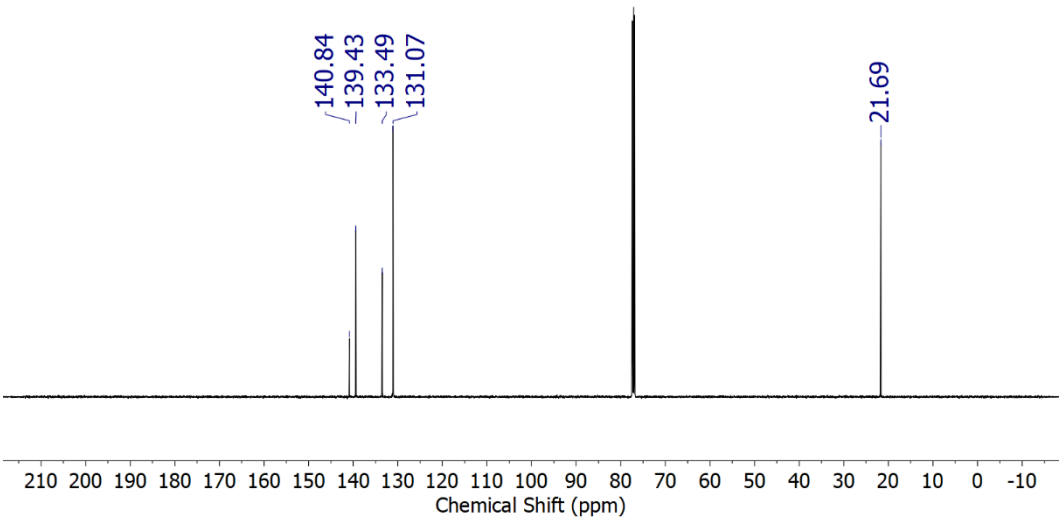

Figure D.1. *Top*: ^{1}H NMR (500 MHz, $CDCl_3$) spectrum of Sb(*m*-xyl)$_3$Br$_2$. *Bottom*: $^{13}C\{^{1}H\}$ NMR (126 MHz, $CDCl_3$) spectrum of Sb(*m*-xyl)$_3$Br$_2$**.**

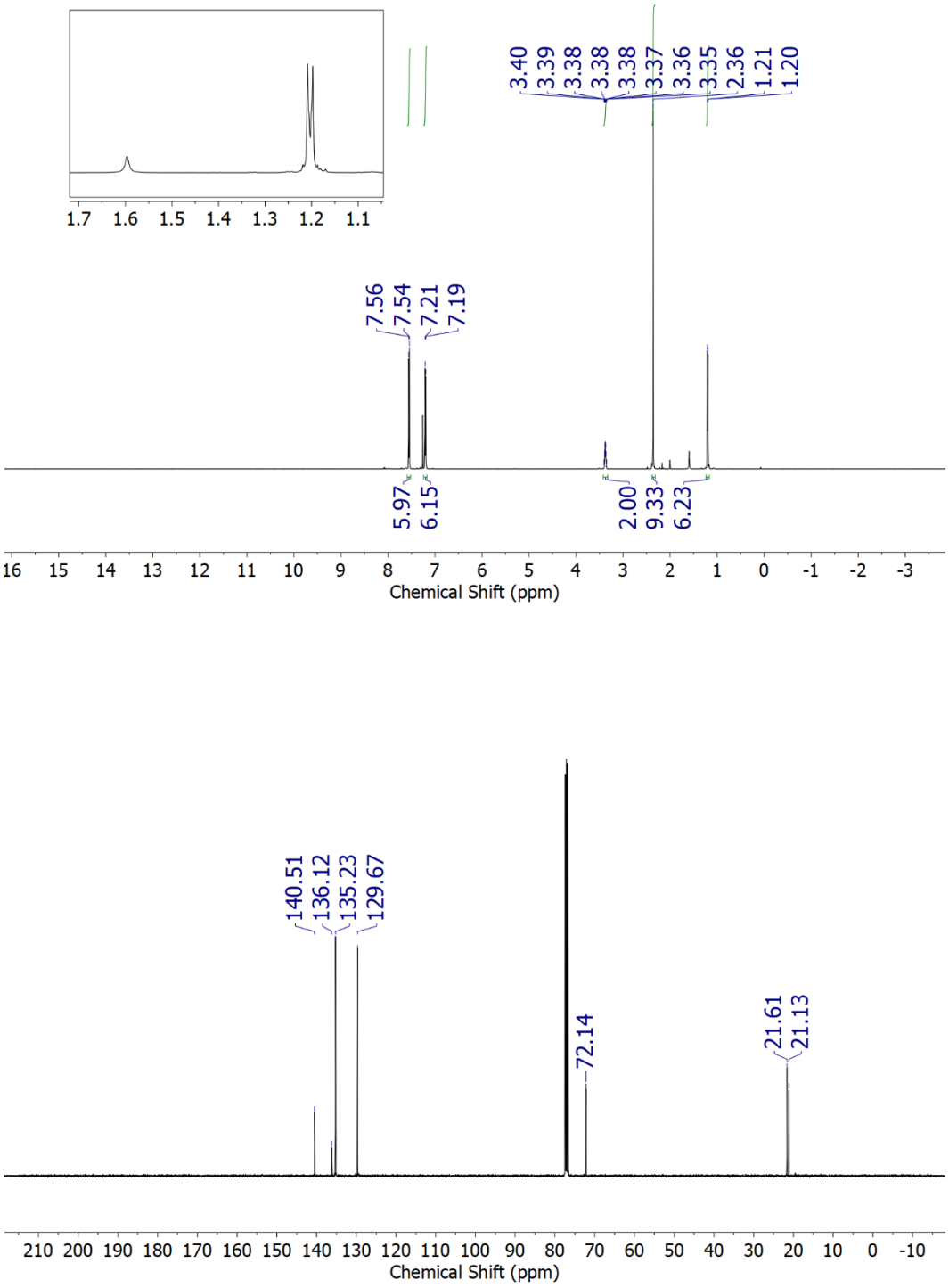

Figure D.2. *Top*: ^{1}H NMR (500 MHz, $CDCl_3$) spectrum of **7**. *Bottom*: $^{13}C\{^{1}H\}$ NMR (126 MHz, $CDCl_3$) spectrum of **7.**

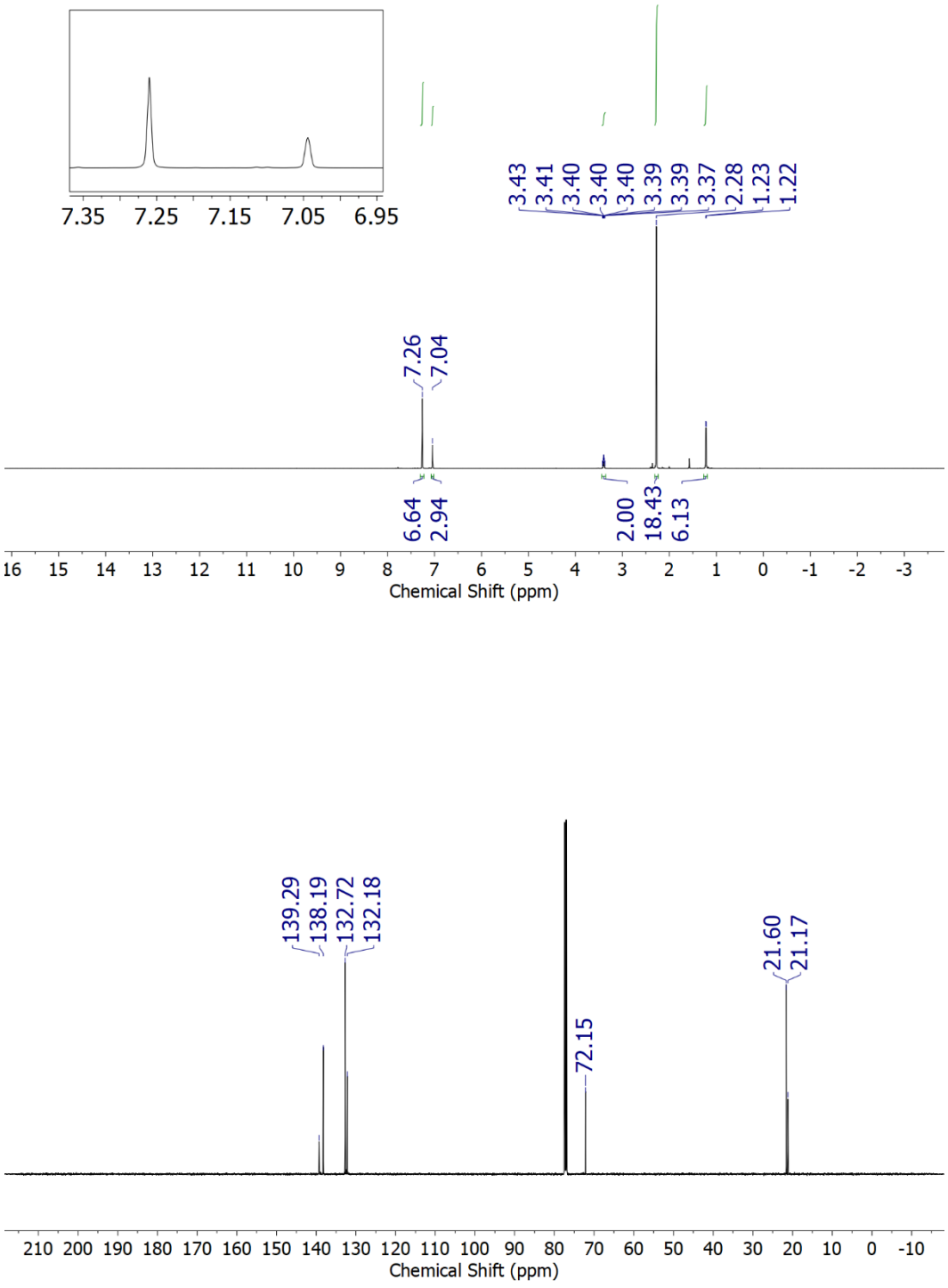

Figure D.3. *Top*: ^{1}H NMR (500 MHz, $CDCl_3$) spectrum of **8**. *Bottom*: $^{13}C\{^{1}H\}$ NMR (126 MHz, $CDCl_3$) spectrum of **8.**

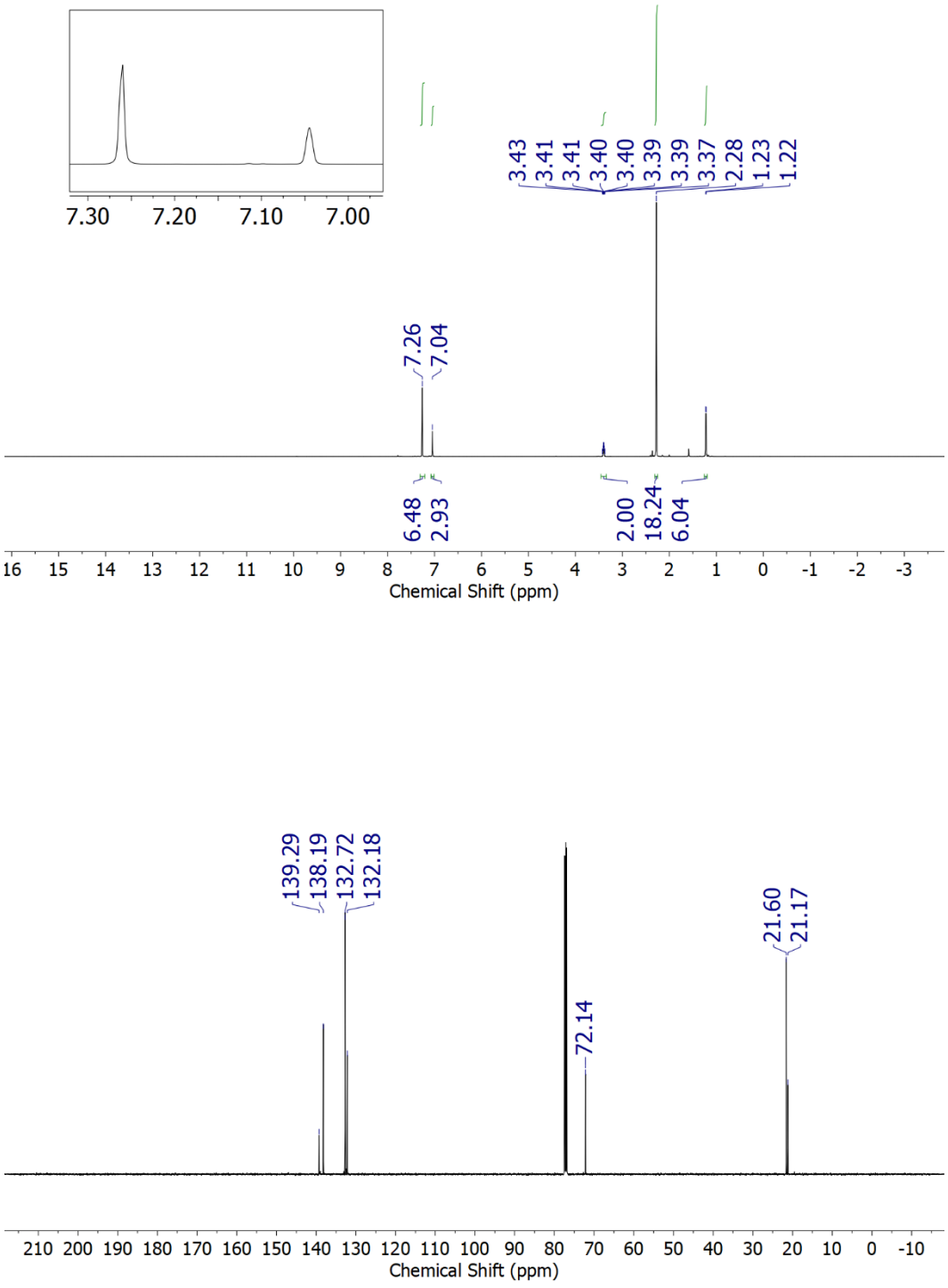

Figure D.4. *Top*: ^{1}H NMR (500 MHz, $CDCl_3$) spectrum of **9**. *Bottom*: $^{13}C\{^{1}H\}$ NMR (126 MHz, $CDCl_3$) spectrum of **9**.